Collective excitations in the transitional nuclei $^{163}\mathbf{Re}_{88}$ and $^{165}\mathbf{Re}_{90}$

Thesis submitted in accordance with the requirements of the University of Liverpool for the degree of Master of Philosophy

Tom Rees Davis-Merry

Oliver Lodge Laboratory

2014

"*For a successful technology, reality must take precedence over public relations, for Nature cannot be fooled.*"

Richard Feynman, in conclusion to his report on
the Space Shuttle Challenger disaster of 1986.

"*MEN WANTED ... For Hazardous Journey. Small wages, bitter cold, long months of complete darkness, constant danger. Safe return doubtful. Honour and recognition in case of success ...*"

Sir Ernest Henry Shackleton's advertisement for the
Imperial Trans-Antarctic Expedition 1914-17.

"*As the nuclear surface is approached, take heed, for there be dragons ...*"

Professor Rodi Herzberg, on the dangers of mankind's
venture to the edge of the mesoscopic world.

Acknowledgements

I would like to express a tremendous gratitude towards my supervisor Dr. David Joss for your encouragement, support and good humour. You have given me the opportunity to undertake a piece of challenging and academically stimulating research, and for this I am most grateful.

I would like to thank Dr. Mark Drummond for your invaluable assistance with Java coding, data sorting and open-source software. To have learnt so much in so little time would have been impossible without your support. Many thanks also to Chris McPean and Alex Thornthwaite for your many insightful discussions and problem-solving lines of code.

I cannot express enough the thanks I owe my parents; as my financiers, logistical support, catering team and hoteliers, my many adventures, travels and other antics would not have been possible without you.

I would like to thank all the members of the Nuclear Physics group at the University of Liverpool, it has been a delight to work with a group of such friendly, helpful and intelligent physicists. Thanks also to the staff and postgraduate students at the University of Jyväskylä for your insightful discussions and great hospitality, my visits to Finland have been some of the highlights of this course.

I would like to recognise the contribution from the collaborators involved in this work, I thank you for your support and invaluable input.

I would also like to acknowledge the STFC, who have provided the financial support for this research.

I would finally like to express a great thank you to Sarah Harley, for not only has your outrageous sense of humour kept me sane in times when adventures were in short supply, but without your support and encouragement this thesis may have never been written.

Abstract

Excited states in the neutron-deficient nuclei $^{163}\mathrm{Re}_{88}$ and $^{165}\mathrm{Re}_{90}$ have been populated in the ^{106}Cd(^{60}Ni,$p2n\gamma$) and ^{92}Mo(^{78}Kr,$3p2n\gamma$) fusion-evaporation reactions at bombarding energies of 270 MeV and 357 MeV, respectively. Gamma rays were detected at the target position using the JUROGAM spectrometer array while recoiling ions were separated in-flight by the RITU gas-filled recoil separator and implanted into the double-sided silicon strip detectors of the GREAT spectrometer. The level excitation schemes for ^{163}Re and ^{165}Re have been identified using recoil-decay correlation techniques. At low spin, the yrast bands of these isotopes are strongly coupled bands based on a single $\pi h_{11/2}$ quasiproton configuration. The bands display large signature splitting consistent with the soft triaxial shape typical of transitional nuclei above $N = 82$. The configurations of the excited states are proposed within the framework of the cranked shell model.

Contents

Chapter 1

Introduction

The atomic nucleus is a unique and fascinating system of strongly interacting fermions. Its landmark discovery in 1911 by Ernest Rutherford [1] revolutionised our understanding of the mesoscopic world and laid the foundations for a wealth of further research.

When the motion of a significant fraction of these constituent nucleons becomes coherent, collective excitations arise that may in some cases lead to a deformation of the nuclear shape. Understanding the evolution of this collective behaviour and the fundamental influence of specific quasiparticle configurations across isotopic chains has been of long-standing importance in nuclear physics. It is well understood that nuclei near closed shells will exhibit phenomena derived from single-particle excitations. However, as valance nucleons are added to or removed from closed shells, couplings between these constituent particles will give rise to collective phenomena, such as deformation and rotation.

The complex interactions between the constituent nucleons in this many-body quantised system are far from fully understood and, furthermore, the computing resources required to solve any analytical calculations for all but the lightest nuclei make this approach utterly impractical. A solution to this problem is to adopt

models that can approximate the nuclear potential and still allow for meaningful insight into this complex and unique system.

The validation of models established in the early 20^{th} century to describe the atomic nucleus used experimental investigations of nuclei relatively close to stability. Using advances in accelerator science and radiation detection systems, it has now become possible to investigate the properties of nuclei in the regions far from stability, which had previously remained elusive. This allows for the testing of nuclear models under extreme conditions such as, for example, those of high neutron deficiency.

Gamma-ray spectroscopy has played a key role in such developments. In particular, the recoil decay tagging (RDT) technique [2] allows for γ-ray data to be correlated with specific nuclei by utilising spatial and temporal correlations with the implantation of an isotope and its subsequent decay. The advent of this innovative technique and its use in conjunction with large γ-ray spectrometers has allowed for the evolution of nuclear structure to be better understood in the extremely neutron-deficient Ta-W-Re-Os-Ir-Pt region [3]. This region holds a particular interest due to the fact that the interplay between single-particle excitations and collective behaviour is observed for nuclei with $N \backsim 90$, where the nuclear structure can evolve swiftly within the range of a few neutrons.

The spectroscopy of excited states in the $A \backsim 170$ region of neutron-deficient isotopes presents two principal experimental challenges. First, the desired fusion exit channels exhibit low population cross-sections (which rapidly diminish further from the line of stability), and second, fission events result in the presence of high γ-ray backgrounds.

On a chart of nuclides, the boundary beyond which nuclei are unstable against proton emission is known as the proton drip line. This work is concerned with nuclei in the neutron-deficient region close to this boundary and the $N = 82$ shell closure, as

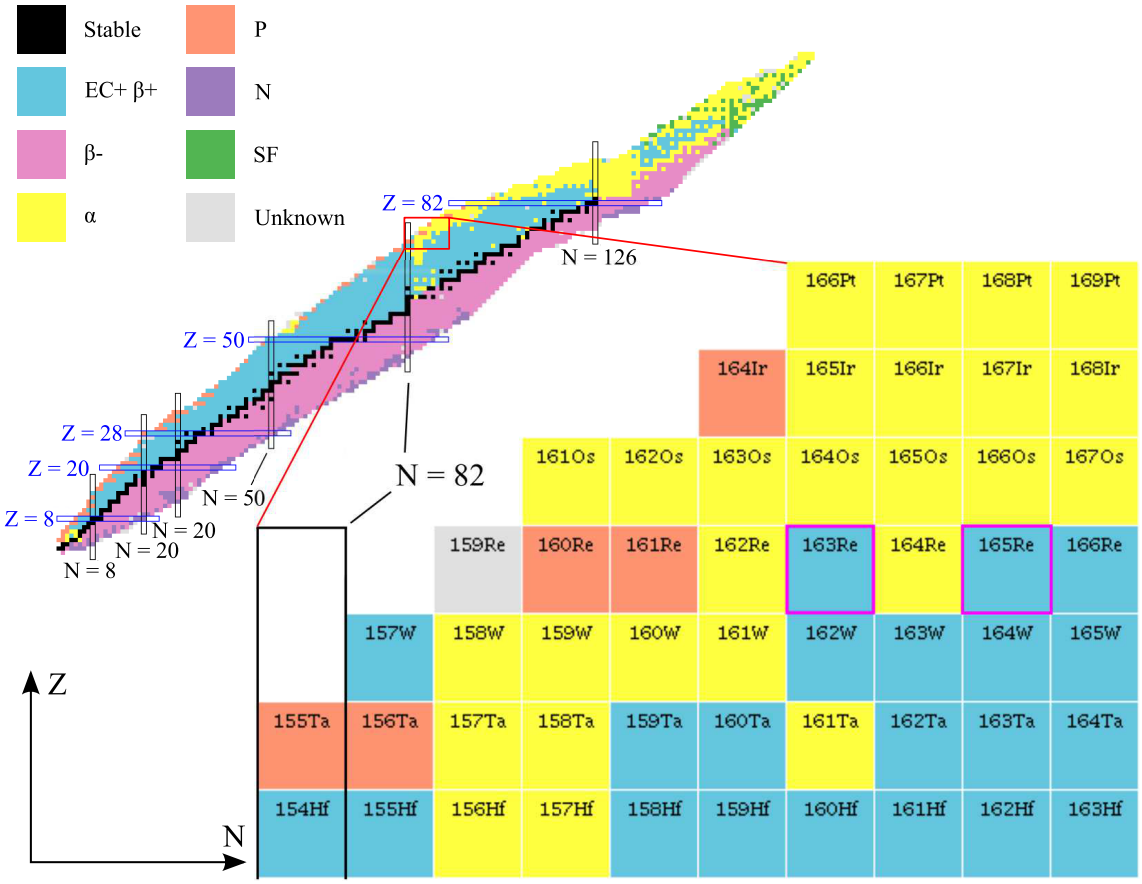

FIGURE 1.0.1: Nuclides in the neutron-deficient region close to the proton drip line and the $N = 82$ shell closure. ^{163}Re and ^{165}Re have been highlighted, and colour-coding is used to indicate the nuclear decay mode.

shown in Figure 1.0.1. Nuclei in this region can be considered as quantised systems comprising valance nucleons coupled to a semi-magic ^{146}Gd core [4]. Thus, the orbitals available for proton occupation are $1h_{11/2}$, $2d_{3/2}$ and $3s_{1/2}$, while neutrons occupy the $2f_{7/2}$, $1h_{9/2}$ and $1i_{13/2}$ orbitals.

The yrast structures of the odd-Z Re isotopes are expected to evolve from the vibrational states in the the proton emitter ^{161}Re [5] to the strongly coupled collective band structures observed in ^{167}Re [3] and the heavier isotopes [6, 7, 8, 9, 10]. A Swedish adjective, *yrast* is the superlative of *yr* and literally translates to dizziest, referring to the greatest obtainable angular momentum for a given energy. The yrast structure of ^{163}Re and ^{165}Re is based on the $11/2^-$ α-decaying isomeric state [11, 12].

In both nuclei, this structure is shown to comprise a strongly coupled band which indicates a collective behaviour not dissimilar to that of the heavier isotopes. In ^{163}Re, two further candidates for strongly coupled band structures are observed in this work. Quasiparticle configurations are assigned to each of these bands, based on a comparison with cranked shell model (CSM) calculations and considerations of the observed signature splitting.

Prior to the results discussed in this thesis, excited configurations in ^{163}Re had been only tentatively assigned, and excited states in ^{165}Re had not been observed. As a result, this work presents the first study of the evolution of nuclear structure in the transitional region between ^{161}Re and the heavier isotopes.

Chapter 2

Concepts in Nuclear Physics

2.1 Nuclear models

2.1.1 The many-body nuclear problem

The atomic nucleus is a many-body problem involving numerous interacting nucleons. In principle, understanding this complex quantum system involves solving the Schrödinger equation (2.1.1) for a given nucleus

$$\hat{H}\Psi = i\hbar\frac{\partial\Psi}{\partial t}, \tag{2.1.1}$$

where Ψ is the total wave function of the nucleus and is dependent on the spatial, temporal, spin and isospin coordinates of the constituent nucleons. The Hamiltonian (2.1.2) for such a system has two terms: the first is the kinetic energy of the nucleons and the second is an interaction potential energy between the nucleons consisting of a Coulomb and a central potential.

$$\hat{H} = \sum_{i=1}^{A} T_i + \sum_{i\neq j} V_{ij} \tag{2.1.2}$$

For the stationary states of the nucleus Φ, the Schrödinger equation thus becomes (2.1.3) where E is the energy of the stationary states.

$$\hat{H}\Phi = \left(\sum_{i=1}^{A} T_i + \sum_{i \neq j} V_{ij} \right) \Phi = E\Phi \tag{2.1.3}$$

The problem for nuclear physics is that this nuclear interaction is not fully understood and cannot take into account all of the complex two-nucleon residual interactions exhibited by the nucleus. As a result, the Schrödinger equation is only analytically solvable for a few simple nuclei. The current solution to this problem is to adopt models which can approximate the nuclear potential yet still give meaningful insight into this complex and unique system. These models fall broadly into two categories; single-particle and collective.

2.1.2 The single-particle model

The single-particle model treats the motion of independent nucleons as moving in a mean-field potential generated by the interactions of all the other nucleons. The Hamiltonian is given by (2.1.4) where $\hat{H}_i$ represents the potential experienced by each individual nucleon, $V(r)$ is the mean-field nuclear potential and the perturbation term $\hat{h}_{ri}$ corrects for the residual interaction between the nucleons.

$$\hat{H} = \hat{H}_0 + \hat{h}_{ri} \tag{2.1.4}$$

$$\hat{H}_0 = \sum_{i=1}^{A} \hat{H}_i \tag{2.1.5}$$

$$\hat{H}_i = T_i + V(r) \tag{2.1.6}$$

To yield energy eigenvalues for the single-particle orbits and obtain a realistic model that will describe experimentally observed features of the nucleus, the Schrödinger equation must be solved using an appropriate nuclear potential. Two such potentials frequently used within the framework of the single-particle model are the harmonic oscillator and the Woods-Saxon potential [13].

2.1.3 Harmonic oscillator potential

The harmonic oscillator potential allows for an analytical solution to the Schrödinger equation and is defined as

$$V(r) = \begin{cases} -V_0 \left[1 - \left(\frac{r}{R}\right)^2\right], & \text{for } r \leq R \\ 0, & \text{for } r > R \end{cases} \tag{2.1.7}$$

where V_0 is the depth of the potential well, r is the distance from the centre of the nucleus and R is the nuclear radius. By solving the Schrödinger equation one obtains the energy eigenvalues

$$E_N = \left[N + \frac{3}{2}\right] \hbar\omega, \tag{2.1.8}$$

where N is the principal (and a good[1]) quantum number and each N level (or oscillator shell) exhibits $(N + 1)(N + 2)$ degeneracy. Each oscillator shell must contain states with the same parity π (also a good quantum number) such that

$$\pi = (-1)^N = (-1)^l, \tag{2.1.9}$$

[1]For a given Hamiltonian, a good quantum number is an eigenvalue whose corresponding eigenvectors remain eigenvectors of the operator, with the same eigenvalue, as time evolves. A classical analogy is that of quantities that are conserved over time.

where l is the orbital angular momentum quantum number. The harmonic oscillator is not a realistic potential because $V(r) \to \infty$ as r becomes large. This implies that surface nucleons experience a larger potential than nucleons within the core, which is unphysical. Furthermore, the harmonic oscillator potential does not reproduce the experimentally observed "magic numbers".

2.1.4 Woods-Saxon potential

The Woods-Saxon potential, which describes a more realistic finite potential where $V(r) \to 0$ for $r > R$, is defined by

$$V(r) = \frac{V_0}{1 + e^{\frac{r-R_0}{a}}}, \tag{2.1.10}$$

where a is a measure of the diffuseness of the nuclear surface. The potential also describes a more realistic flat-bottomed potential well; an advantageous feature as nucleons in the core experience no net force ($\nabla V = 0$). The nuclear radius is given by $R_0 = r_0 A^{1/3}$ where $r_0 = 1.2$ fm. The depth of the potential V_0 can be varied to agree with experimentally derived values.[2] This potential does give an excellent approximation of the distribution of nuclear matter in the nucleus, but it does not allow for analytical solutions to the Schrödinger equation; moreover, the experimentally observed magic numbers are not reproduced. However, this potential does lift the degeneracy associated with the harmonic oscillator shells.

2.1.5 The spherical nuclear shell model (SNSM)

The spherical nuclear shell model is the most representative of the single-particle models, and is based on considerable experimental evidence. For instance, there is a greater abundance of elements with certain "magic" neutron numbers where the zero

[2] A typical value for this potential might be $V_0 \backsim 50$ MeV.

electric quadrupole moments for these nuclei are indicative of a spherical nuclear shape. In addition, a discontinuity in the binding energies and the deviation of experimental masses from the liquid drop model[3] at magic nucleon numbers indicate that these magic nuclei are more tightly bound relative to their neighbours.

The central argument of the SNSM is that these relatively tightly bound nuclei with certain nucleon numbers and a spherical nuclear shape correspond to filled nucleonic shells. As nucleons occupying a given orbital tend to form pairs with their angular momentum coupling to zero, magic nuclei are thus a special case of nuclei with an even number of nucleons in the outer shell where all the nucleons are paired.

The Hamiltonian $\hat{H}_i$ for the individual energy states in the SNSM is defined by (2.1.11) and consists of a mean-field non-perturbed Hamiltonian $\hat{H}_{mf}$ which must be corrected with the spin-orbit correction term $c'l \cdot s$.

$$\hat{H}_i = \hat{H}_{mf} - c'l \cdot s \tag{2.1.11}$$

A harmonic oscillator potential represented by $\hat{H}_{ho}$ may also be used (2.1.12); however, an additional surface correction term cL^2 is also required.

$$\hat{H}_i = \hat{H}_{ho} - cL^2 - c'l \cdot s. \tag{2.1.12}$$

Working within the framework of the spherical nuclear shell model, successive single-particle orbitals are filled with nucleons - observing Pauli's exclusion principle - to obtain the ground state of a given nucleus.

A manifestation of the residual interaction term in the single-particle Hamiltonian given by (2.1.4) is the pairing of nucleons; nucleons occupying a given orbital

[3]The liquid drop model approximates the nucleus as a "drop" of nuclear fluid with terms accounting for its volume, surface tension, Coulomb energy, nucleon asymmetry and pairing. The general trend for the binding energy per nucleon is well reproduced except for deviations by light nuclei (where the liquid drop concept is not well suited) and nuclei near closed nucleon shells.

form pairs with total angular momentum coupled to zero due the time-reversal symmetry of their individual orbits. An orbital of total angular momentum j can contain $(2j+1)$ individual nucleons whilst respecting the exclusion principle.

Nuclei with filled proton *and* neutron shells are known as doubly magic nuclei, e.g. ${}^{16}_{8}\mathrm{O}$, ${}^{20}_{40}\mathrm{Ca}$ and ${}^{208}_{82}\mathrm{Pb}$. Figure 2.1.1 shows the single-particle states with the magic nucleon numbers at 2, 8, 20, 28, 50, 82, 126 marked. Spectroscopic notation[4] of the form nl_j is used to label each orbital, where n is the principal quantum number, l is the orbital angular momentum and the spectroscopic labels $s, p, d, f, g...$ correspond to orbital angular momenta of 0, $\hbar$, $2\hbar$, $3\hbar$, $4\hbar$ etc..

Spin-orbit coupling

In order to successfully reproduce the magic numbers observed experimentally, it is necessary to introduce a spin-orbit coupling term to the nuclear Hamiltonian. This term accounts for the coupling of the intrinsic spin $s = \pm\frac{1}{2}$ of the nucleon to its orbital angular momentum l, such that the total angular momentum is defined by the vector sum $j = l + s$. The total angular momentum quantum number for a nucleon in an orbit l is then $l \pm \frac{1}{2}$. With such a coupling, the force experienced by a nucleon differs according to whether its spin and orbital angular momentum are aligned parallel or antiparallel. Thus the degeneracy of each nl state, such as $1g$, is lifted and the level is split into two orbits, $1g_{9/2}$ and $1g_{7/2}$, which are lowered and raised in energy, respectively.

Figure 2.1.2 shows the $l{\cdot}s$ coupling with components projected onto the rotational axis. The angular momenta vectors l and s precess around the vector j, which in turn precesses around the symmetry axis. The projection j_x of the total angular momentum on to the symmetry axis is constant, whereas l_x and s_x will vary. In

[4]The labels s, p, d, f and then g, h, i etc. correspond to *sharp*, *principal*, *diffuse*, *fundamental*, and then continue alphabetically. These historical terms originate from the observed properties of spectral series in alkali metals, dating from before the concept of atomic orbitals was fully understood.

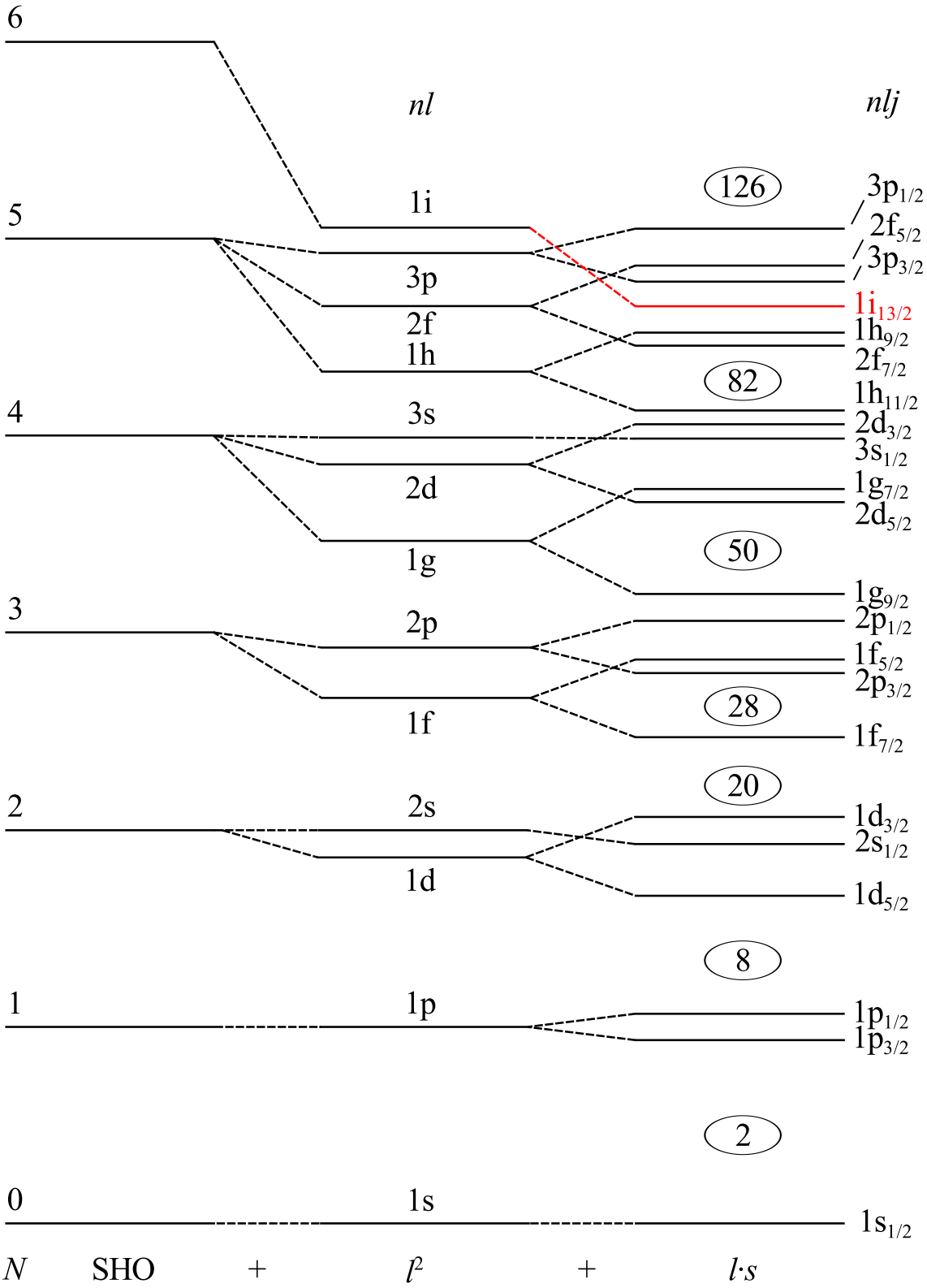

FIGURE 2.1.1: Single-particle states for a simple harmonic oscillator (SHO) potential; a modified harmonic oscillator with an l^2 correction term; and a more realistic shell model potential (e.g. Woods-Saxon) with l^2 and $l \cdot s$ terms. The $i_{13/2}$ intruder orbital is highlighted in red.

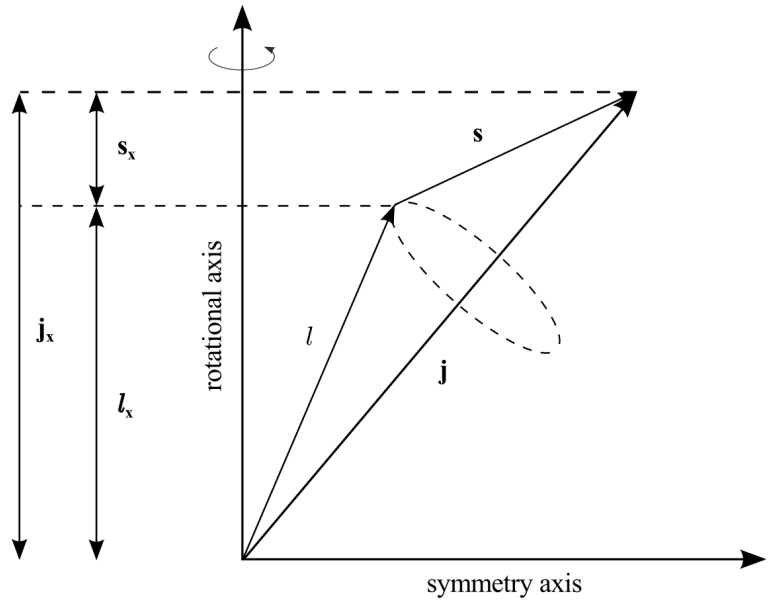

FIGURE 2.1.2: The $l \cdot s$ coupling shown with components projected onto the rotational axis.

order for the $j = l + 1/2$ states to have lower-lying energies than the $j = l - 1/2$ states - as is observed experimentally - the spin-orbit force must be attractive.

The splittings introduced by the spin-orbit coupling are comparable in magnitude to those between adjacent multiplets of the harmonic oscillator potential (see Figure 2.1.1). Thus, the spin-orbit force must be of substantial absolute strength in order to reproduce the correct magic numbers. Indeed, the constant $\hbar\omega_0$ of the harmonic oscillator is found to be $\hbar\omega_0 = 41/A^{1/3}$ (so $\backsim$ 8 MeV for medium and heavy nuclei), ergo the strength of the spin-orbit force must be comparable in magnitude.

The spin-orbit interaction, which is primarily a surface phenomenon [14], takes the form

$$V_{l\cdot s} = -V_{ls}\frac{\partial V(r)}{\partial r} l \cdot s, \tag{2.1.13}$$

where V_{ls} is a strength constant and $V(r)$ is the chosen central potential (e.g. Woods-Saxon) in the Hamiltonian.

The $(2n + l)$ degeneracy of the levels of the harmonic oscillator potential results

in shells containing sets of l values which differ by even numbers. Thus, all levels of a given harmonic oscillator shell must have the same parity. Whilst this is not altered by the addition of a small l^2 correction to the Hamiltonian, the introduction of a spin-orbit term can sufficiently lower the energy of an N-shell high-j orbital ($j = l + \frac{1}{2}$) so that it intrudes into the $(N-1)$ shell - a phenomena required for the reproduction of the magic numbers. These depressed states are know as *unique parity orbits* or *intruder states*, and are of particular importance in understanding regimes of high angular momentum and large deformation. An example of an intruder orbital is the $i_{13/2}$ orbital shown in Figure 2.1.1.

2.1.6 Deformation parameters and nuclear shapes

There is considerable experimental evidence for *static* nuclear deformation; principally that nuclei away from closed shells exhibit large quadrupole moments and rotational bands. The equilibrium shape of a nucleus results from a competition between shell-structure influences, which favour spherical symmetry, and the effects of residual interactions, which give rise to deformation. In closed-shell regions, the shell structure dominates and results in spherically symmetric nuclei.

The deforming power of additional valence nucleons drives the equilibrium shape away from spherical symmetry. For a sufficient number of additional valence nucleons, the nucleus develops an ellipsoidal deformation and collective rotational modes arise.

This *moving* nuclear surface can be characterised by considering the radius vector $R(\theta, \phi, t)$ from the centre of the nucleus to its surface at time t, as an expansion of

spherical harmonics[5] with time-dependent shape parameters as coefficients

$$R(\theta,\phi,t) = R_0\left(1+\alpha_{0,0}+\sum_{\lambda=1}^{\infty}\sum_{\mu=-\lambda}^{\lambda}\alpha_{\lambda,\mu}(t)Y_{\lambda,\mu}(\theta,\phi)\right), \tag{2.1.14}$$

where R_0 is the radius of a sphere with a volume equal to that of an ellipsoidal nucleus and $\alpha_{0,0}$ is introduced to ensure the conservation of volume. The time-dependent amplitudes $\alpha_{\lambda,\mu}(t)$ are tensors, which describe the distortion of the nuclear surface with λ defining the deformation type.

Of particular interest in this investigation is quadrupole deformation ($\lambda = 2$), which causes (2.1.14) to become

$$R(\theta,\phi) = R_0\left(1+\alpha_{0,0}+\sum_{\mu}\alpha_{2\mu}Y_{2\mu}(\theta,\phi)\right), \tag{2.1.15}$$

where $\alpha_{2\mu}$ is the quadrupole deformation tensor. Since the nuclear radius must be real, by applying $R(\theta,\phi,t) = R^*(\theta,\phi,t)$ to (2.1.14) and using $Y^*_{\lambda,\mu}(\theta,\phi) = (-1)^{\mu}Y_{\lambda-\mu}(\theta,\phi)$ (a property of all spherical harmonics), one can show that $\alpha_{2\mu}$ must fulfil the condition $\alpha^*_{\lambda,\mu} = (-1)^{\mu}\alpha_{\lambda-\mu}$ and, therefore, that $\alpha_{2\mu}$ has five independent degrees of freedom; $\alpha_{2,0}$ (since $\alpha_{2,0} = \alpha^*_{2,0}$), and the real and imaginary parts of $\alpha_{2,1}$ and $\alpha_{2,2}$. Explicitly, this gives the coefficients

$$\alpha_{2,2} \qquad \alpha_{2,1} \qquad \alpha_{2,0} \qquad \alpha_{2,-1} \qquad \alpha_{2,-2}, \tag{2.1.16}$$

which describe specific properties of the nuclear shape [15], as detailed in Table 2.1.

For nuclei that exhibit axial symmetry, the quadrupole deformation tensors are

[5]Spherical harmonics of the form $Y_l^m(\theta,\phi)$ are the angular component of the solution to Laplace's equation in spherical coordinates, and thus satisfy the spherical harmonic differential equation.

TABLE 2.1: The specific properties of the nuclear shape associated with the quadrupole deformation tensor $\alpha_{2\mu}$.

Coefficient	Property of nuclear shape
α_{20}	Describes stretching along the z axis with respect to the x and y axes.
α_{22}, α_{2-2}	Describes the relative length of the x axis compared to the y axis, along with the oblique deformation in the $x-y$ plane.
α_{21}, α_{2-1}	Describes an oblique deformation along the z axis.

constrained such that

$$\alpha_{2,2} = \alpha_{2,-2} \qquad\qquad \alpha_{2,1} = \alpha_{2,-1} = 0. \tag{2.1.17}$$

When these are combined with the three Euler angles, which govern the transformation to the intrinsic frame, the nuclear shape can be completely defined. Using the polar coordinates β and γ, the coefficients $\alpha_{2,2}$ and $\alpha_{2,-0}$ can be expressed using an alternative parameterisation, such that

$$\alpha_{2,2} = \frac{1}{\sqrt{2}}\beta \sin\gamma, \tag{2.1.18}$$

$$\alpha_{2,-2} = \beta \cos\gamma, \tag{2.1.19}$$

where

$$\sum_{mu} |\alpha_{2,\mu}|^2 = \beta^2. \tag{2.1.20}$$

The RMS deviation of the nuclear surface from a sphere of radius R_0 is given by the quadrupole deformation parameter β. How this deviation is distributed over the nuclear surface is then given by the triaxiality parameter γ. This allows (2.1.15) to be expressed as

$$R(\theta,\phi) = R_0\left(1 + \sqrt{\frac{5}{16\pi}}\beta\cos\gamma(3\cos^2\theta - 1) + \sqrt{3}\sin\gamma\sin^2\theta\cos 2\phi\right). \tag{2.1.21}$$

Lund Convention

The Lund Convention, shown in Figure 2.1.3, provides a useful framework for describing quadrupole shapes. Axially symmetric shapes appear at γ equal to -120°, -60°, 0° or 60° and correspond to non-collective prolate, collective oblate, collective prolate and non-collective oblate shapes, respectively. The quadrupole deformation parameter β then quantifies the degree to which the structure has become deformed. Figure 2.1.4 illustrates the triaxial deformation of the nuclear surface. Note the angular momentum vector L, which lies in the principal plane formed by the short and intermediate axes.

2.1.7 The Nilsson model

The principal maxim of the shell model is that individual nucleons move in independent orbits due to the mean-field potential produced by the other nucleons. Whilst this may be an accurate model for nuclei with near-magic numbers, there is a wealth of experimental evidence to suggest that many nuclei are not adequately described by a spherical mean-field potential. To describe non-spherical nuclei, one must use a deformed potential (such as the Nilsson potential) in the nuclear Hamiltonian. Non-spherical nuclear shapes provide a certain conceptual difficulty; they require the separation of the motion of individual (valence) nucleons at the Fermi surface from the rotations of the core itself, and these motions can be very different.

A qualitative approach to the Nilsson diagram

The Nilsson diagram shows how the $(2j+1)$ degeneracy of the SNSM (incorporating the spin-orbit and l^2 corrections) is relieved as a function of quadrupole deformation. Consider a single valence nucleon orbiting a prolate-deformed nucleus in an equatorial plane, as shown by orbit Ω_1 in Figure 2.1.5. Now consider that this nucleus can

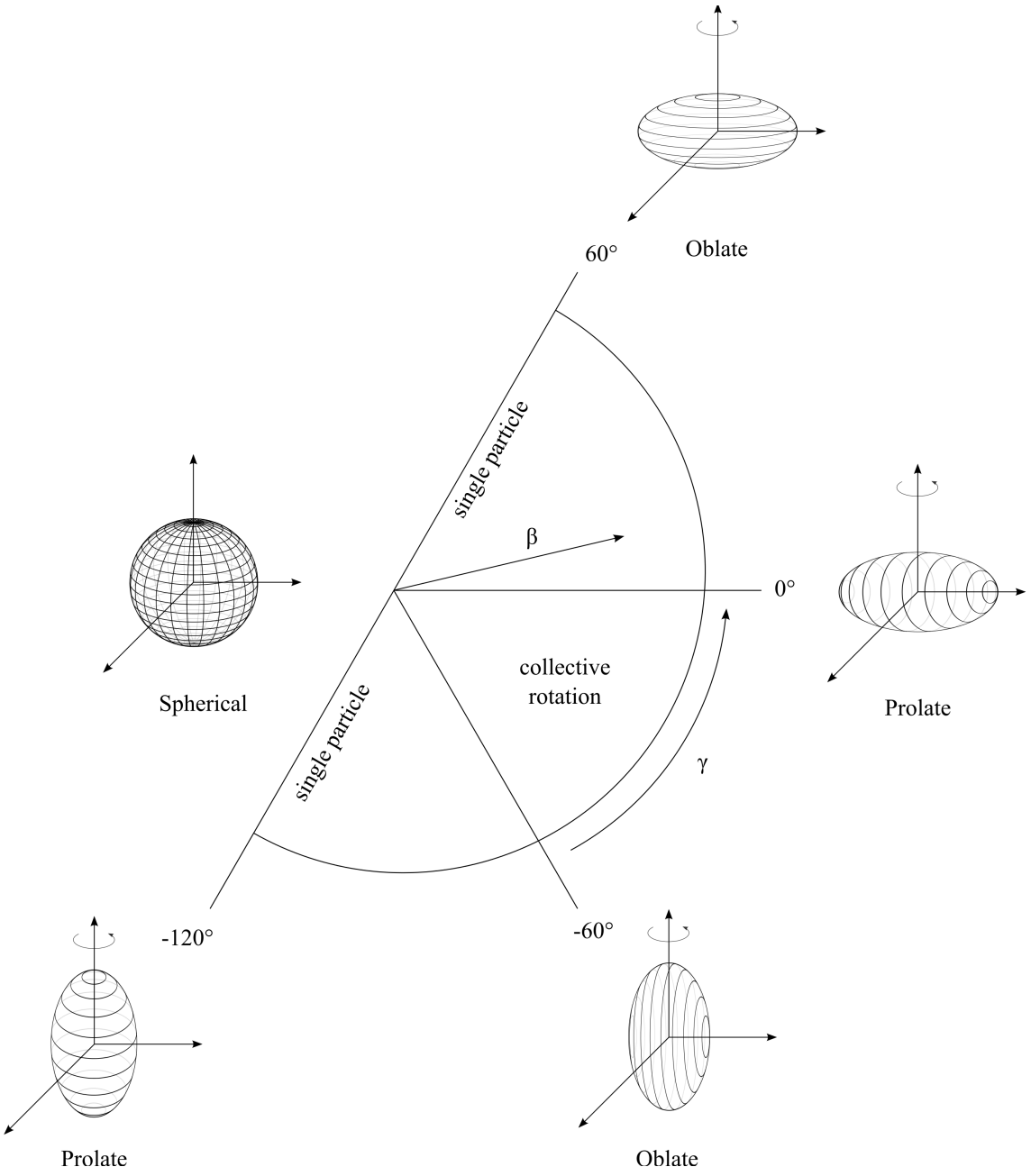

FIGURE 2.1.3: The Lund Convention for describing nuclear shapes.

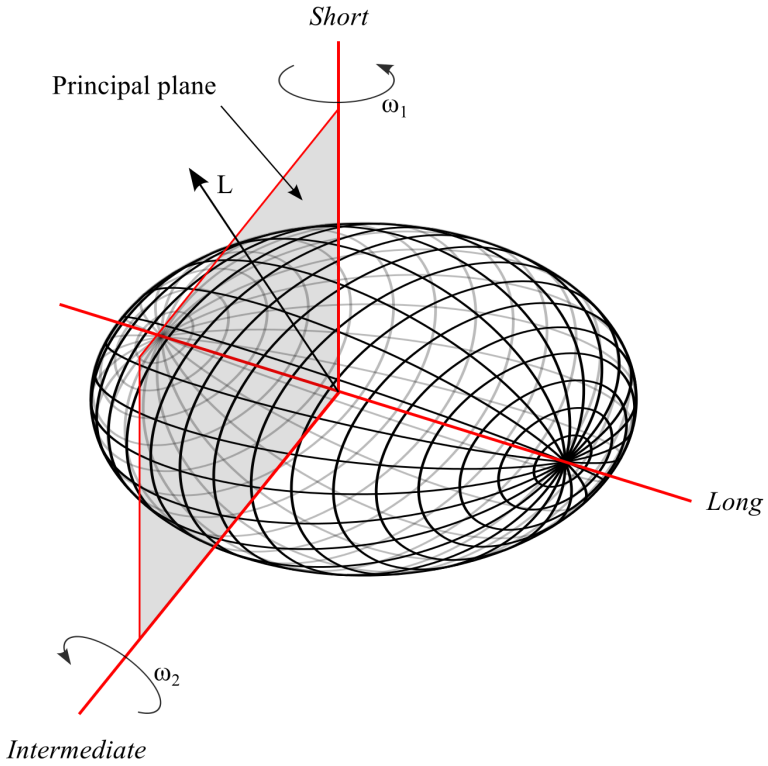

FIGURE 2.1.4: Triaxial deformation of the nuclear surface, with the angular momentum vector L which lies in the principal plane formed by the short and intermediate axes.

rotate about an axis perpendicular to the symmetry axis. For a rapid rotation the time-averaged shape of the nuclear core has become oblate. The subsequent shape of the single nucleon's orbit is then dependent on the extent to which its motion is coupled to that of the core; that is to say, it is dependent on the separation of the rotational and single-particle degrees of freedom.

For frequencies of nucleonic motion much greater than the frequency of rotation of the core, an approximate separation can be made by assuming that a nucleon performs many orbits of the core during a single nuclear rotation; that is to say, the nucleus can be considered stationary during a single nucleonic orbit. However, to effectively explore nuclei in high-spin states using modern experimental techniques, one can no longer consider these two distinct motions as separate, and must instead explicitly incorporate the effects of coupling to a single-particle rotating core.

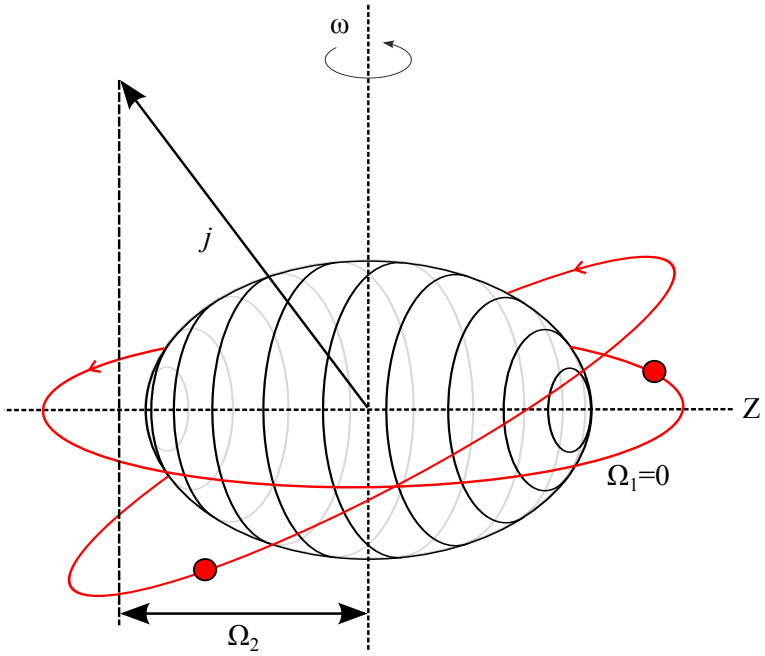

FIGURE 2.1.5: Two single-particle orbitals, Ω_1 and Ω_2, at different inclinations to a prolate deformed nucleus.

To construct a qualitative understanding of the Nilsson diagram and a number of the principal features of the Nilsson wave functions, an intuitive approach is to consider a deformed single-particle potential (such as a shell model potential with a quadrupole deformation β) whilst recognising that the nuclear force is both short-range and attractive.

Consider a valence nucleon in a *single-j* orbital in a prolate deformed potential. The projection of its angular momentum on the symmetry axis is labelled Ω_2 in Figure 2.1.5. It is clear that the Ω_1 orbit must be lower in energy than the orbit labelled Ω_2, as it follows a path with a greater overlap of the core. Thus, the energy of the orbit depends on its *orientation* with respect to the nuclear symmetry axis. This orientation is quantified by the projection of the total angular momentum on the symmetry axis, as shown in Figure 2.1.6 and denoted by the symbol Ω.

Figure 2.1.6 shows the quantum numbers used to describe the projections of the single-particle angular momenta for a deformed rotating nucleus. Note that

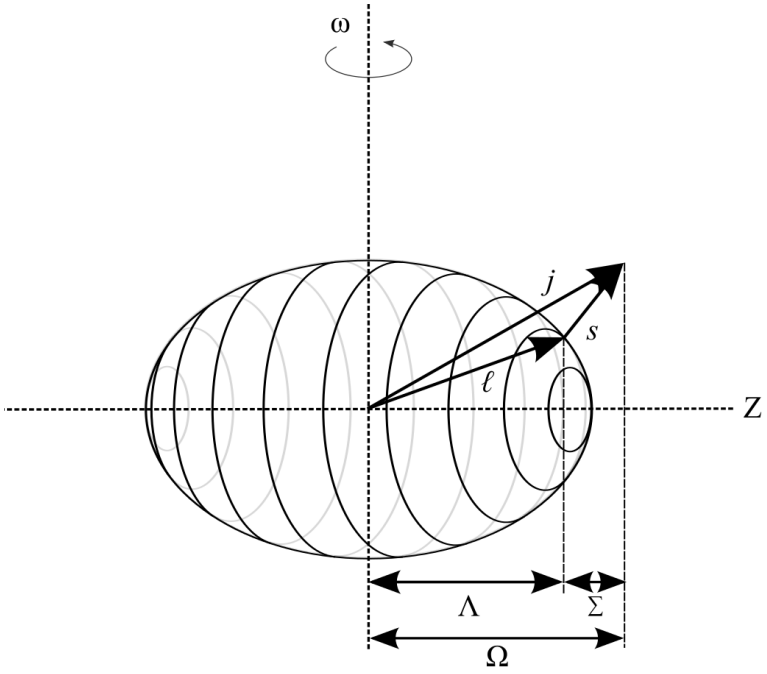

FIGURE 2.1.6: Projections of single-particle angular momenta for a deformed rotating nucleus.

$\Omega = \Lambda + \Sigma$ and $K = \sum \Omega$. As has been shown for a deformed nucleus, the energy of a valence nucleon is dependent on the spatial orientation of its orbit. For j orientated nearly perpendicular to the symmetry axis, Ω is small and the nucleon is said to be in a rotationally aligned (low-Ω) orbit. Conversely, for j orientated nearly perpendicular to the rotational axis, Ω is large and the nucleon is said to be in a deformation-aligned (high-Ω) orbit. The lowest energy orbital for a prolate nucleus is that with the lowest Ω value, and vice versa for an oblate nucleus.

Next consider the classical orbit angles corresponding to varying values of Ω. For the $i_{13/2}$ orbit (i.e. $j = 13/2$), Ω is permitted to have the values $\Omega = 1/2, 3/2, ..., 13/2$. Approximating the angle of the orbital plane using $\theta = \arcsin(\Omega/j)$, one observes that θ changes very slowly for low Ω and more rapidly for high Ω values. Thus, one would expect the energy difference for low Ω values to be small, and to increase rapidly for high Ω values, known as Ω-splitting. This is illustrated in Figure 2.1.7, which shows how the degeneracy of the single-j states is relieved as a function of

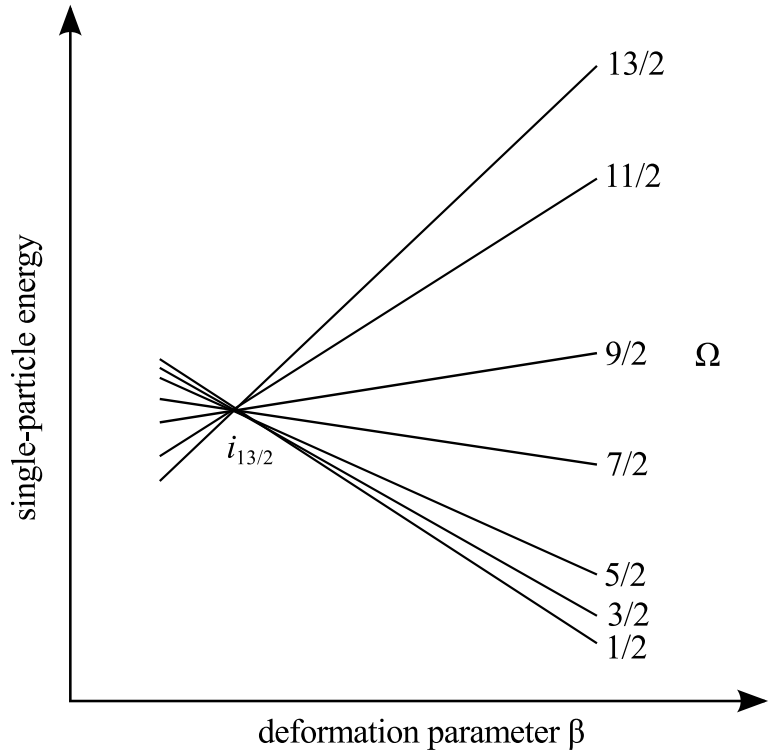

FIGURE 2.1.7: Variation in the single-particle energies of $i_{13/2}$ orbits for different Ω projections as a function of deformation parameter β.

deformation.

To construct the full Nilsson diagram of deformed single-particle energies as a function of deformation, as shown in Figure 2.1.8, the combination of several j values needs to be considered. This requires that the configuration mixing of different j values be superimposed onto the splitting discussed above. Having noted that no two levels with the same quantum numbers may cross, and that the only good quantum number for these orbits is Ω, it then follows that no two lines in the Nilsson diagram (which correspond to the same Ω value and π) may cross. With the understanding that any two such lines approaching each other must repel, it then becomes possible to incorporate many j values into the Nilsson diagram, with the final step being to extend the diagram to realistic deformations where the energies of different orbits will interweave.

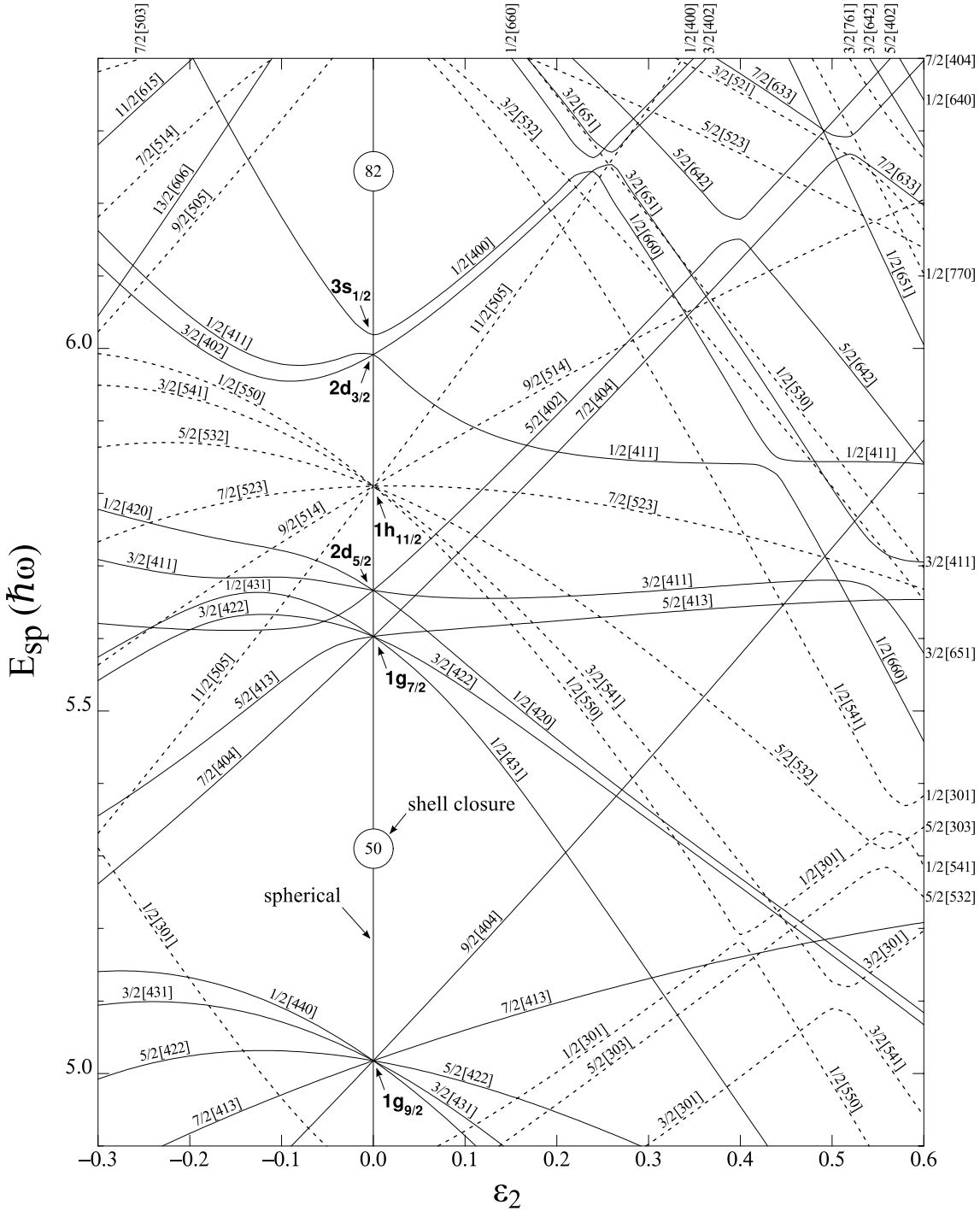

FIGURE 2.1.8: Nilsson diagram for protons in the $50 \leq Z \leq 82$ region. The diagram shows how the degeneracy of the spherical shell model single-particle states is relieved for non-zero values of the quadrupole deformation parameter ϵ_2.

Each line in the full Nilsson diagram represents a single-particle *Nilsson state* and slopes either upwards or downwards, depending on the angle of the orbital relative to the rotating core of the nucleus. A state will only start to curve when it mixes with another state of the same Ω and parity. Thus, the entire structure of the Nilsson diagram is dependent on only three factors; the initial input of single-particle shell model energies (valid only for $\beta = 0$), Ω-splitting (arising from the effects of the short-range nuclear interaction in a non-spherical potential) and the repulsion between individual Nilsson states of the same Ω and π.

The Nilsson or modified oscillator potential

The Nilsson (or axially deformed shell-) model is a single-particle model that provides a microscopic foundation for the existence of rotational and vibrational collective motion. The model uses an anharmonic oscillator with an ellipsoidal potential to calculate the energies of the single-particle orbits.

The Nilsson potential defined by (2.1.22) arises from the anharmonic oscillator potential (2.1.23) for an aspheroidal nucleus deformed along the z-axis.

$$V_{Nilsson} = V_{osc} - \kappa\hbar\omega_0 \left[2(l{\cdot}s) + \mu \left(I^2 - \langle I^2 \rangle_N\right)\right] \tag{2.1.22}$$

$$V_{osc} = \frac{M}{2}\left[\omega_\perp^2 \left(x^2 + y^2\right) + \omega_z^2 z^2\right] \tag{2.1.23}$$

The $(I^2 - \langle I^2 \rangle_N)$ term accounts for nucleons near the nuclear surface - which experience a greater potential than those near the core - by flattening the potential to give it a more realistic shape. The κ and μ coefficients parameterise the coupling strength and are determined by making fits to experimental energy levels; these parameters will be different for each major oscillator shell. To reproduce the shell gaps at magic numbers, the spin-orbit coupling term $l{\cdot}s$ is introduced to lift the degen-

eracy from the $j = l \pm \frac{1}{2}$ orbitals. $\omega_\perp$ and ω_z are the frequency of simple harmonic motions (oscillation) perpendicular and parallel to the axis of symmetry, respectively, and are inversely proportional to the length of the deformed nucleus along each axis. Note that for conservation of volume (assuming the incompressibility of nuclear matter) $\omega_0^3 = \omega_\perp^2 \omega_z$.

The eigenvalues, or Nilsson orbitals, obtained by solving the Schrödinger equation, are then labelled by the asymptotic quantum numbers

$$[N\ n_z\ \Lambda]\Omega^\pi \tag{2.1.24}$$

valid for both large deformation and axially symmetric nuclear shapes where

N = Principal quantum number of major shell,
n_z = Number of nodes in the Nilsson wave function along the z-axis,
Λ = Projection of orbital angular momentum l on the axis of symmetry,
Ω = Projection of total angular momentum j on the axis of symmetry,
π = Parity of the Nilsson state $\left[= (-1)^N\right]$.

The projection Ω of total angular momentum on the axis of symmetry and the parity π are now the only good quantum numbers. N, n_z, and Λ are not good quantum numbers at low deformations and only become good at larger deformations; hence they are said to be to be asymptotic.

Figure 2.1.6 shows the quantum numbers used to describe the projections of the single-particle angular momenta for a deformed rotating nucleus. Note that $\Omega = \Lambda + \Sigma$ and $K = \sum \Omega$. In a deformed nucleus, the energy of a valence nucleon is dependent on the spatial orientation of its orbit. For j orientated nearly perpendicular to the symmetry axis, Ω is small and the nucleon is said to be in a rotationally aligned

(low-Ω) orbit. Conversely, for j orientated nearly perpendicular to the rotational axis, Ω is large and the nucleon is said to be in a deformation-aligned (high-Ω) orbit. The lowest energy orbital for a prolate nucleus is that with the lowest Ω value and vice versa for an oblate nucleus.

Each Nilsson state with $\pm\Omega$ is two-fold degenerate. As the deformation increases and the nucleus moves away from spherical symmetry, the $(2j+1)$ degeneracy of the spherical shell-model states is lifted. For example, in the case of the $1d_{5/2}$ orbital the degeneracy would be lifted to give $(2 \times (5/2))+1 = 6$ discrete energy levels with $\Omega = \pm 1/2, \pm 3/2, \pm 5/2$.

2.1.8 Quadrupole moments

The electric quadrupole moment Q_0 is a quantity which gives a measure of the charge distribution of the nucleus, and hence the deviation of the nucleus away from spherical symmetry. A nucleus exhibiting spherical symmetry would have a quadrupole moment of zero, whilst positive (negative) moments are characteristic of prolate (oblate) deformed shapes. Values of Q_0 are typically expressed in units of 1.6×10^{-43} cm^2 = 1 eb.

The operator corresponding to the electric quadrupole moment is given by

$$\hat{Q}(r) = e \int \rho_e(r) r \left(3\cos^2\theta - 1\right) dV, \tag{2.1.25}$$

where $\rho_e(r)$ is the electric charge density function and θ is the angle subtended by the radius vector r. The (intrinsic) quadrupole moment is then defined as the expectation value of $\hat{Q}$ for a nucleus in the state $|I, M\rangle$ as

$$Q_0 = \langle I, M | \hat{Q}(r) | I, M \rangle , \tag{2.1.26}$$

where I is the total angular momentum of the nucleus and M is the magnetic quantum number. The intrinsic quadrupole moment can also be related to the quadrupole deformation parameter β by

$$Q_0 = \frac{3}{\sqrt{5\pi}} Z R^2 \beta^2 \left[1 + \frac{1}{8} \sqrt{\frac{5}{\pi}} \beta^2 \right]. \tag{2.1.27}$$

2.1.9 Nuclear transitions

γ-decay within the QED framework

Quantum theory as formulated prior to 1925 is now considered to be more a heuristic collection of incomplete and non-self-consistent corrections to classical mechanics rather than the rigorous mathematical framework with which we are familiar today. These early attempts at a quantum theory could not successfully describe the phenomenon of spontaneous γ-decay, as they did not allow for the electromagnetic field to be properly quantised. As the overlap between the ground state and excited state nuclear wave functions is zero, a nucleus cannot decay between these states in the absence of a quantised electromagnetic field. The extension of quantum mechanics to a quantum field theory, in which the electromagnetic field is quantised at every point in space, is described using quantum electrodynamics (QED). Within this framework, the electromagnetic field has a fluctuating ground state, the QED vacuum, which can mix with the stationary states of the nucleus and thus induce a decay via γ-ray emission.

All nuclei with bound excited states exhibit γ-ray decay due to this nucleus-electromagnetic field interaction; an excited nucleus will lose energy via the emission of a γ-ray photon of energy E_γ equal to the transition energy between the initial and final nuclear states[6], typically between 0.1 and 10 MeV.

[6]This is neglecting the recoil energy of the emitting nucleus; a reasonable assumption, as the recoil momentum transfer is usually approximately 1 part in 10^5.

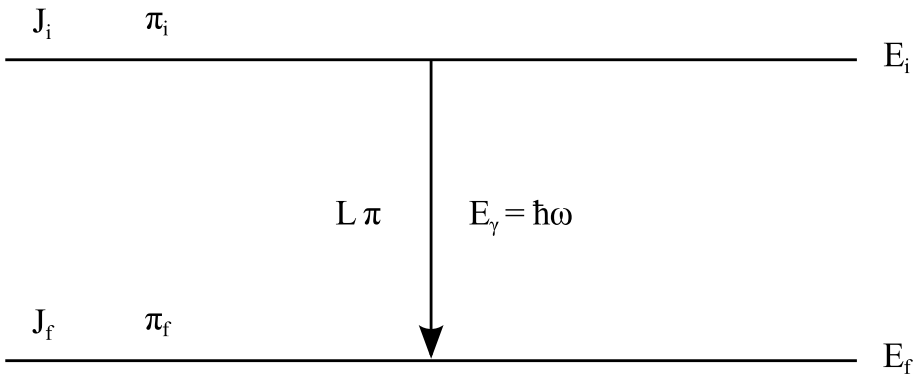

FIGURE 2.1.9: Diagram showing the initial and final spins, parities and energies for an electromagnetic transition.

This electromagnetic radiation is quantised - the emitted photon must have a discrete energy and angular momentum - and is emitted as oscillations of electric or magnetic moments. An oscillating electric charge distribution (due to proton motion) coupled with the external electric field generates the emission of electric EL-type radiation. Likewise, the coupling of the intrinsic magnetic moment of a nucleon with the magnetic field - induced by current loops due to proton orbitals - generates the emission of magnetic ML-type radiation. Magnetic transitions are thus sensitive to nuclear magnetic moments and so yield information about the single-particle properties of the nucleus. Conversely, electric transitions are sensitive to the nuclear charge distribution and so yield information about collective effects such as deformation.

Selection rules

The electromagnetic transitions between two states - as shown in Figure 2.1.9 - observe the angular momentum and parity π selection rules give by (2.1.28) and (2.1.30), where L is the multipolarity of the emitted radiation.

$$|J_i - J_f| \leq L \leq J_i + J_f \tag{2.1.28a}$$

$$L_{min} = |J_i - J_f| \tag{2.1.28b}$$

Multipolarity is a measure of the angular momentum carried away by the photon. A photon with l units of angular momentum is a 2^l-pole photon, i.e. $l = 1$ corresponds to a dipole, $l = 2$ to a quadrupole and $l = 3$ to an octupole. The parity of a given state is given by

$$\pi = (-1)^l, \tag{2.1.29}$$

where l is the corresponding orbital angular momentum quantum number. The change in parity for a transition of given type - electric (EL) or magnetic (ML) - and multipolarity is thus given by

$$\Delta\pi(EL) = (-1)^L \qquad \Delta\pi(ML) = (-1)^{L+1} \tag{2.1.30}$$

Note that L cannot be equal to zero. As the photon has an intrinsic spin of 1, it must take away a minimum angular momentum of $L = 1$.

2.1.10 Summary of nuclear models

Thus far, this chapter has discussed a series of corrections to the spherical nuclear shell model which contribute to a significantly more realistic nuclear model. These corrections are illustrated schematically in Figure 2.1.10. This figure shows how an axial deformation of the nuclear shape relieves the degeneracy of the spherical shell model states, and how an interplay of centrifugal and Coriolis forces gives rise to new symmetries in the nuclear Hamiltonian (π, α). These concepts provide a foundation for the understanding of nuclear rotations which are fundamental to the results presented in this thesis.

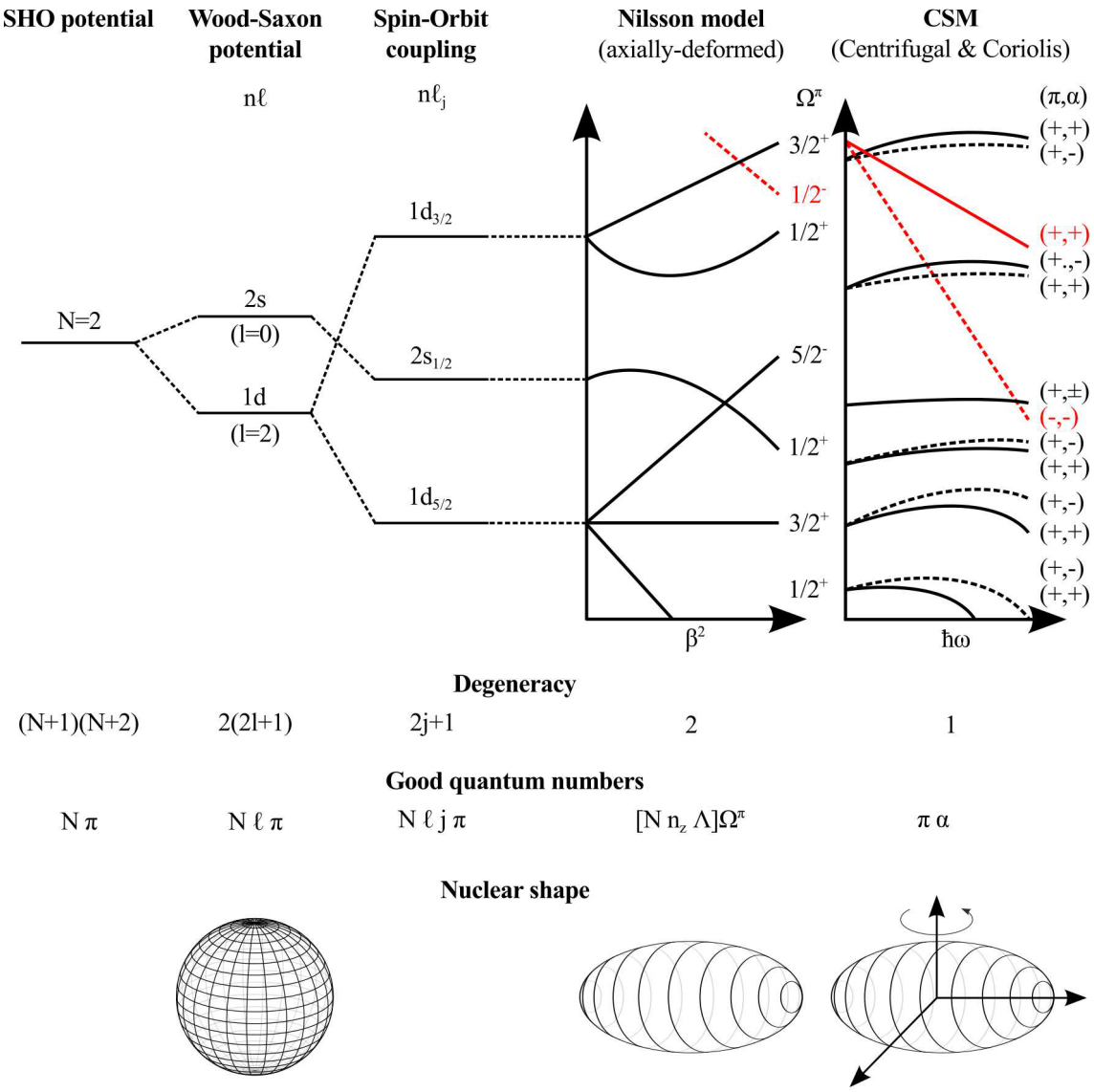

FIGURE 2.1.10: Corrections made to the spherical shell model which produce increasingly realistic models. The lifting of $(N+1)(N+2)$ degeneracy associated with the $N = 2$ oscillator shell is illustrated schematically for each model, along with the respective degeneracy and the remaining good quantum numbers. Each regime is then characterised by the nuclear shape shown at the bottom of the figure. The $1/2^-$ intruder state (shown in red) is the negative-parity $2p_{1/2}$ orbital of the $N = 3$ oscillator shell, which is lowered in energy by the spin-orbit interaction to lie below the $N = 2$ $3/2^+$ Nilsson state.

2.2 Collective nuclear rotation

2.2.1 Collective motion

Collective excitations arise from the coherent motion of constituent nucleons. It is this coherent motion of nucleons which leads to nuclear deformation and the collective rotational and vibrational degrees of freedom. These collective excitations result in regular sequences of excited states constituting rotational bands. As nucleons are added to (or removed from) a closed shell, polarisation of the mean-field potential, or *core polarisation*, removes spherical symmetry and the nucleus can take on a deformed equilibrium shape.

2.2.2 Particle-core coupling and the particle-rotor model (PRM)

The particle-rotor model was first introduced as an angular momentum-conserving phenomenological description of odd-A deformed nuclei. Originally formulated for axially symmetric nuclei, notable extensions to the model now allow for the description of triaxial deformation [16].

More specifically, the model describes a coupling between the single-particle motion of a small number of independent nucleons to a deformed nuclear core. This coupling can occur between two extreme regimes; the rotation-alignment limit (RAL) and the deformation-alignment limit (DAL). Figure 2.2.1 illustrates these two regimes.

The particle-rotor system will approach the rotation-aligned limit for rapid rotation and smaller deformations. In this regime, the Coriolis force exerts a strong influence on the valence-nucleon orbitals and aligns the angular momentum of the nucleon(s) with the axis of rotation. The angular momentum vector J now precesses

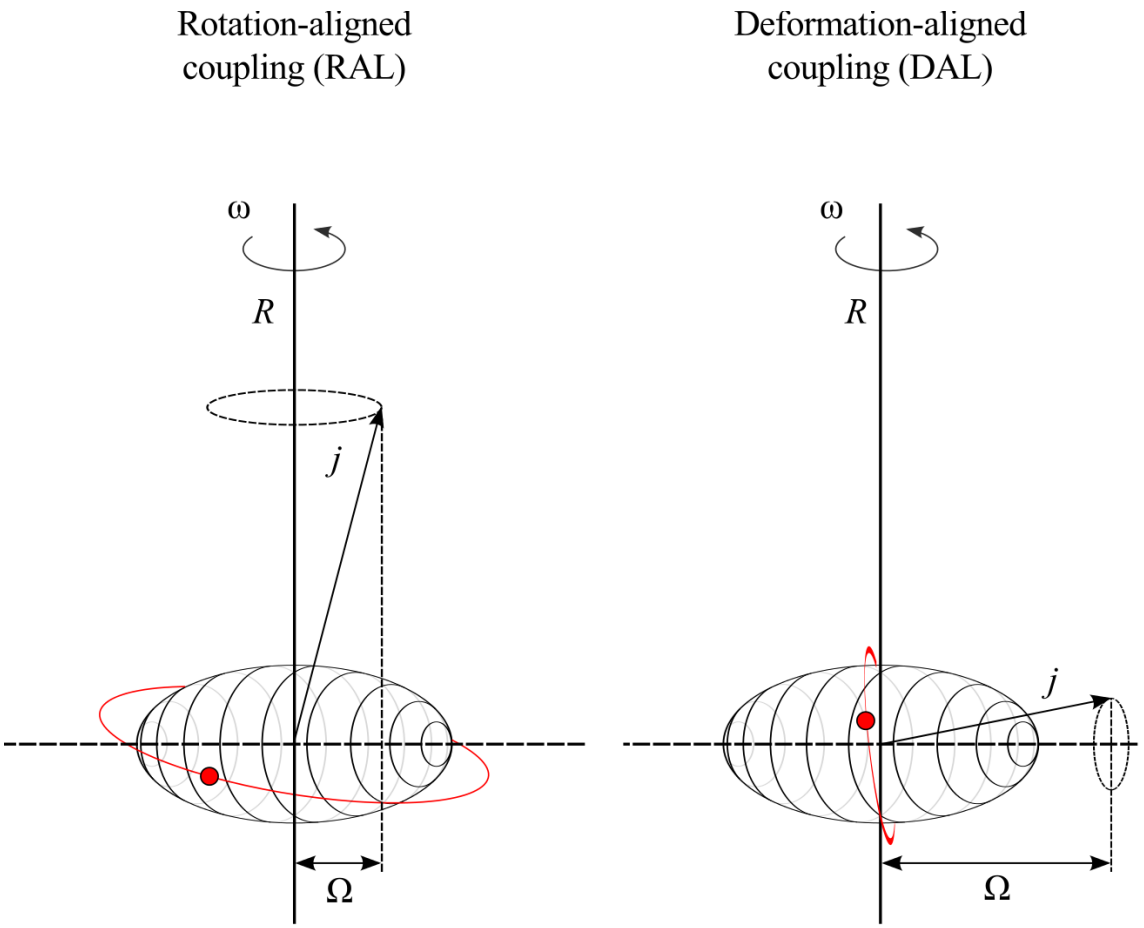

FIGURE 2.2.1: Angular momentum coupling of the single-particle motion of a valance nucleon to a deformed core. The symmetry axis is perpendicular to the rotational axis and indicated by the dashed line.

about the rotation axis and the orbit of the nucleon lies in the symmetry plane.

For low rotational frequencies and larger deformations, the deformation-aligned limit is approached. In this case, the Coriolis force is too weak to align the single-particle orbits with the axis of rotation. The single-particle Routhians have become near-degenerate levels and exhibit minimal staggering.

Coriolis coupling

Classically, a particle of mass m moving with velocity ν in a rotating reference frame with angular momentum Ω appears to be influenced by an additional force

term $\hat{F} = -2m(\Omega \times \nu)$, known as the Coriolis force [17]. In nuclei, Coriolis effects arise due to the orbital motion of valence nucleons in the field of a rotating nuclear core. The resulting Coriolis force will always act to align the angular momenta of these valence nucleons along the rotational axis of the core. The effect is most pronounced where valence nucleons occupy high-j orbitals.

Assuming a rigid, axially symmetric deformed core, a simple Hamiltonian for a deformed odd-A nuclei is given by

$$\hat{H} = \hat{H}_{in} + \hat{H}_{rot}, \tag{2.2.1a}$$

$$\hat{H}_{rot} = \hat{H}^0_{rot} + \hat{H}_{Coriolis}, \tag{2.2.1b}$$

where $\hat{H}_{in}$ corresponds to the intrinsic valence odd-particle Hamiltonian in the absence of any core rotation, and $\hat{H}_{rot}$ corresponds to an even-even axially symmetric rotor. $\hat{H}^0_{rot}$ and $\hat{H}_{Coriolis}$ are purely rotational and Coriolis terms, respectively. It is important to distinguish between the particle-*core* coupling, which is contained within $\hat{H}_{in}$, and the particle-*rotation* coupling, which is contained within $\hat{H}_{rot}$. The major contribution to the coupling between valence nucleons and the nuclear *core* is spherically symmetric, and not central to this discussion; however, for a core which is deformed, there is then a coupling to the deformation which must be considered. For nuclei exhibiting large deformation and strong particle-core coupling, valence nuclei will follow the core as it rotates. Coriolis effects are then observable as perturbations to the purely rotational spectra.

The coupling between valence nucleons and the nuclear core *rotation*, however, arises from their sharing of the total angular momentum of the core-particle system.

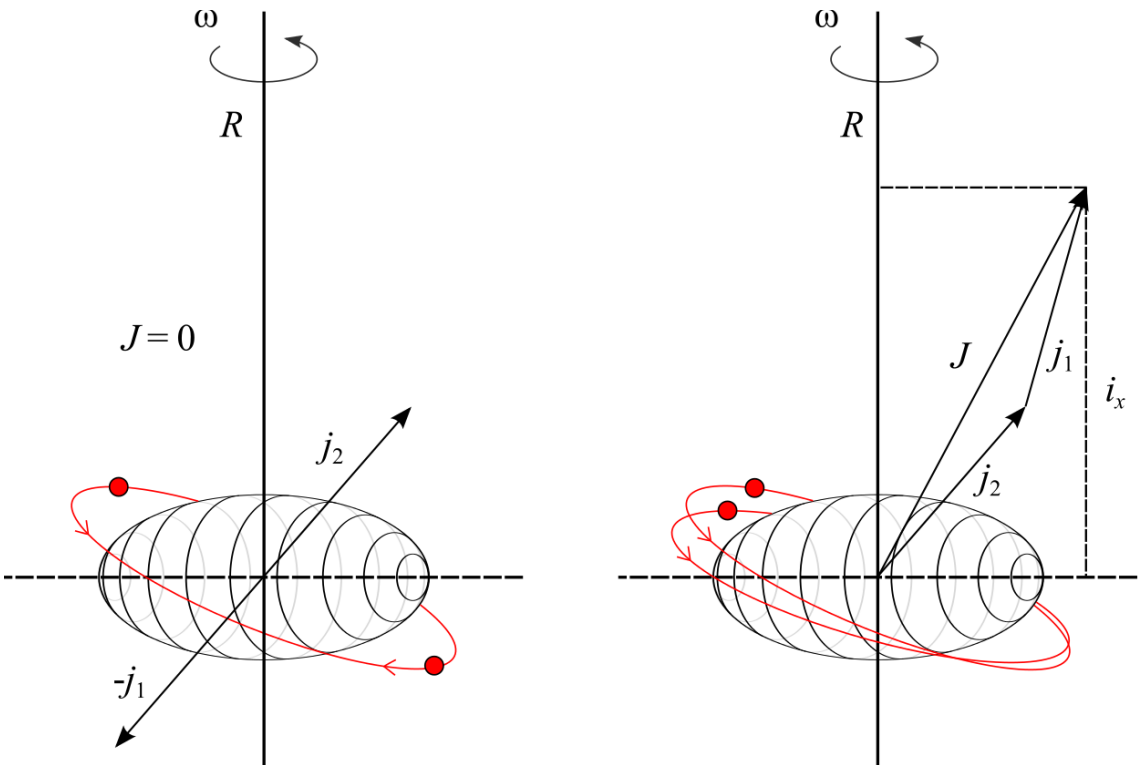

FIGURE 2.2.2: A pair of valence nucleons in time-reversed orbits (left) with angular momentum coupled to zero. As spin is increased the pair recouples (right), such that their angular momenta are aligned with the rotational axis. The symmetry axis is perpendicular to the rotational axis and indicated by the dashed line.

Rotation-aligned coupling RAL

At high spin, the Coriolis and centrifugal forces break the time-reversal symmetry of valence nucleon pairs and align the orbital angular momenta vectors j_1 and j_2 with the rotational axis. Figure 2.2.2 shows a pair of valence nucleons in time-reversed orbits (left) with angular momentum coupled to zero. As spin is increased the pair recouples (right), such that their angular momenta are aligned with the rotational axis.

The aligned angular momentum I of a rotating deformed nucleus is given by (2.2.2), where R is the collective angular momentum due to the rotation of the core and J is the sum of the intrinsic single-particle angular momenta of the valence

nucleons.

$$\hat{I} = \hat{R} + \hat{J} \tag{2.2.2}$$

If the axis of symmetry is chosen as the z-axis then R will be perpendicular to it, and the projection of I and J will be equal and denoted by K.

The rotational alignment i_x [18, 19] is quantified as the projection on the axis of rotation of the vector sum of the angular momentum of the valence nucleons $J = \sum j$, and is given by (2.2.3).

$$i_x = \sqrt{I(I+1) - K^2} - I_{ref} \tag{2.2.3}$$

I_{ref} is the total aligned angular momentum of a reference configuration and is used to subtract the rotation of the nuclear core, such that the first rotational band exhibits almost constant alignment at low spin.

The aligned configuration will have an angular momentum greater than that of the rotational band constructed with all the nucleons paired. On a plot of angular momentum as a function of frequency, this is seen as *backbending* at the crossover frequency ω_c at which the alignment occurs. This backbending is interpreted as the crossing of two distinct rotational bands, each with their own intrinsic configuration. The sharpness of the backbending corresponds to the strength of the interaction between the two crossing bands, with a steeper slope indicating a stronger interaction.

2.2.3 The cranked shell model (CSM)

The cranking model was originally introduced [20, 21] within the framework of a single-particle model, and approximated the collective motion of nucleons (associated with a change in nuclear shape) through the introduction of a non-spherical distortion to the zero-order wave functions of the shell model. This model was later extended [22] so as to be based on the self-consistent mean-field theory of a deformed

rotating body.

A further reformulation [23] of the self-consistent cranking model is the cranked shell model (CSM); this variation exhibits a greatly increased applicability over previous models, and is widely used in the analysis of band crossing and other high-spin nuclear phenomena [16]. This formulation, which applies to well-deformed axially symmetric nuclei and is used in this work, is known as principal-axis cranking (PAC), and assumes that collective rotations occur about a principal axis which is perpendicular to the axis of symmetry.

The CSM assumes a set of independent nucleons moving in a time-dependent potential $\bar{\nu}(x, y, z, t)$, which is non-invariant under rotation. This potential consists of a time-independent potential $\nu(x_1, x_2, x_3)$, which is given a constant angular velocity ω, or *cranked* about a fixed axis. The wave function of a nucleon in the laboratory frame (x, y, z) is given by $\bar{\Psi}(x, y, z, t)$, and in the rotating frame (x_1, x_2, x_3) by $\Psi(x_1, x_2, x_3, t)$. The rotation operator $\hat{R} = e^{-iwjt}$ is then defined such that (2.2.4) transforms the wave function of the nucleon from the laboratory frame to the rotating frame (2.2.5) with angular momentum j,

$$\bar{\Psi} = \hat{R}\Psi, \tag{2.2.4}$$

$$\bar{\Psi}(x, y, z, t) = e^{-iwjt}\Psi(x_1, x_2, x_3, t). \tag{2.2.5}$$

The time-dependent Schrödinger equation

$$i\hbar\frac{\partial}{\partial t}\bar{\Psi}(x, y, z, t) = \hat{h}\bar{\Psi}(x, y, z, t) = E\bar{\Psi}(x, y, z, t), \tag{2.2.6}$$

with the single particle Hamiltonian given by

$$\hat{h} = t + \bar{\nu}(x, y, z, t), \tag{2.2.7}$$

can thus be transformed into the time-independent Schrödinger equation

$$\begin{aligned} i\hbar\frac{\partial}{\partial t}\hat{R}\Psi &= i\hbar\frac{\partial}{\partial t}e^{-iwjt}\Psi(x_1,x_2,x_3,t), \\ &= (\hat{h}-\hbar\omega j)\Psi(x_1,x_2,x_3,t), \\ &= \hbar^{\omega}\Psi(x_1,x_2,x_3,t), \end{aligned} \tag{2.2.8}$$

in the rotating frame with the cranking one-particle Hamiltonian or Routhian operator, given by

$$\hbar^{\omega} = \hat{h} - \hbar\omega j. \tag{2.2.9}$$

This allows for the single-particle excitation energies in the rotating reference frame, or *Routhians*, to be determined. Summing (2.2.9) over all independent particles in the system gives the total cranking Hamiltonian

$$H^{\omega} = \hat{H} - \hbar\omega J, \tag{2.2.10}$$

where the use of capitals denotes summed quantities corresponding to a system of many independent nucleons, i.e. a nucleus.

2.2.4 Signature splitting

In the CSM, the nucleon states are described by two symmetry quantum numbers; signature α which defines the allowed spin sequence for a band through the relation $I = \alpha + 2n$ $(n = 0, 1, 2, ...)$, and parity π. Signature is related to the invariance of a system with quadrupole deformation under a rotation of 180° around a principal axis. For an axially symmetric system, the signature quantum number can therefore only be defined by a rotation around any principal axis other than the symmetry axis [24]. Hence, signature is a consequence of the deformation of a system, and corresponds to a deformation invariance with respect to space and time [25]. As

the single-particle Routhian $\hat{h}^{\omega}$ is invariant under a rotation $\hat{R}_x = e^{-i\theta j x}$ around the x-axis by an angle θ, the single-particle states may then be classified according to their symmetry with respect to the rotation $\hat{R}_x(\theta)$,

$$\hat{R}_x|\alpha i_x\rangle = e^{-i\theta j_x}|\alpha i_x\rangle = e^{-i\theta\alpha}|\alpha i_x\rangle \qquad \alpha = \pm\frac{1}{2}. \tag{2.2.11}$$

This symmetry of the nuclear wave function with respect to $\hat{R}_x(\theta)$ allows for a relationship to be established between the states separated by $\Delta I = 2$. For *odd A* nuclei, the energetically favourable signature α_f is lowered relative to the unfavoured signature α_u, where j is the angular momentum of the odd nucleon.

$$\alpha_f = \frac{1}{2}(-1)^{j-\frac{1}{2}} \qquad \alpha_u = \frac{1}{2}(-1)^{j+\frac{1}{2}} \tag{2.2.12}$$

The experimental *signature splitting* $\Delta e'$ is then defined as the energy difference at a given rotational frequency between the favoured and unfavoured signature sequences of a rotational band. As this energy difference is often very small (especially in the case of some axially prolate deformations), an energy staggering index or *staggering parameter* is introduced to provide a more usable measurement [26]. The staggering parameter $S(I)$ as a function of spin is thus defined by

$$\begin{aligned} S(I) = E(I) - E(I-1) - 1/2[E(I+1) \\ - E(I) + E(I-1) - E(I-2)], \end{aligned} \tag{2.2.13}$$

where $E(I)$ is the excitation energy of a state I. A large degree of signature splitting (and hence a large staggering parameter) in a high-Ω orbital is indicative of triaxial deformation and minimal splitting (and hence a small staggering parameter) of an axial prolate deformation [3].

For odd-A nuclei, states with angular momentum $I = 1/2, 5/2, 9/2, ...$ correspond

to $\alpha = +1/2$, and the states $I = 3/2, 7/2, 11/2, ...$ correspond to $\alpha = -1/2$. These two sequences form independent decay paths along the yrast line with cascades of $E2$ transitions.

2.3 Nucleonic configurations

Central to this work is the concept that a given isotope can exist in different states with valence nucleons coupled in certain configurations, depending on the excitation energy and spin angular momentum of the nucleus. The specific nucleon orbitals which are then involved in forming such couplings have a dramatic effect on the nuclear shape and deformation properties. For example, the rotational alignment of a pair of $i_{13/2}$ neutrons at high spin will drive the nuclear shape towards prolate deformation, whereas an odd-proton in the $\pi h_{11/2}$ orbital at low spin is characteristic of triaxial deformation.

A nucleus formed at a given excitation energy and spin (for example in a fusion evaporation reaction) will have its valence nucleons coupled into a given configuration. As the nucleus loses energy and spin through the emission of γ radiation, its valence nucleons will then recouple into more energetically favourable configurations, accompanied by any corresponding change in nuclear shape. The energy levels (between which these γ-ray transitions occur) associated with a given configuration then form band structures characteristic of that configuration. Take, for example, a rotationally excited nucleus, where the excitation energies (which will generally be lower in energy than those which occur due to single-particle excitations) form bands of levels which satisfy the relation

$$E_{rot} = \frac{\hbar^2}{2\mathcal{J}} I(I+1), \tag{2.3.1}$$

where $\mathcal{J}$ is the moment of inertia. This chapter briefly discusses a range of nuclear

phenomena which underpin the work undertaken in this thesis, and these are: band crossing (2.3.1), configuration mixing (2.3.2) and backbending (2.3.3).

2.3.1 Band crossing

Consider an excited band with a greater moment of inertia than that of the ground band. The energy levels in the excited band increase more slowly with J and at sufficiently high spin, levels with a given J can occur lower in energy than levels of the same spin in the ground band. Alternatively phrased, the lowest energy states of a given spin (the yrast states) become those of an excited configuration. This phenomenon is known as *band crossing* (see Figure 2.3.1). This is best thought of as an interaction region with an apparent crossing (see Figure 2.3.2) and a recoupling of nucleons into a new configuration.

2.3.2 Two-state mixing

When two bands cross they either interact or mix. Mixing occurs when levels of the same spin and parity lie close in energy and repel each other due to the exclusion principle. Consider the simple case of two states from the ground and excited bands in the crossing region, as indicated in Figure 2.3.1. The (perturbed) wave functions corresponding to each observed state ψ_0 and ψ_1, shown in Figure 2.3.2, can be written as a linear combination of the pure wave functions ϕ_0 and ϕ_1, corresponding to the ground configuration state and the excited configuration state, respectively. This gives

$$\psi_0 = \alpha\phi_1 - \beta_0, \qquad \psi_1 = -\beta_1 + \alpha\phi_0, \tag{2.3.2}$$

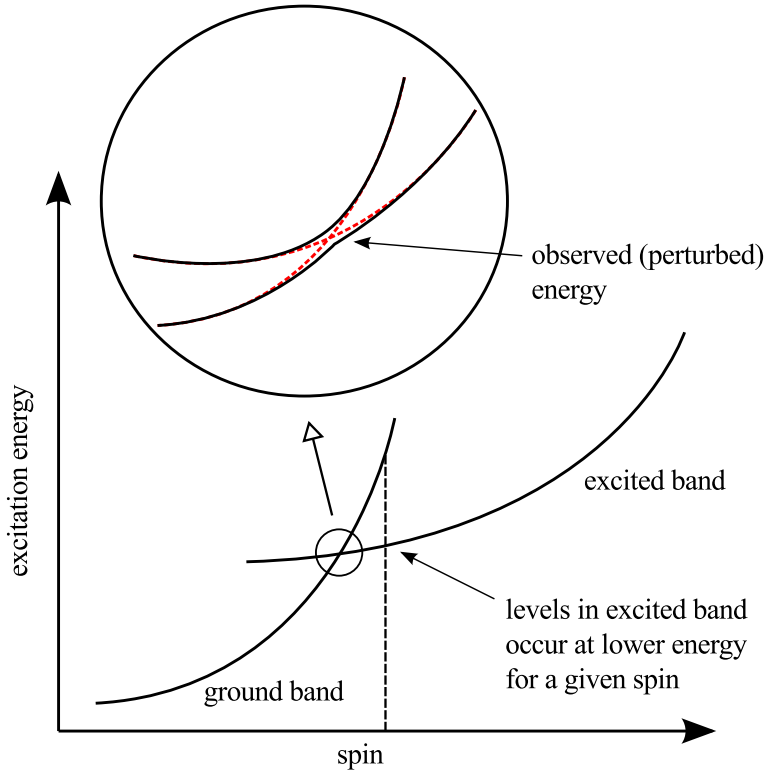

FIGURE 2.3.1: A plot showing the ground and excited bands and their crossing region. The expanded view of a band crossing region shows how the two bands interact - leading to an interchange of the intrinsic nuclear structure - without *explicitly* crossing. The lower solid line (labelled) indicates the observed (perturbed) energy as a result of two-state mixing whilst the dashed red lines indicate the unmixed "pure" energies.

where α and β are the amplitudes of the wave function components such that

$$\alpha^2 + \beta^2 = 1. \tag{2.3.3}$$

The perturbed (observed) energies E_{obv} of the two levels in the crossing region are related to the unperturbed energies through the interaction matrix element V, such that

$$\begin{pmatrix} E_0^- & V \\ V & E_1^+ \end{pmatrix} \begin{pmatrix} \phi_0 \\ \phi_1 \end{pmatrix} = E_{obv} \begin{pmatrix} \phi_0 \\ \phi_1 \end{pmatrix}, \tag{2.3.4}$$

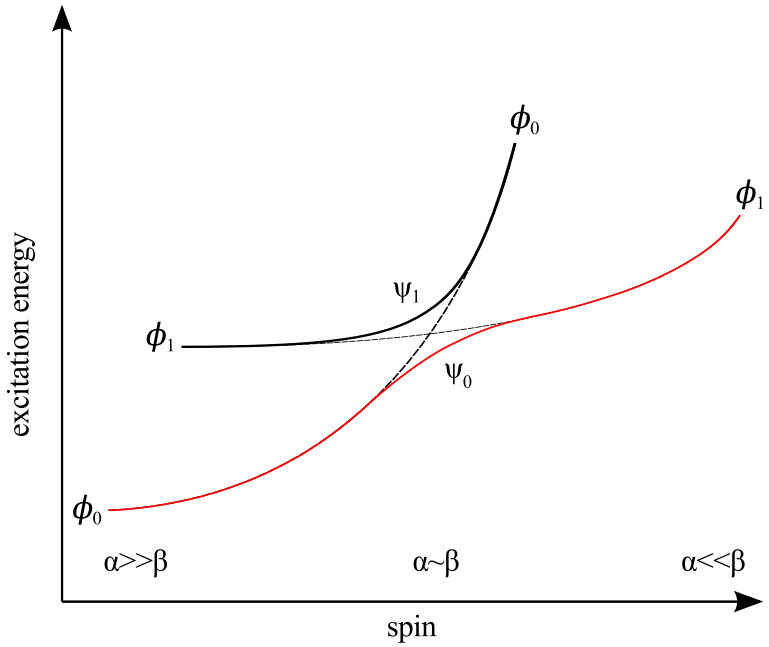

FIGURE 2.3.2: A plot of excitation energy against a given nuclear structure parameter (e.g. spin) shows the inflection point between two admixed states.

where E_0^- and E_1^+ are the unperturbed energies of the upper and lower states, respectively. The two solutions for E_{obv} are then found by rearranging (2.3.4) and diagonalising the resulting matrix, giving

$$E_{1,2} = \frac{1}{2}\left[\left(E_0^- + E_1^+\right) \pm \sqrt{\left(E_0^- - E_1^+\right)^2 + 4V^2}\right]. \tag{2.3.5}$$

2.3.3 Backbending

For a normal rotational band, a plot of $2I/\hbar$ against $\hbar\omega$ is flat or increases slightly for low $\hbar\omega$. This is due to $E_\gamma(J)$ being linear in J and the moment of inertia at low spins being either constant or slightly increasing due to, for example, centrifugal stretching.

At the band crossing, however, there is a more radical change; in the insert in Figure 2.3.1 one can see that, for a narrow range of spins, the γ-ray transition energies between yrast states can actually decrease; as $\hbar\omega = E_\gamma/2$, a plot of $2I/\hbar$

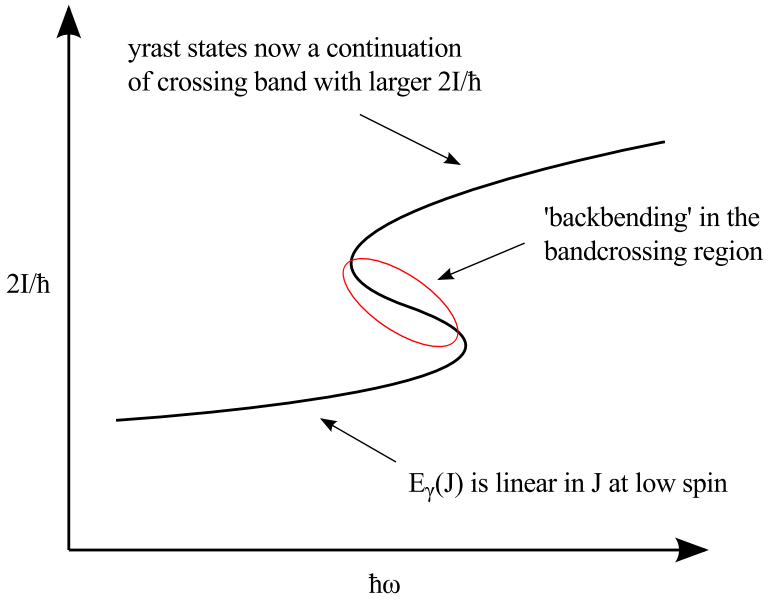

FIGURE 2.3.3: A plot of $2I/\hbar$ against $\hbar\omega$ illustrating the backbending phenomenon.

against $\hbar\omega$ will in fact move "backwards" (i.e. to the left) in the band crossing region, as shown in Figure 2.3.3. However, at J values above the band crossing, the level energies again approach a $J(J+1)$ dependence, and so E_γ (or $\hbar\omega$) increases again with spin (i.e. moves to the right) but at a higher energy (since the yrast states are now a continuation of the crossing band, which has a larger value of $2I/\hbar$).

The sharpness of the backbend is indicative of the strength of the interaction between the different configurations at the crossing. A weaker interaction will be characterised by a backbend which moves sharply to the left, before moving sharply right again as $\hbar\omega$ increases.

Chapter 3

Experimental Apparatus

The study of exotic nuclei far from stability faces a number of challenges for experimental physics. The heavy neutron-deficient nuclei under investigation are produced with low cross-sections in the fusion evaporation reactions used and have to be isolated from high fission γ-ray backgrounds. To overcome this problem, recoil decay tagging is utilised. This technique takes advantage of the distinct α-decay energy of the nucleus under investigation to identify γ-ray transitions between its excited states.

Implantation detection systems (for example the GREAT spectrometer) combined with in-flight recoil separators (for example the RITU gas-filled separator) to suppress fission products and transmit fusion recoils, form one of the most powerful tools available for investigating nuclear phenomena far from stability. Such systems offer efficient separation of the nuclei of interest coupled with sensitive detection of these reaction products and their subsequent radioactive decays. The exploitation of recoil-decay tagging (RDT) techniques has furthermore allowed the spectroscopic study of their excited states to flourish [27].

Figure 3.0.1 shows the experimental apparatus used in this investigation, which consists of three main components: the JUROGAM spectrometer array, which sur-

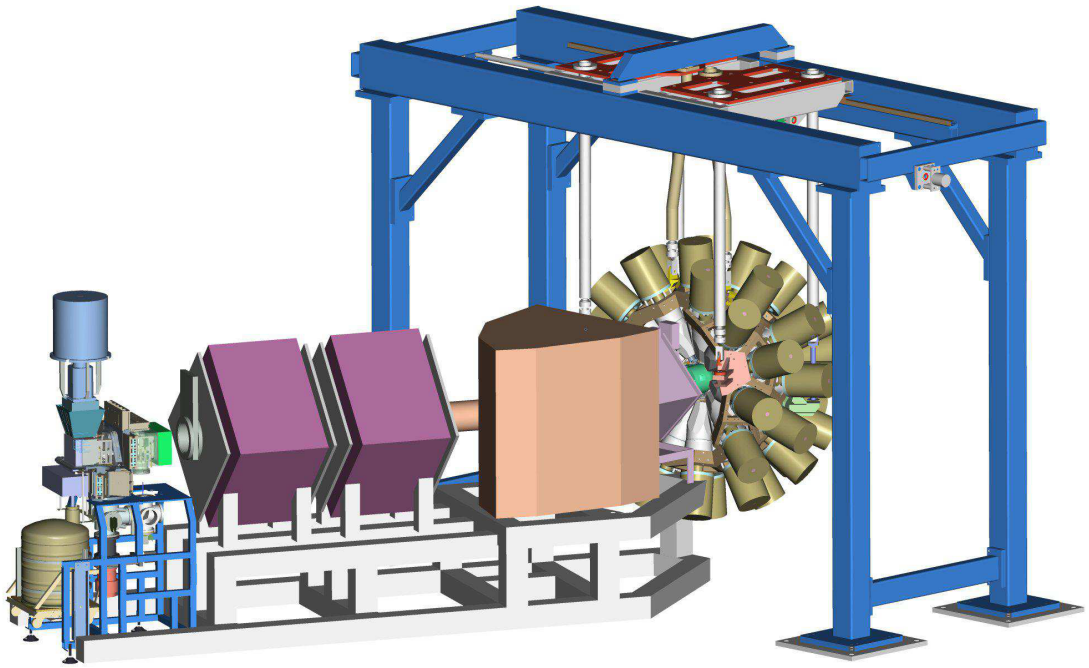

FIGURE 3.0.1: Render of the JUROGAM, RITU and GREAT spectrometer assembly with the beam line incident from right to left. Figure courtesy of Ref.[27].

rounds the target position, the RITU gas-filled recoil separator and the GREAT spectrometer. Using GREAT as a tagging spectrometer in conjunction with a target position prompt γ-ray detector array, a *delayed coincidence technique*, has the limitation of severe deadtime losses in the data acquisition system when using conventional triggering methods. To circumvent this problem, an innovative triggerless total-data-readout (TDR) data acquisition method has been developed for this application [28].

The incident heavy-ion beam enters the JUROGAM detector array and collides with the self-supporting thin foil target, producing a large number of prompt γ rays. Fusion products are then separated in-flight from the scattered beam and other reaction products by the RITU gas-filled separator [29, 30] before being implanted into the double-sided silicon strip detectors (DSSDs) of the GREAT spectrometer [27]. The

triggerless total-data-readout (TDR) data acquisition system is then used to independently record all detector output signals where they are time-stamped with a precision of 10 ns. This allows for accurate temporal correlations between recoil implants and subsequent radioactive decays to be performed using the GRAIN software package [31].

In the off-line analysis, the JUROGAM data is used to produce two-dimensional symmetric matrices from which excited states level schemes can be constructed for the nucleus under investigation using the ESCL8R software package [32].

3.1 Heavy-ion fusion evaporation reactions

Fusion evaporation reactions are the most effective experimental method for giving the largest possible angular momentum to the nucleus of interest [33]. Such reactions involve the collision of a beam of heavy ions with a stationary, self-supporting, thin foil target to produce the compound nuclei with a large density of states. These nuclei are highly excited and will "evaporate" particles to lose energy; the nature of the evaporated particles (i.e. alphas, protons or neutrons) depends on the energy and spin of the compound nucleus. These evaporated particles have a statistical energy spectrum and remove approximately 5-8 MeV per nucleon from the excitation energy of the compound system, whilst only 1-2 $\hbar$ of angular momentum is carried away. Thin foil targets are approximately of the order of 1 mg cm^{-2} and are bombarded by beams of typically a few particle nano-Amps ($\backsim 10^{10}$ particles s^{-1}).

Figure 3.1.1 shows the various types of heavy-ion collision as a function of impact parameter b. Fusion reactions only take place for small values of b, with other reactions occurring at increased target-beam distances. For beam energies around the Coulomb barrier (3-5 MeV A^{-1}) the total fusion cross-sections are typically of the order of 1 barn (10^{-28} m). For heavier nuclei where fission begins to dominate

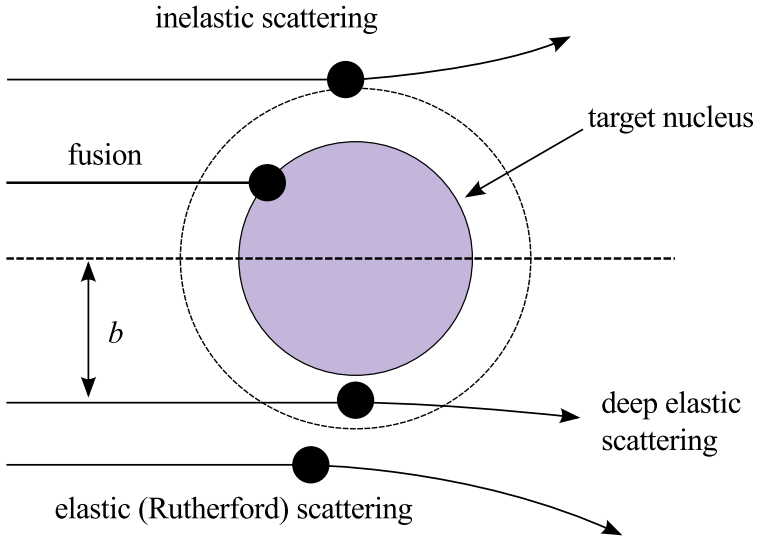

FIGURE 3.1.1: Impact parameter b for various nuclear reaction mechanisms.

over fusion evaporation, the fusion cross section drops dramatically.

Figure 3.1.2 shows the fusion reaction by which a ^{60}Ni nucleus fuses with a ^{106}Cd nucleus in the foil target to produce the highly excited ^{166}Os compound system with a large angular momentum. This compound nucleus is a hot[1] nuclear system with a sufficient lifetime ($> 10^{-20}$ s) to reach thermodynamic equilibrium. During this time the nucleus loses all information on its composition from constituent beam and target nuclei [34]. However, quantities such as total energy and angular momentum are conserved.

A given combination of beam and target will produce compound nuclei which can de-excite via a variety of possible exit channels; an appropriate choice of beam energy may then allow for preferential population of particular channels of interest. The excitation energy and spin of the compound nucleus define its proximity to the yrast line upon formation; thus determining the amount and type of particle evaporation possible and hence the exit channels available for de-excitation.

Figure 3.1.3 shows the typical de-excitation process for a compound nucleus,

[1] A *hot* nucleus is an excited nucleus where its energy is shared between many degrees of freedom.

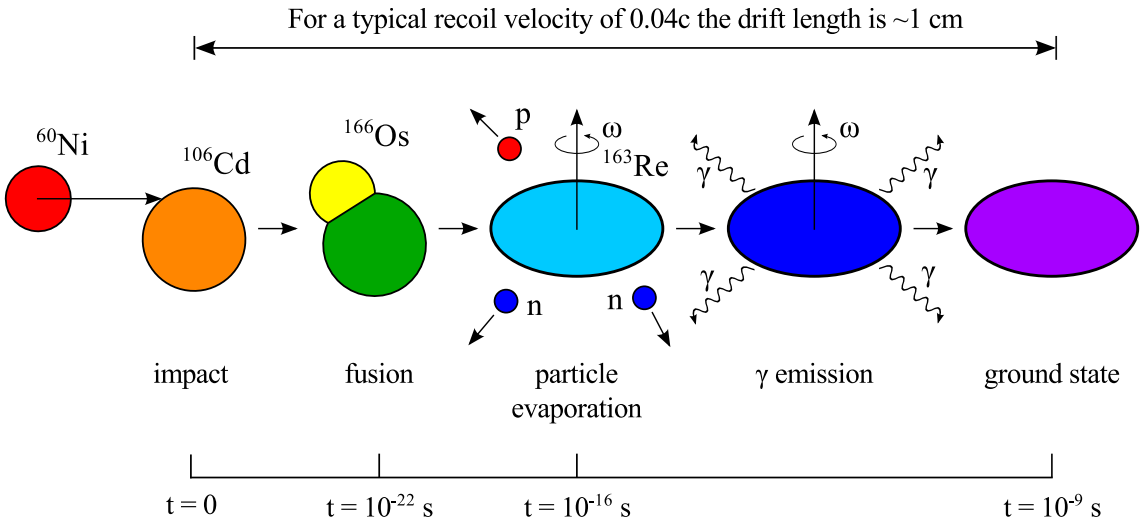

FIGURE 3.1.2: A ^{60}Ni beam nucleus fuses with a ^{106}Cd target to form a ^{166}Os compound system which decays to ^{163}Re via the p2n exit channel. An approximate time scale for each step in the process is given. A typical value for ω would be 2×10^{22} Hz.

using the p2n exit channel as an example. Approximately 10^{-16} s after its formation, the compound system will undergo nucleon evaporation until the nucleus is within a fraction of the proton and neutron separation energies from the yrast line, known as the particle evaporation threshold. At this stage the nucleus is considered to be an *evaporation residue*. The only method by which the newly synthesised nucleon, which is highly excited and with a large angular momentum, can de-excite further (and hence move closer to the yrast line) is now by γ-ray emission. Initially, there is still a relatively high density of states and the resulting transitions do not form resolvable peaks. These emitted γ rays are said to be statistical. As the nucleus de-excites further towards the yrast line, the density of states is much smaller and transitions in this region, known as γ-ray cascades, become resolvable.

Figure 3.1.4 shows the greatest angular momentum obtainable by the compound nucleus for a given energy for different nucleon configurations. As the angular momentum decreases below a certain value for a given configuration, it becomes more energetically favourable for the nucleons to recouple into a new configuration with

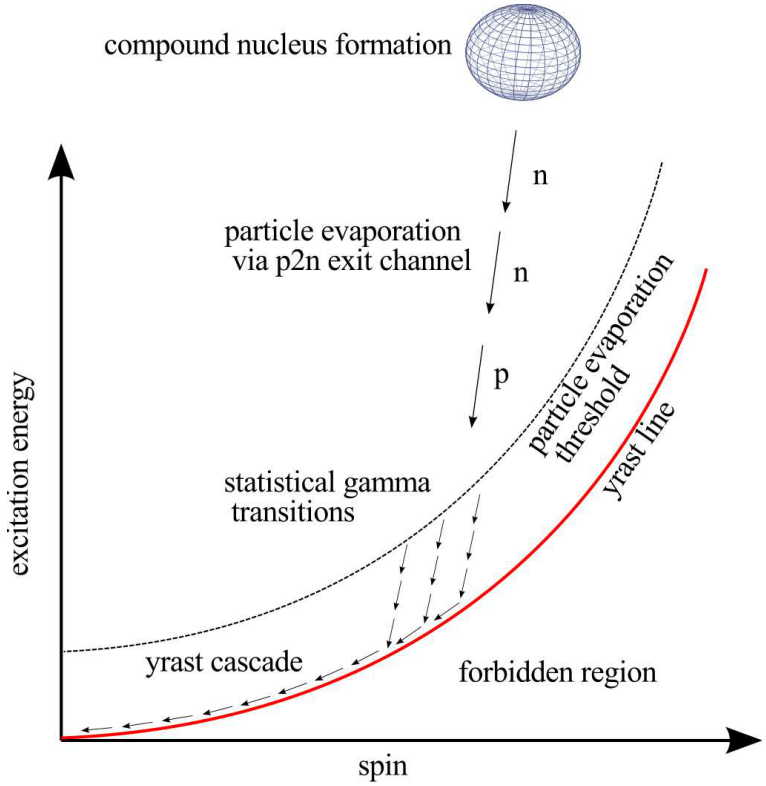

FIGURE 3.1.3: De-excitation of a compound nucleus via the p2n exit channel. Energy is carried away from the nucleus by particle emission until the evaporation residue is within the particle evaporation threshold. The nucleus then continues to de-excite towards the yrast line via statistical γ rays before finally de-exciting further via a cascade of γ-ray transitions between states close to the yrast line.

lower excitation energy for that value of spin. Thus the de-exciting compound nucleus will continue to emit γ rays - following the yrast line as it loses energy - until the ground state is reached.

3.2 JUROGAM

The JUROGAM detector array consists of 43 EUROGAM phase I and GASP-type [35] Compton-suppressed high-purity germanium (HPGe) detectors distributed in six rings with each ring at an angle relative to the beam direction as given in Table 3.1.

Compton suppression is a technique that allows for the removal of Compton-

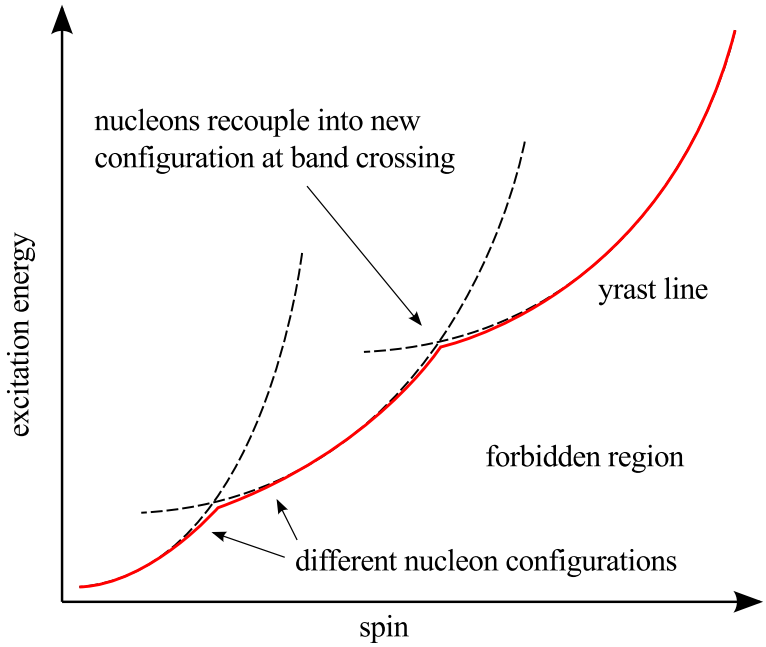

FIGURE 3.1.4: A plot of excitation energy against spin showing the greatest angular momentum obtainable for a given energy; known as the yrast line (red).

scattered γ-rays from the HPGe detector output signal. As the high-resolution solid state germanium detectors are of finite size, many γ rays will Compton-scatter out of the detector before they have deposited all of their energy, thus only a fraction of the energy of the incident γ radiation is detected. By surrounding the main HPGe detector with a larger low-resolution suppression detector (usually a bismuth germanate (BGO) scintillator) and running the pair in anticoincidence, a scattered γ ray that is detected by both detectors can be safely ignored. The larger suppression detector has a greater stopping power than the main detector and thus it is highly unlikely that a γ ray will scatter out of both devices.

Figure 3.2.1 shows the JUROGAM detector array at the University of Jyväskylä Accelerator Laboratory. Figure 3.2.2 shows the target position of the detector with the beam line coming in from the left. The first vertically focusing quadrupole magnet of the RITU gas-filled separator can be seen downsteam of the target position on the right-hand side.

TABLE 3.1: The ring number, angle from the beam axis, array positions and the maximum number of detector positions per ring, for each ring in the JUROGAM spectrometer.

Ring number	Ring angle θ	Array positions	(Maximum) number of detectors
1	157.60	1 - 5	5
2	133.57	6 - 15	10
3	107.94	16 - 25	10
4	94.16	26 - 30	5
5	85.84	31 - 35	5
6	72.05	36 - 45	10

3.3 Recoil ion transportation unit (RITU)

Typically, the collision of a heavy-ion beam with a thin foil target produces a multitude of reaction products including those from fusion-induced fission, deep-inelastic-type reactions and often up to a dozen fusion exit channels. The role of any recoil separator type device is then to separate and collect the recoiling fusion products from the unwanted contaminants and the much more intense flux of beam particles. Such devices typically achieve this by some configuration of electric and magnetic fields [36], which allows for the primary beam to be dumped and for the ions to be separated by their mass over charge state. RITU however, as a gas-filled recoil separator, operates on the principle of *charge state focusing*.

RITU uses an ion optical configuration of $Q_\nu D Q_h Q_\nu$ where quadrupole magnets are denoted by Q and dipole magnets by D. Vertical and horizontal focussing is denoted by the subscripts ν and h respectively. The first Q_ν magnet collects and focuses the beam from the target position, ensuring that the recoil cone matches acceptance of the dipole magnet. This second magnet then separates the recoils from the beam before dumping the beam in a beam stop located inside the dipole magnet chamber. The Q_h and Q_ν quadrupole magnets then provide final focusing of the fusion products before implantation into the DSSD of the GREAT spectrometer.

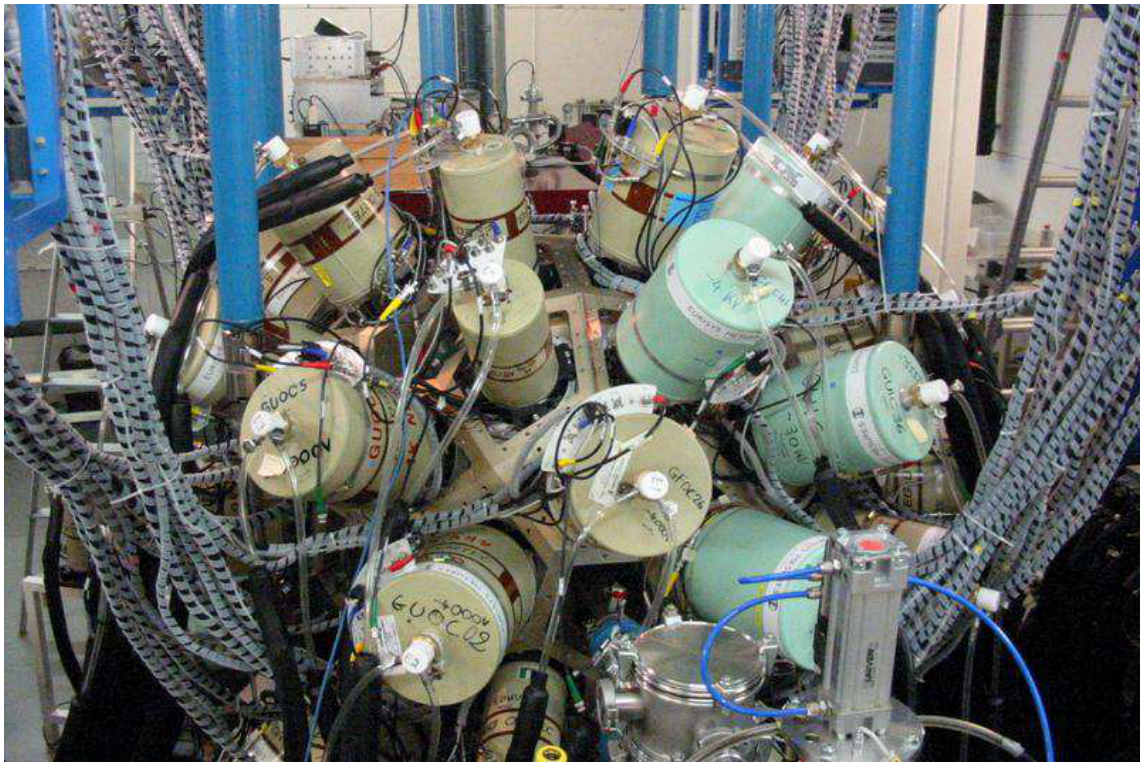

FIGURE 3.2.1: The JUROGAM γ-ray spectrometer array at the University of Jyväskylä.

Most gas-filled separators utilise a *DQQ* configuration; it is the addition of the front Q_ν magnet which makes it possible to place an efficient γ-ray detector, such as JUROGAM, around the target position without losing angular acceptance.

The separator vacuum chamber is filled with helium gas from the target region to the GREAT spectrometer at the focal plane. A 0.5 mg/cm^2 Ni foil separates the high vacuum of the beam line from the low pressure helium gas and a thin Mylar[2] window separates the RITU separator chamber from the methylpropane used in the MWPC of the GREAT spectrometer.

High transmission efficiency is achieved as a result of filling the field region with the dilute helium gas; collisions between reaction products and the gas atoms lead to a charge state focusing effect where the ions follow a trajectory approximately

[2]Mylar, developed in the mid-1950s, is a trade name for biaxially-orientated polyethylene terephthalate (BoPET), which is a polyester film used for its high tensile strength, dimensional and chemical stability, transparency, electrical insulation and gas barrier properties.

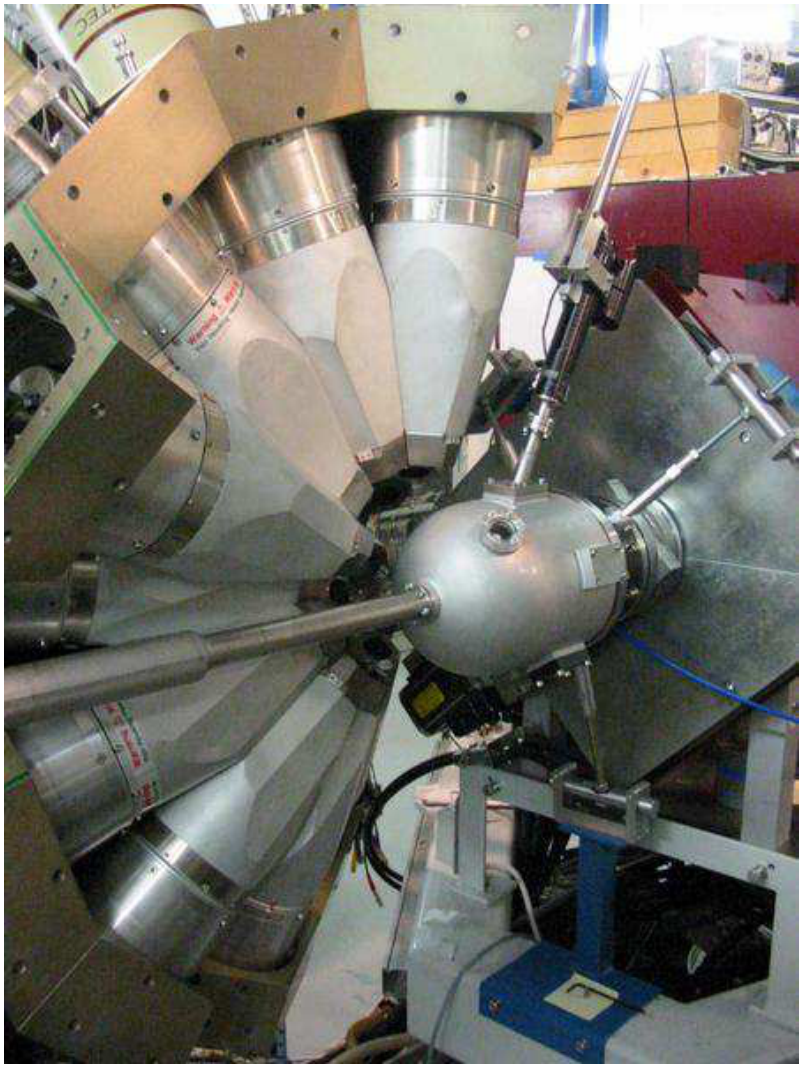

FIGURE 3.2.2: The target position of the JUROGAM detector array and the first quadrupole magnet Q_ν of RITU. The beam pipe can be seen entering the array from the left.

determined by their average charge state in the gas and independent of their original charge state at the exit of the target position. As a result, velocity and charge acceptance may both approach 100% and transmission is mainly limited only by angular acceptance and losses inside the separator due to scattering [30]. Figure 3.3.1 shows the JUROGAM detector array just visible at the target position in the top left corner followed downbeam by the $Q_\nu D Q_h Q_\nu$ magnet configuration. At the focal plane of RITU in the bottom left hand corner is the GREAT spectrometer.

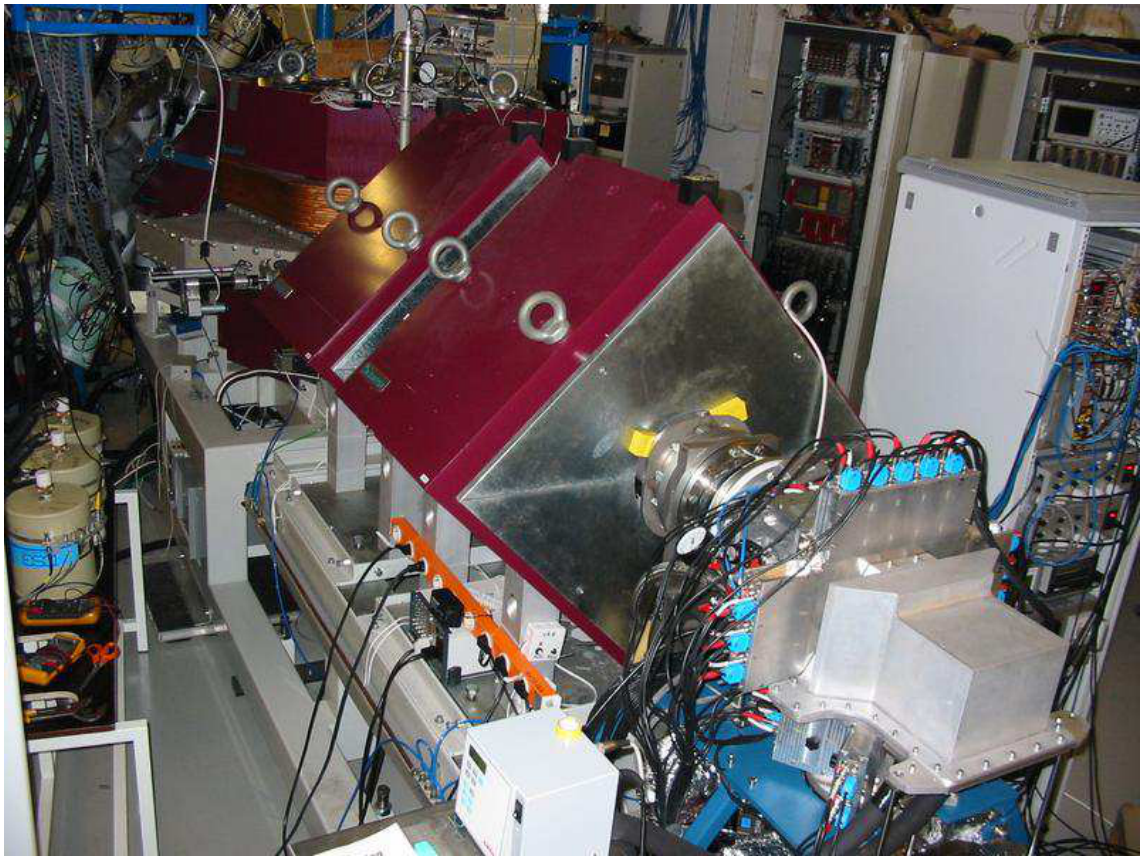

FIGURE 3.3.1: RITU and the GREAT spectrometer with the JUROGAM detector array just visible at the top left.

Figure 3.3.2 shows the $Q_\nu DQ_h Q_\nu$ magnet configuration of the RITU separator with the beam incident at the target position on the left hand side. The beam stop region inside the dipole magnet chamber is indicated by the red line.

3.4 Gamma recoil electron alpha tagging (GREAT) spectrometer

Situated at the focal plane of RITU - see Figure 3.0.1 - the Gamma Recoil Electron Alpha Tagging (GREAT) spectrometer [27] is a composite detector array consisting of two Double-sided Silicon Strip Detectors (DSSDs), a MultiWire Proportional Gas-Counter (MWPC), a planar High Purity Germanium (HPGe) detector and an array

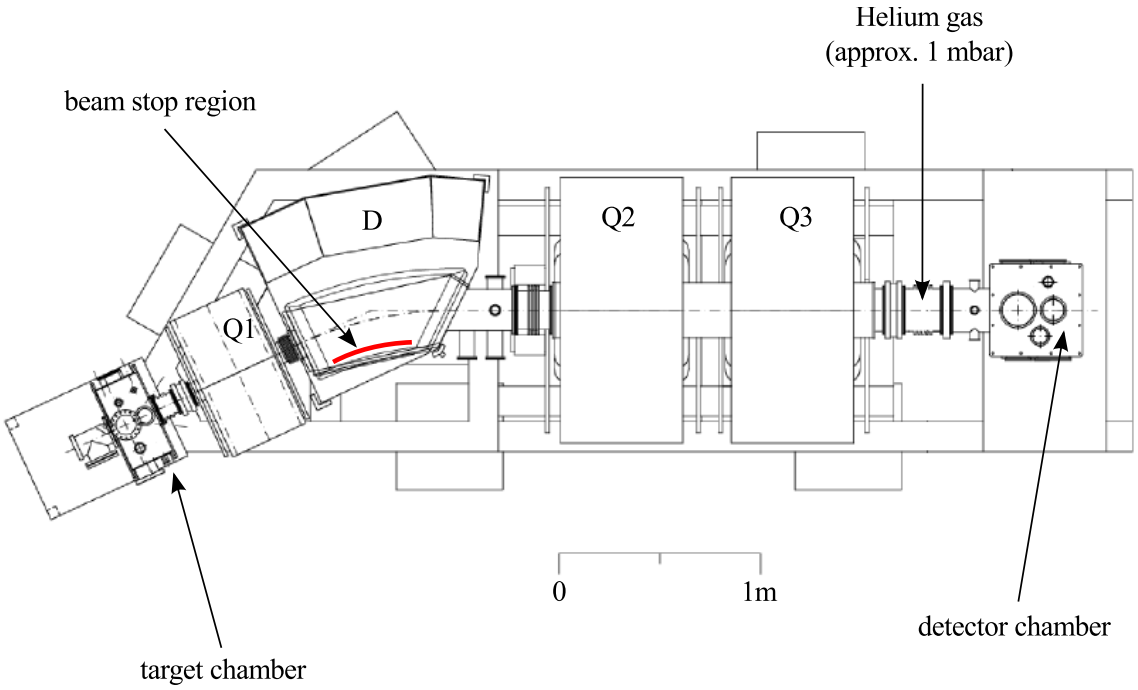

FIGURE 3.3.2: Top-down view of the RITU gas-filled separator showing the $Q_\nu DQ_h Q_\nu$ ion optical magnetic configuration and beam stop region (indicated by the red line).

of 28 Si PIN diode detectors. The arrangement of these detector systems is shown in Figure 3.4.1. To detect high energy γ rays, a high-efficiency segmented clover-type HPGe detector is situated directly above the GREAT spectrometer.

3.4.1 Multi-wire proportional counter (MWPC)

The multi-wire proportional counter (MWPC) is a type of gaseous ionization detector used to count particles of ionizing radiation. As it can measure the energy of incident radiation, MWPCs are widely used where it is necessary to distinguish between different radiation types, for example α and β particles. Practically, a MWPC consists of a collection of thin, parallel and equally spaced wires, sandwiched symmetrically between two cathode planes.

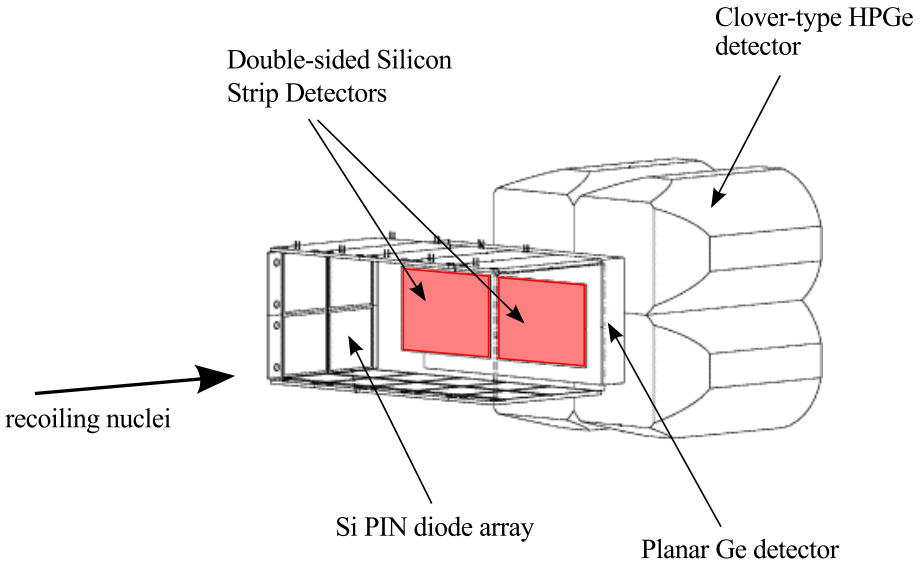

FIGURE 3.4.1: Schematic drawing of the GREAT spectrometer showing the arrangement of the silicon and germanium detectors. The DSSDs are then highlighted in red. Recoiling nuclei would pass through the MWPC (not shown) and the enter the detector system from the left. Original image courtesy of Ref. [27].

The anode wires are grounded and as a negative potential is applied to the cathode an electric field is established. This field is then approximately uniform between the electrodes, except for the region near the wires where it becomes distorted. As a charged particle passes through the gas volume, charges are liberated in ionisation events and the particle will leave behind it a trail of electron-ion pairs. Electrons will then drift to the nearest wire causing a voltage pulse to be recorded.

3.4.2 Double-sided silicon strip detectors (DSSDs)

The DSSDs are used to measure the energy, time and position of implanted ions and of their subsequent radioactive decay products (protons, alpha and beta particles). A DSSD consists of two 60 × 40 mm^2 active windows with 200 individual strips at a pitch of 1 mm in both directions, giving a total of 4800 independent pixels. Approximately 80% of the distribution of fusion products in the focal plane is then covered by the active area of the DSSD. The array of Si PIN diode detectors then

surrounds the perimeter of the two DSSD windows in order to measure the energy of conversion electrons emitted during the decay of implanted ions.

3.4.3 Silicon PIN diode array

Situated between the DSSDs and MWPC is an array of 28 PIN diode silicon detectors, as shown in Figure 3.4.1. A PIN diode is a (photo)diode with a wide, lightly doped near intrinsic region placed between the (typically heavily doped) p-type and n-type semiconductor regions. The utilisation of such a near intrinsic region makes a PIN-type diode more suitable for photodetection applications. Each diode has a thickness of 500 μm and an active area of 28×28 mm^2. Although their primary function is the detection of conversion electrons and β decays, the array can also be used to reconstruct energy information of α particles which escape the DSSDs.

An α particle emitted from the DSSDs towards the PIN diode array in the upbeam direction will deposit its energy shared between the DSSDs and the array. Thus the full energy of the α decay can be reconstructed, although the accuracy of this technique is limited by energy losses in the two detectors. This *add-back* technique is a powerful method of increasing statistics, as typically 40% of events will escape the DSSDs.

3.4.4 Planar Germanium (HPGe) strip detector

The role of the planar double-sided germanium strip detector is to measure the energies of X-rays and low energy γ transitions; providing positional information that can be correlated with data from the other GREAT detectors. The detector is mounted approximately 10 mm downbeam of the DSSDs and is housed in its own cryostat with a thin beryllium[3] entrance window. To minimise attenuation of low-

[3]Because of its low density and atomic mass, beryllium is relatively transparent to X-rays and other forms of ionising radiation; thus making it particularly suitable as a window material.

energy photons the detector is mounted inside GREAT vacuum chamber. Like that of the DSSDs, the detector has an active area of 60×120 mm^2.

As high-energy γ rays will pass through the detector, to be absorbed by the surrounding clover detectors, the planar detector's (relatively) low thickness of 15 mm gives a maximum efficiency at < 100 keV. To allow for spatial correlations to be made with the DSSDs, a strip pitch of 5 mm in both x and y directions gives a total of 288 pixels. Like the four clover detectors, the planar detector utilises the $\backsim$ 0.5 μs time-of-flight from JUROGAM to implantation in the DSSDs to look for isomer-delayed transitions.

3.4.5 Clover detectors

Clover-type silicon detectors are so called because each detector consists of a segmented assembly of four co-axial n-type HPGe crystals resembling the shape of a four-leaf clover. Four clover detectors (totalling 16 crystals) are situated left, right, above and downbeam of the focal plane. Housed outside of the vacuum chamber, as shown in Figure 3.4.1, the clover-type detectors can be used for the detection of high-energy γ rays emitted from isomeric states.

3.5 Total data readout (TDR)

Prior to around 2002, RDT experiments often suffered from a common deadtime due to the use of hardware-based data-acquisition systems. In this setup, a typical trigger condition might be that any focal plane detector fires (e.g. detection of an implanted recoil). This would occur some microseconds after correlated γ radiation had been emitted at the target position (due to the time-of-flight through the separator) and a *delayed coincidence* mode is then used in the analogue-to-digital converters (ADCs) instrumenting the target array to overcome this flight delay. By collecting

signals from detectors only for a fixed period of time after a trigger condition has passed, a system-wide deadtime is introduced in which further events of interest may be missed. For low triggering rates, this is not an inadequate method of data acquisition.

However, for high triggering rates or when events of interest are frequent compared to background counts, such conventional data acquisition systems are no longer sufficient. The total data readout (RDT) technique [28] circumvents these severe deadtime losses by reading from all detectors individually and simultaneously without the requirement for a triggering condition to have been passed. Each signal is then time stamped to a precision of 10 ns by a 100 MHz clock which is distributed and synchronised throughout the system. Spatial and temporal correlations made with a software trigger are then used to build events offline in a software-based event builder (events can also be built using online data for monitoring purposes).

One essential advantage of the RDT technique, in which the γ-ray data of interest precedes the triggering condition(s) by several milliseconds, is that correlations can be made over relatively long periods of time without missing other events of interest that may have occurred during this time. A second considerable advantage is that data correlated to a triggering event can be collected prior to the event without difficulty.

Of course, collecting the total data output from an experiment - much of which is of little or no interest - would demand a vast storage capacity. Therefore a pre-filter is employed to limit the amount of data which is stored. Such a pre-filter might be the requirement that all stored data must be correlated with an event in the DSSDs. Thus, in the offline analysis, all correlations made when sorting the data must be made relative to events which occur in the DSSDs (e.g. a recoil followed by an α decay).

Chapter 4

Experimental Methodology

4.1 Recoil decay tagging (RDT) technique

Typically, in fusion-evaporation reactions, γ rays from the heavy neutron-deficient nuclei under investigation (which often exhibit low production cross-sections) have to be isolated from the high fission γ-ray backgrounds and γ rays produced in the de-excitation of the target material and other, more highly populated, evaporation channels. The *recoil decay tagging* technique [2] allows for γ-ray data collected by JUROGAM and GREAT to be correlated with a specific reaction channel by utilising spatial and temporal correlations with an implanted recoil and subsequent decay events.

Signals in the DSSDs are processed to distinguish between recoil and subsequent decay events, and decays are correlated with a previous event in the same DSSD pixel. If the decay is preceded by a recoil, the energy and decay time characteristics of the recoil-decay events are checked to determine whether they match those of the nucleus of interest. If these conditions are passed, correlated γ rays from other detectors are assigned to that particular nucleus.

For this technique to be successful, recoil and decay events must be distinguished

experimentally. Recoil events are transported to the DSSDs via the RITU gas-filled separator, and therefore must pass through the MWPC before becoming implanted in a DSSD pixel. As this is not the case for decay events, which will originate from this same pixel, they will not be accompanied by an MWPC signal. Whilst this allows for decays to be distinguished from recoil events, unreacted beam fragments - which have eluded the separation process - will also carry an accompanying MWPC signal before becoming implanted in the DSSDs. Differences in the liberated charge and the MWPC-to-DSSD flight time are considered so as to ensure that these fragments are identified and discarded.

The velocity of the unreacted beam fragments is typically greater than that of the recoiling compound nuclei, thus the time-of-flight (TOF) between the MWPC and DSSD is smaller. Furthermore, recoils will typically carry a greater charge than the beam fragments and therefore cause more ionisation in the MWPC, depositing a larger amount of energy. These differences allow for beam fragments to be isolated from evaporation residues, as shown in Figure 4.1.1. A 2-dimensional gating condition is used to ensure that, for an event to be defined as a recoil, its deposited energy and MWPC to DSSD time-of-flight must be within certain limits.

In order for DSSD events to be processed, they must be stored in a software *tagger*. A tagger is a 3-dimensional array in which two dimensions correspond to the coordinates of the DSSD pixel in which the event became implanted, and a third corresponds to the time-frame in which events occur. Each element in the array then corresponds to a pixel of a DSSD, and when an event occurs in a given pixel, it is stored in that corresponding element until a prespecified time interval[1] has passed. Further events which occur in that pixel are then added to the tagger, in addition to those already stored. When an event is identified as a decay, the previous

[1] A typical time interval, or *tagger length*, might be five times the alpha-decay half-life of the nucleus of interest. For example, when investigating ^{165}Re $\left(t_{1/2} = 1740 \text{ ms}\right)$, a tagger length of 10 s is used.

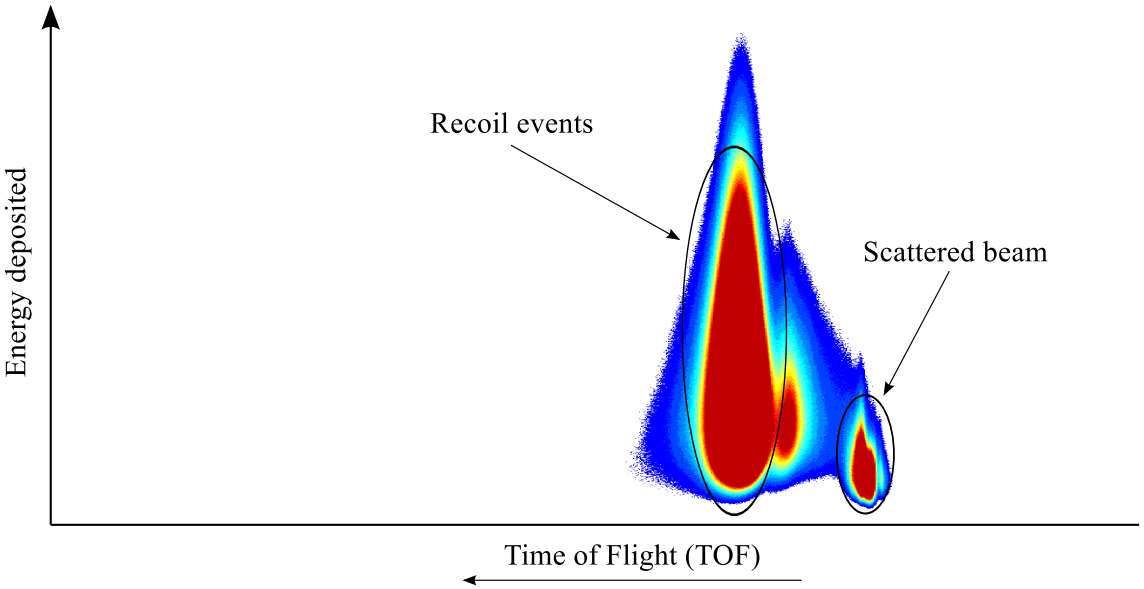

FIGURE 4.1.1: Energy deposited in the MWPC against the MWPC to DSSD flight time. The scattered beam can be isolated from the recoiling evaporation residues by considering differences in the time of flight and the amount of energy deposited.

events in that pixel are then available for correlation, as discussed above. All signals are timestamped with a precision of 10 ns, making these temporal correlations straightforward to perform.

4.2 Gamma-ray correlations: a practical application of the RDT technique

In order for γ rays detected in the JUROGAM array and focal plane detectors to be correlated with the implantation and subsequent decay of a nucleus of interest, a number of considerations must be taken into account. Establishing such correlations is a superb example of a practical application of the RDT technique, and also serves to demonstrate the power of software event building using triggerless TDR systems.

The periodicity of the K130 cyclotron [37] is shorter than the flight time through the RITU gas-filled separator, $\backsim$ 70 ns and $\backsim$ 0.5 μs, respectively, and as a result

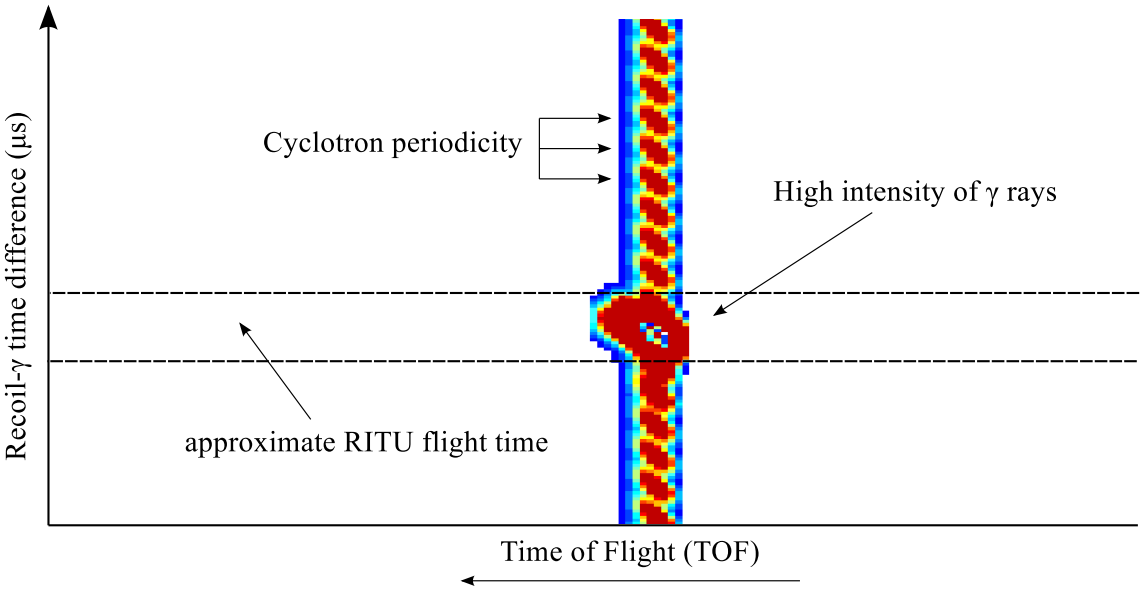

FIGURE 4.2.1: Recoil-γ time difference against the time of flight between the MWPC and the DSSDs. A high density (red) of γ rays collects at the average recoil-γ time difference corresponding to the RITU flight time. The smaller periodic regions of high intensity correspond to the resonant frequency of the cyclotron; there is a greater probability of a reaction and thus the detection of the largest number of γ rays.

many fusion reactions occur at the target position in the time it takes a recoil to reach the focal plane, thus introducing a large γ-ray background. By taking into account the average RITU time-of-flight and ignoring any data which deviate from this range, γ rays detected at the target position can be correlated with recoil events in the DSSDs. This technique is demonstrated in Figure 4.2.1.

Recoils can also be correlated with transitions detected in the focal plane planar and clover-type detectors of the GREAT spectrometer array. As the DSSDs are also located at the focal plane, the average flight time does not need to be taken into account, and instead only the decay time is considered. As a result, γ rays detected at the focal plane are collected only if they occur within a specified time gate of an event in a DSSD pixel.

There are three major limitations to recoil decay tagging; the successful application of the technique is dependent on the α-decay half-life and branching ratio of the

nucleus of interest, along with the recoil implantation rate. Nuclei with half-lives shorter than the average RITU time-of-flight, i.e. less than $\backsim 0.5$ μs, will often decay before reaching the focal plane spectrometer, thus preventing the nucleus from being identified via its characteristic α decay. Furthermore, for nuclei with longer half-lives - i.e. more than $\backsim 0.1$ s - identification becomes problematic when the recoil rate at the focal plane is significantly high. This combination of long decay time and high implantation rate results in an increased likelihood for misscorrelations to be made. Finally, the applicability of the RDT technique is limited for nuclei which exhibit low α-decay branching ratios.

At high recoil implantation rates, γ rays can be miscorrelated with random implantations during the data analysis. This occurs when an unrelated recoil is implanted into a DSSD pixel after a recoil of interest, but before that recoil has decayed. Tagging on the decay of the recoil of interest thus causes it to be miscorrelated with the unrelated recoil, introducing contamination.

However, for nuclei which exhibit suitable α-decay characteristics, the RDT technique allows for spectroscopic studies to be performed where relatively low production cross-sections and large γ-ray backgrounds would otherwise prevent transitions from being assigned to the nuclei of interest.

4.3 Doppler-shift correction

The reaction products formed during heavy-ion fusion evaporation reactions are not produced at rest. Consequently, the energy of any γ radiation emitted by a particle with such a non-zero velocity will be Doppler shifted according to

$$E = E_0 \left(1 + \frac{v_{recoil}}{c} \cos\theta\right) \tag{4.3.1}$$

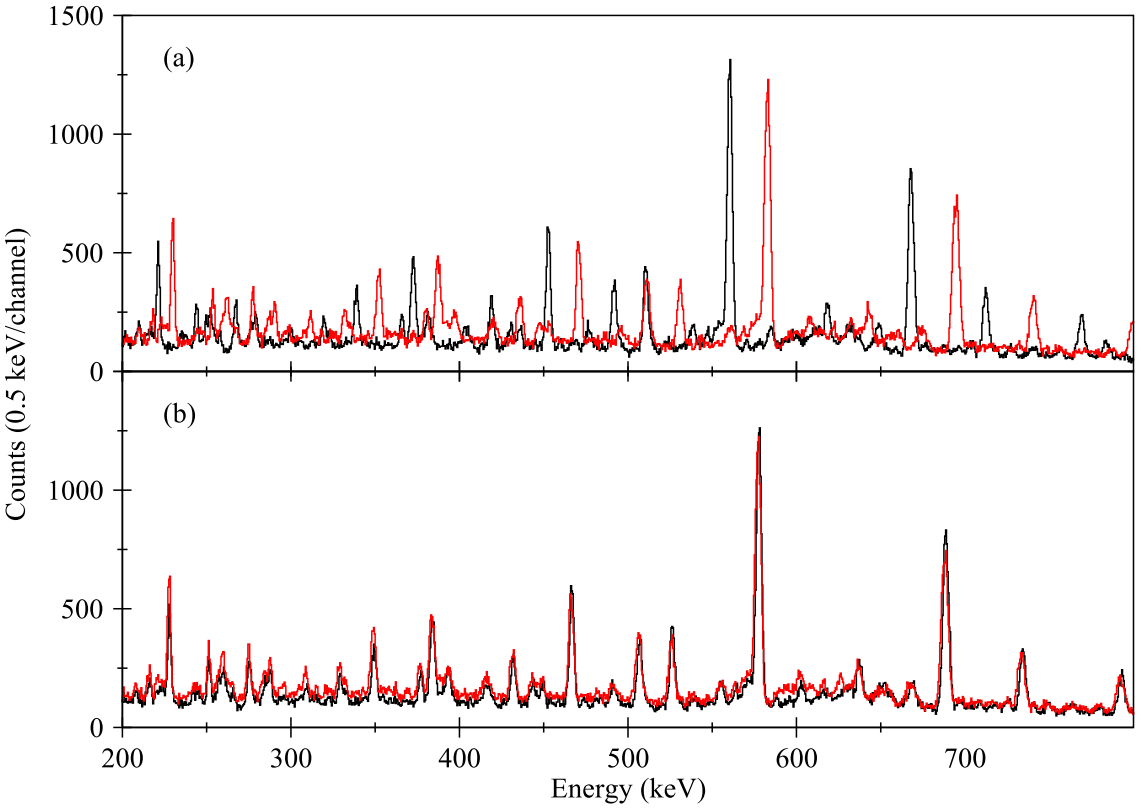

FIGURE 4.3.1: An RDT spectrum produced by gating on the $^{163}Re^{m}$ α decay. Rings 1 and 6 are at angles of 157.60° and 72.05° from the beam axis, respectively. (a) Before a Doppler correction is applied, energies recorded in Ring 1 are redshifted whilst those in Ring 6 are blueshifted. Notice the greater energy shift in Ring 1, caused by this ring being positioned further from the 90°position than Ring 6. (b) The true energy of the transitions after the application of a Doppler correction of $\beta = 0.0317$.

$$\frac{E - E_0}{E_0} = \beta \cos\theta \qquad\qquad \beta = \frac{v_{recoil}}{c} \tag{4.3.2}$$

where E and E_0 are the observed and true γ-ray energies, respectively, v_{recoil} is the recoil velocity of the compound nucleus and θ is the angle of the emitted γ ray with respect to the beam direction. Table 3.1 gives the angle from the beam axis for each ring in the JUROGAM spectrometer array. The effect of the Doppler shift on rings 1 and 6 at angles 157.60°and 72.05°, respectively, is shown in Figure 4.3.1. The corrected spectrum (b) is shown for comparison.

The true γ-ray energy E_0 is the energy that would be recorded in a detector at 90° to the target position. Since there is no detector positioned at this angle, the midpoint between the energies recorded in rings 4 and 5, located at 91.16°and 85.84°, respectively, is taken as the true energy. This is a valid technique, as the energy recorded in each ring is Doppler shifted by an equal but opposite amount; thus, by taking the midpoint energy the shifting effect is cancelled out. The Doppler shift correction parameter β is then determined from the straight-line gradient of the observed energy E for a given transition as a function of $\cos\theta$.

4.4 Analysis of coincidence γ rays using RADWARE

4.4.1 The RADWARE software package

The analysis of $\gamma\gamma$ coincidence matrices has been performed using the RADWARE ESCL8R software package [32]. ESCL8R allows a matrix to be inspected by setting gates, i.e. by specifying a particular prompt γ-ray energy, or gate, and producing a gated spectra of the intensity of coincident γ rays as a function of energy.

The coincidence data set is stored as a 2k×2k-channel matrix[2] - or two-dimensional histogram of energy vs. energy - and is symmetrised such that the two energy axes are equivalent. To fully exploit the high sensitivity of the state-of-the-art detector arrays used in this experiment, it is crucial that the background level is properly understood and well-estimated. As the analysis in the present work uses discrete photopeak - or *full-energy* - coincidence measurements, it is necessary to establish the degree of Compton scattering in the data set.

In addition, in order to perform the analysis of a given $\gamma\gamma$ coincidence matrix,

[2]The data set is initially sorted into a 4k×4k-channel matrix and then compressed to a 2k×2k-channel matrix.

ESCL8R also requires knowledge of the efficiency and energy calibrations as well as peak shapes and widths as a function of γ-ray energy. A two-dimensional background subtraction algorithm is used to account for the Compton-scattered γ rays and quasicontinuum transitions. The background is subtracted from each gate individually, rather than using a matrix with the background already removed; this allows the programme to keep track of the individual uncertainties on the counts-per-channel in the gated spectrum.

The gate width is set as the FWHM of the corresponding energy peak, which greatly simplifies the analysis of the coincidence matrix. The FWHM, in units of channels, is given by 4.4.1, where x is the channel number.

$$\text{FWHM}(x) = f + g\sqrt{\frac{x}{1000}} + h\frac{x}{1000} \tag{4.4.1}$$

The f term arises from noise in the detector and amplification circuits, and the second term from the statistics of the charge collection process. The third (linear) term is due to the emission of γ rays from recoiling residual nuclei causing a Doppler broadening of the peaks. By using a thick target, it is possible to prevent these recoils, in which case the last term can be set to zero. The values of f, g and h and can be set within ESCL8R, or fitted by least squares regression to a selected gated spectrum, to allow for the best agreement between the level scheme predictions and the observed data.

In the analysis of the excited states, ESCL8R displays a proposed level scheme which is continually modified as the analysis progresses. This level scheme is then used to calculate expected coincidence energies and intensities for comparison with the observed experimental data. The user can add bands and levels to the scheme using the graphical user interface (GUI). ESCL8R will propose a corresponding spin-parity and energy for each level, which the user can then edit as the scheme is

developed.

ESCL8R makes it simple for the user to take and view gates on the matrix. As a gate only specifies the mean energy, the energy width must also be considered; by default this is taken as the FWHM, as given by 4.4.1. The user may also gate on two energies simultaneously, to produce a spectrum of the γ rays which are in coincidence with both transitions; this tool is particularly useful in the analysis process. When a gate is selected, all transitions with energies that lie within the gate limits are highlighted in the level scheme window. ESCL8R then displays the observed and calculated spectra, the difference spectrum and the residual spectrum[3]. This then allows the user to easily locate areas where the proposed level scheme fails to reproduce the observed data and make appropriate modifications.

4.4.2 Building the excited states level scheme

A level scheme is an ordered decay scheme of the excited states of the nucleus under investigation, and is constructed from the mutually coincident γ rays emitted as the nucleus loses energy. There may be several decay paths leading to or from a single state and, in principle, the intensity flow into a given state will be equal to the flow out of that state. An exception to the latter is the ground state or any isomeric state that may decay outside of the coincidence time-frame.

The specific order of transitions within a given decay path is deduced from their intensities. When more than one possible decay path exists, consistency requirements of the excitation energies are used to offer greater insight. Two γ rays both feeding or de-exciting the same state will not be in coincidence, and any two coincident γ rays must be located somewhere in the same decay path.

Figure 4.4.1 is a simple $\gamma\gamma$ symmetrised coincidence matrix which serves to

[3]The *residual spectrum* is given by dividing the difference spectrum by the experimental uncertainty.

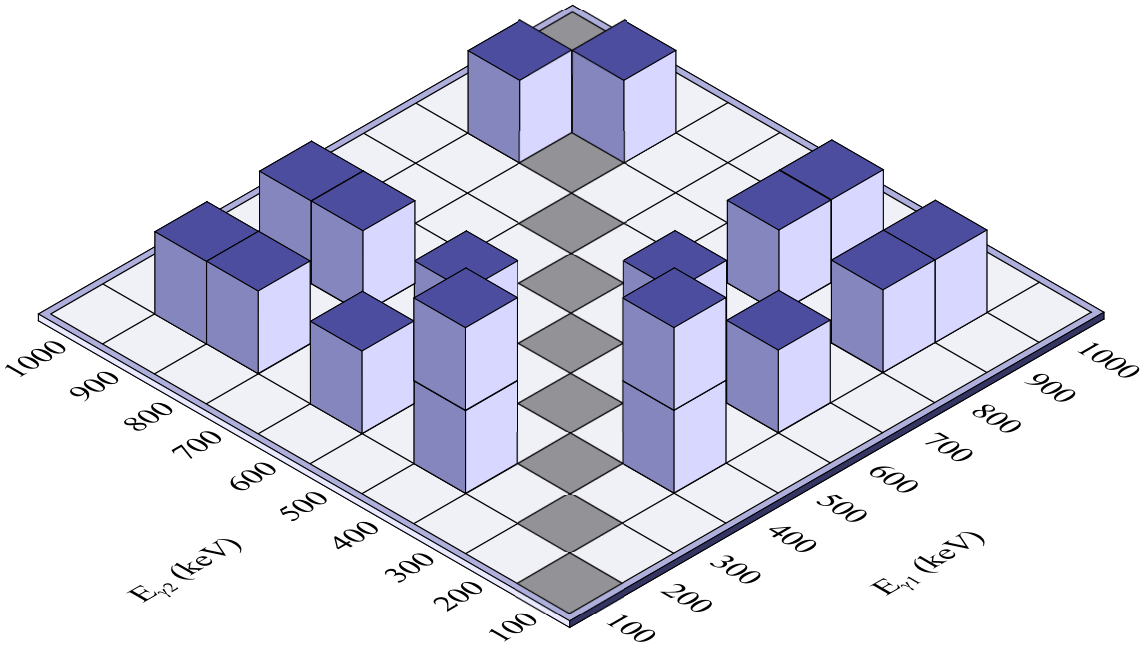

FIGURE 4.4.1: A simple $\gamma\gamma$ symmetrised coincidence matrix to demonstrate the analytical technique.

demonstrate the analytical technique used in this work. Figure 4.4.2 then shows the gates taken on every value of $E_{\gamma 2}$ for which there are coincident γ rays, and the energy $E_{\gamma 1}$ projected onto the horizontal axis.

Firstly, note that (a) the 600 keV transition is not present in the 900 or 800 keV gates and that the 900 and 800 keV transitions are not present in the 600 keV gate; also that (b) the 800 keV transition is present in the 900 keV gate and vice versa. Secondly, note that (c) the 600, 800 and 900 keV transitions are all present in both the 200 and the 400 keV gates.

From (a) and (b), one can deduce that the 900 and the 800 keV and the 600 keV transitions occur in two separate decay paths, or events. From (c), one can then further infer that these two decay paths must converge before reaching the ground state. This is shown in Figure 4.4.3, which is the completed level scheme corresponding to the matrix.

Where two transitions have a similar energy - within perhaps 1 - 2 keV - their

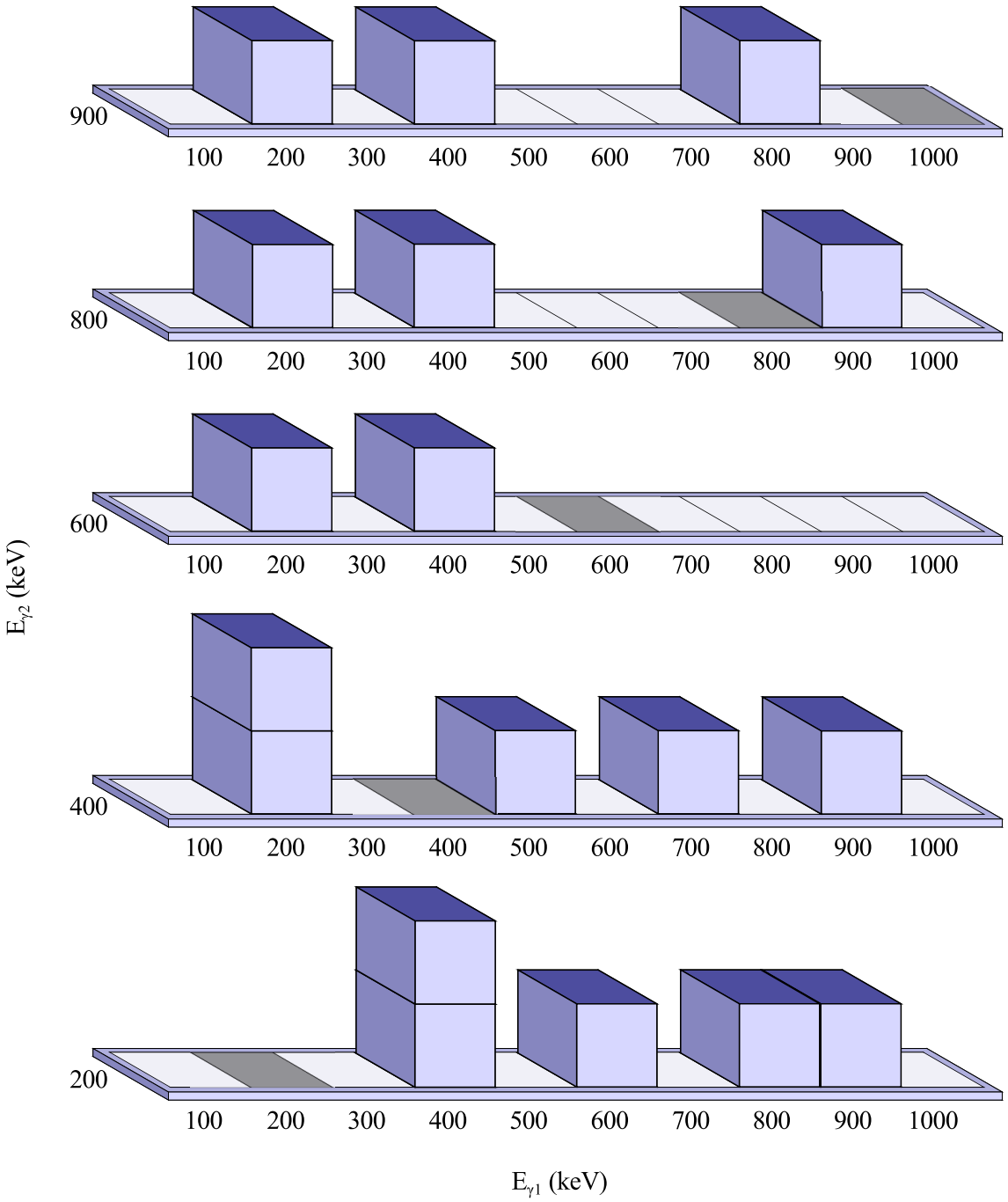

FIGURE 4.4.2: Gates taken on every value of $E_{\gamma 2}$ for which there are coincident γ rays, with the energy $E_{\gamma 1}$ projected onto the horizontal axis.

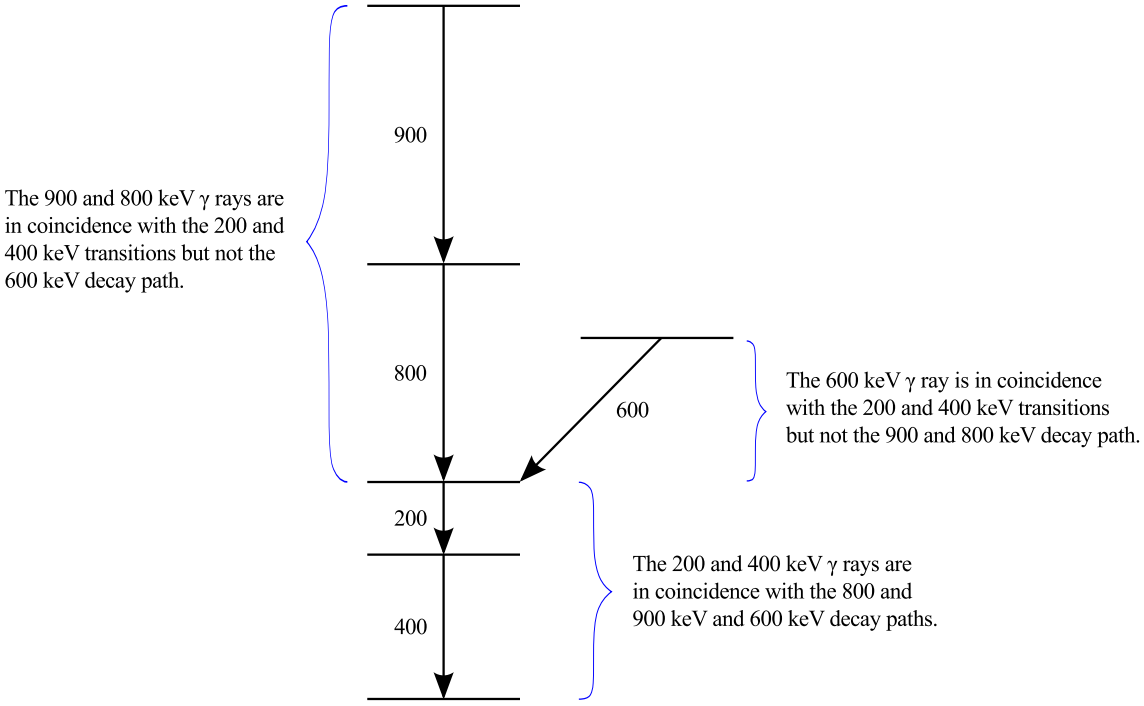

FIGURE 4.4.3: Completed level scheme corresponding to the simple $\gamma\gamma$ symmetrised coincidence matrix shown in Figure 4.4.1.

spectral peaks will overlap and the two γ rays are said to form a doublet. If these two transitions are then in coincidence, the doublet is said to be self-coincident. Both doublets and self-coincident doublets often complicate the process of building an excited states level scheme, as well as reducing the effectiveness of some analytical techniques such as reduced transition probability ratios and angular correlations.

Chapter 5

Collective Excitations in ^{163}Re$_{88}$ and ^{165}Re$_{90}$

The development of coherent behaviour in atomic nuclei generated by the interactions between their constituent nucleons is an issue of central importance in nuclear physics [38, 39]. The evolution of collectivity in nuclei as a function of nucleon number is reflected in the spectrum of low-lying excited states, which vary according to the available valence space. The largest range of nuclei where excited states can be identified with contemporary experimental techniques spans the $82 \leq N \leq 126$ neutron shell. The spectroscopy of excited states at the extremes of this shell is challenging, yet has been achieved through the application of selective experimental techniques. For example, excited states have been identified in many of the Re isotopes from ^{159}Re ($N = 84$) [40] to ^{196}Re ($N = 121$) [41].

The neutron-deficient nuclei near both the $N = 82$ shell gap and the proton drip line are usually synthesised with low production cross-sections. In many cases, the ordering of excited states can only be unravelled through the analysis of recoil-decay correlated γ-ray coincidence data [2]. Proton radioactivity studies have revealed that the ground states of the near-spherical Re isotopes are based on the low-Ω $s_{1/2}$ or

$d_{3/2}$ proton states with a low-lying isomer formed by exciting the odd proton into the high-Ω $h_{11/2}$ state [40, 42, 43, 44]. Recoil-decay correlations with the characteristic proton emissions of ^{160}Re ($N = 85$) [45, 46] and ^{161}Re ($N = 86$) [5] have revealed excited states based on the ground state and an isomeric configuration. These arise from coupling the odd proton to the few valence neutrons in the $f_{7/2}$, $h_{9/2}$ and $i_{13/2}$ states. As the proton and neutron occupancy of the valence space increases approaching the neutron and proton midshells at $N = 104$ and $Z = 66$, a concomitant increase of the deformation is expected, which will influence the relative positions of orbitals at the Fermi surface and the excitation energies of their associated configurations.

With the addition of only a few neutrons, collective excitations are well established in ^{167}Re ($N = 92$) [3]. The level scheme for ^{167}Re is typical of the heavy $N \sim 90$ odd-Z nuclei, which are soft to triaxial deformation (γ) due to spatial density distributions of the proton and neutron orbitals at the top or bottom of their respective shells [47]. The γ-soft cores in these nuclei are sensitive to the occupation of specific orbital configurations, which can polarize the nucleus towards different shapes. For example, in ^{167}Re the degeneracy of the $h_{11/2}$ signature partners is relieved due to the triaxiality of the γ-soft core, yet restored at higher spins due to the rotational alignment of a pair of $i_{13/2}$ neutrons, which is interpreted as the transition to an axially prolate shape [3].

This chapter discusses the structure of the neutron-deficient nuclei ^{163}Re ($N = 88$) and ^{165}Re ($N = 90$), which occupy a transitional region in which collectivity evolves rapidly over the range of a few neutrons, and the interplay between single-particle and collective behaviour is most pronounced. The new structures identified in ^{163}Re and ^{165}Re are interpreted in terms of quasiparticle configurations within the framework of the cranked shell model with the aid of total Routhian calculations.

Previous work [11] has observed a strongly-coupled yrast structure for ^{163}Re

($N = 88$) up to a spin of 23/2 $\hbar$ as based on the $11/2^-$ isomeric state. This indicated a collective structure akin to the heavier isotopes. Further strongly coupled structures comprising low-energy transitions were also observed to feed the low-spin states of this yrast band. These low-spin yrast states were shown to exhibit a higher degree of signature splitting than in the heavier isotopes, reinforcing the trend of greater signature splitting with increasing neutron deficiency. Prior to the work presented in this thesis, a level scheme for ^{165}Re ($N = 90$) had not been established.

The level schemes presented in this thesis for both ^{163}Re and ^{165}Re are original work. The scope of this work spans the Java script used in the initial data sort to the analysis of the level schemes and the calculation of total Routhians for ^{163}Re.

5.1 Experimental details

Excited states in ^{163}Re and ^{165}Re were populated using the reactions listed in Table 5.1. The beam species were accelerated by the K130 cyclotron at the University of Jyväskylä Accelerator Laboratory. Prompt γ rays were detected at the target position by the JUROGAM γ-ray spectrometer [48], comprising 43 EUROGAM-type escape-suppressed germanium spectrometers [35]. The recoiling fusion-evaporation residues were separated from fission products and scattered beam by the RITU gas-filled recoil separator [29, 30] and deposited into the double-sided silicon strip detectors of the GREAT spectrometer [27] at the separator's focal plane.

All detector signals from the JUROGAM and GREAT spectrometers were passed to the total-data-readout acquisition system [28], where they were time-stamped with a precision of 10 ns. This allowed for the accurate temporal correlation of γ rays (detected at the target position) with recoil implantations and their subsequent radioactive decays (detected at the focal plane). These triggerless data were sorted into $\alpha(^A\text{Re})$-correlated $\gamma\gamma$ matrices using GRAIN [31], and analysed with the

TABLE 5.1: Summary of reactions employed in the present work. The quoted beam energies are the bombarding energies at the front of the target.

Experiment	Beam species	Beam energy (MeV)	Average beam current (pnA)	Target isotope	Thickness (mg/cm^2)	Exit channel	Residual nucleus	Duration of experiment (h)
1	^{60}Ni	270	4	^{106}Cd	1.1	$p2n$	^{163}Re	120
2	^{78}Kr	357	6	^{92}Mo	0.5	$3p2n$	^{165}Re	172
3	^{78}Kr	357	6	^{92}Mo	1.0	$3p2n$	^{165}Re	26

RADWARE [32] software package.

5.2 Results

5.2.1 Excited states in ^{163}Re

In-beam γ-ray spectroscopy of heavy nuclei approaching the proton drip line is challenging for several reasons. Typically, the production cross-sections for very neutron-deficient nuclei are much lower (< 200 μb) than for nuclei populated closer to the line of stability. Furthermore, heavy-ion induced fission is a strong reaction exit channel and produces a large background of γ rays. These obstacles have been mitigated by the application of the recoil-decay tagging technique [2], which employs spatial and temporal correlations to associate γ rays emitted by a specific nucleus at the target position with their subsequent characteristic radioactive decays detected at the focal plane of the recoil separator.

Previous decay spectroscopy experiments [49, 50, 51] have identified α-decay branches from both the $1/2^+$ ground state and a low-lying $11/2^-$ isomer in ^{163}Re. These decay properties, given in Table 5.2, are well-suited for tagging experiments. This is due to a high α-branching ratio and a relatively short half-life, which subsequently results in fewer miscorrelations. However, the overlapping $\alpha(^{163}\text{Re})$ peaks render it difficult to assign γ rays above the $s_{1/2}$ ground state unambiguously, as the fusion evaporation reaction preferentially populates excited yrast states based on the $h_{11/2}$ state.

A total of 1.67×10^6 full-energy (E_α=5920 keV) $\alpha(^{163m}\text{Re})$ decays were detected during the experiment. The production cross-section is estimated to be 150 μb, assuming a RITU separation efficiency of 50% and a 65% full-energy α-particle detection efficiency.

Figure 5.2.1(a) shows γ rays detected at the target position and correlated with

TABLE 5.2: α-decay properties for the $1/2^+$ ground state and $11/2^-$ isomer of ^{163}Re. The level energies are quoted relative to the ground state. Values taken from Ref. [49, 50].

J^π	Level energy (keV)	Decay Energy (keV)	Half-life (ms)	Branching ratio (%)
$1/2^+$	0.0	5870(5)	390(72)	32(3)
$11/2^-$	115(4)	5920(5)	214(5)	66(4)

any recoiling nucleus implanted in the GREAT focal plane spectrometer. Gamma rays from ^{163}Re are swamped by the emissions from nuclei produced in other reaction channels with higher production cross-sections. For example, the prominent γ rays at 288 keV and 433 keV originate from ^{163}Ta [52] populated via the $3p$ exit channel, and the 384 keV, 506 keV and 555 keV transitions belong to ^{163}W [53] produced in the $2pn$ reaction channel. Figure 5.2.1(b) shows a γ-ray spectrum correlated with recoils which are followed by an α decay from the $11/2^-$ isomer in ^{163}Re within the same pixel of the DSSD. This spectrum shows that the γ rays arising from the strongest reaction channels are suppressed, leaving intense γ-ray transitions at 577 keV and 688 keV which are not immediately apparent in the recoil-correlated spectrum. Thus, these transitions are assigned to ^{163}Re. Such deductions serve well to demonstrate the power of the RDT technique.

The excitation level scheme for ^{163}Re was deduced from the analysis of γ-ray coincidences correlated with the distinct α decay of the $11/2^-$ isomer in ^{163}Re. A total of 2.4×10^5 α-correlated $\gamma\gamma$ coincidences were incremented into a $E_{\gamma1} - E_{\gamma2}$ coincidence matrix. The recoil-decay time correlation was limited to 214 ms to avoid false correlations with the dominant reaction channel ^{163}W, which has a longer α-decay half-life $t_{1/2} = 2800(170)$ ms [51]. The level scheme deduced from these data is shown in Figure 5.2.2. Table 5.3 gives the measured gamma-ray energies and intensities, along with the spin assignments of the initial and final states.

Figure 5.2.3 shows γ rays in coincidence with the 577 keV, 688 keV and 466 keV

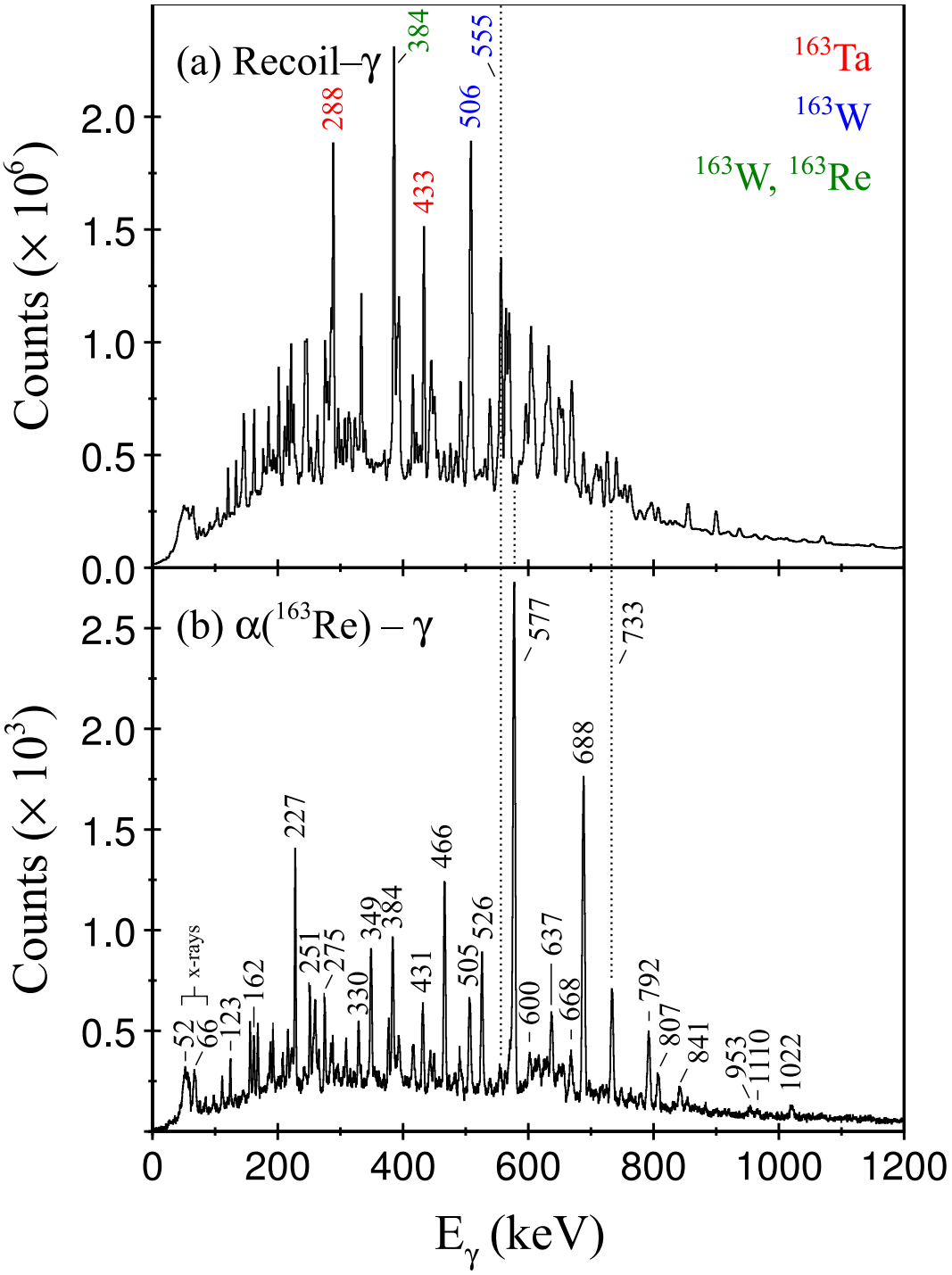

FIGURE 5.2.1: (a) Prompt γ rays detected in the JUROGAM spectrometer and correlated with any recoil implantation detected in the GREAT implantation detector, located at the focal plane of the RITU separator. Note that both ^{163}W and ^{163}Re have associated 384 keV transitions. (b) Gamma rays correlated with recoil implantations followed by the characteristic α decay from the $11/2^-$ isomer in ^{163}Re within the same DSSD pixel of the GREAT spectrometer. The recoil-α correlation time was limited to 214 ms.

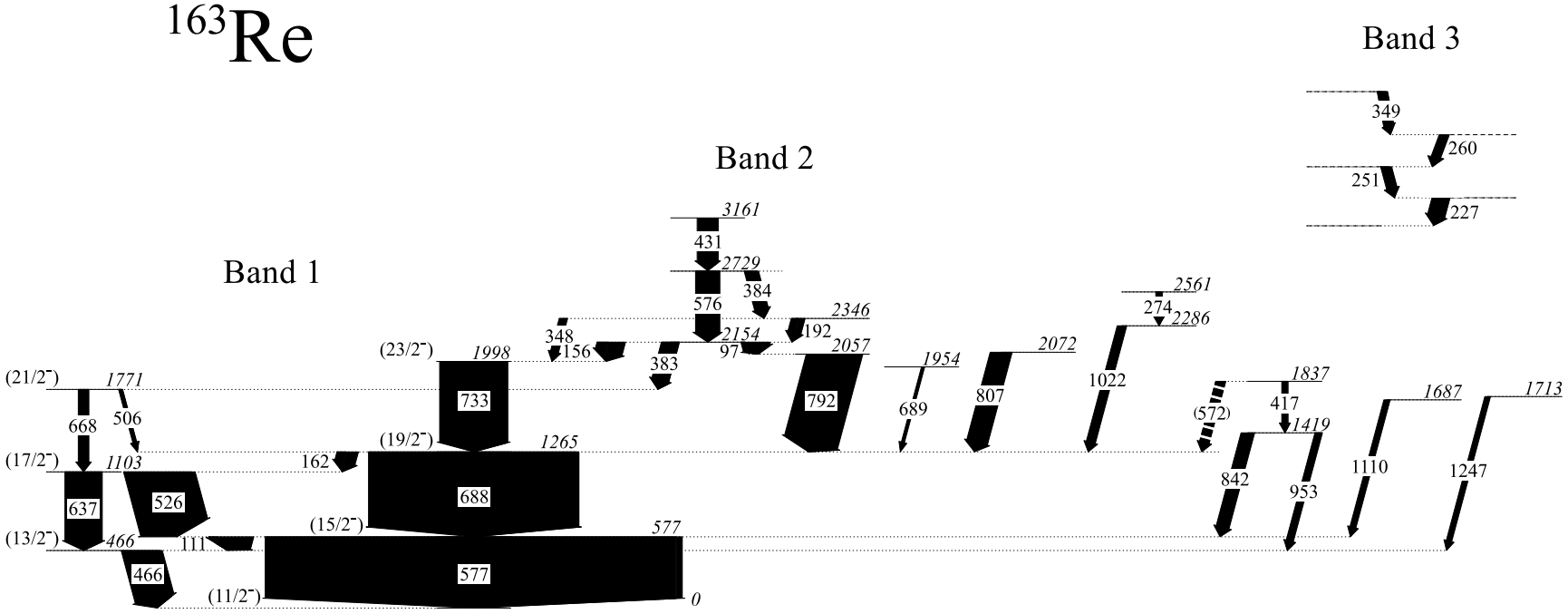

FIGURE 5.2.2: Level scheme deduced for ^{163}Re from an $\alpha(^{163}\text{Re})$-correlated $\gamma\gamma$ matrix. The transition energies are given in keV and their relative intensities are proportional to the widths of the arrows. Dashed lines and parentheses indicate tentative assignments.

TABLE 5.3: Measured properties of γ-ray transitions assigned to ^{163}Re. Energies are accurate to ± 0.5 keV. Tentative assignments are given in parentheses and * denotes transitions assigned to Band 3, where a decay path to Bands 1 or 2 was not identified. Where it has been possible to calculate intensities, they are quoted normalised to the 466 keV transition.

E_γ (keV)	Initial E_{level} (keV)	Initial J^π	Final E_{level} (keV)	Final J^π	I_γ (%)	Assigned multipolarity
97	2154		2057		5.30	
111	577	$15/2^-$	466	$13/2^-$	8.22	$M1$
156	2154		1998	$23/2^-$	18.4	
162	1265	$19/2^-$	1103	$17/2^-$	16.2	$M1$
192	2346		2154		13.4	
227*					(51.9)	
251*					(25.5)	
260*					(44.6)	
274	2561		2286		24.2	
349*					(36.2)	
383	2154		1771	$21/2^-$	(40.2)	
384	2729		2346		(66.4)	
417	1837		1419			
431	3161		2729		(45.1)	
466	466	$13/2^-$	0	$11/2^-$	100	$M1$
506	1771	$21/2^-$	1265	$19/2^-$		$M1$
526	1103	$17/2^-$	577	$15/2^-$	89.9	$M1$
(572)	1837		1265	$19/2^-$		
(576)	2729		2154			
577	577	$15/2^-$	0	$11/2^-$	(396)	$E2$
637	1103	$17/2^-$	466	$13/2^-$	58.8	$E2$
668	1771	$21/2^-$	1103	$17/2^-$	27.0	$E2$

TABLE 5.3 *Continued*: Measured properties of γ-ray transitions assigned to ^{163}Re. Energies are accurate to ± 0.5 keV. Tentative assignments are given in parentheses and * denotes transitions assigned to Band 3 where a decay path to Bands 1 or 2 was not identified. Where it has been possible to calculate intensities, they are quoted normalised to the 466 keV transition.

E_γ (keV)	Initial E_{level} (keV)	Initial J^π	Final E_{level} (keV)	Final J^π	I_γ (%)	Assigned multipolarity
688	1265	$19/2^-$	577	$15/2^-$	29.1	$E2$
689	1954		1265	$19/2^-$		
733	1998	$23/2^-$	1265	$19/2^-$	97.0	$E2$
792	2057		1265	$19/2^-$	73.7	
807	2072		1265	$19/2^-$	26.1	
842	1419		577	$15/2^-$		
953	1419		466	$13/2^-$		
1022	2286		1265	$19/2^-$		
1110	1687		577	$15/2^-$		
1247	1713		466	$13/2^-$		

transitions. The γ-ray coincidence analysis reveals that the yrast sequence is a strongly coupled band at low spin. The ordering of the states at low-excitation energy is fixed by coincidence relationships between the low-lying band members and the high-energy transitions feeding them. Collective excitations based on the favoured (α=$-1/2$) and unfavoured (α=$+1/2$) signature partners are connected by interleaving transitions, which are assumed to have $M1/E2$ multipolarities. The γ-ray intensities for the $\Delta I = 1$ transitions from the unfavoured to favoured signatures are much stronger than the transitions linking in the opposite direction.

This band is expected to have a similar structure to the yrast bands in the heavier Re isotopes [3, 6, 7, 8, 9], which are based on an odd-proton occupying the $h_{11/2}$ [514]$9/2^-$ Nilsson orbital. In ^{163}Re, the $11/2^- \rightarrow 9/2^-$ γ-ray transition is not observed. Trends in the light Re isotopes suggest that the energy difference between the $11/2^-$ state and the $9/2^-$ band head becomes very small as $N = 88$ is approached. Indeed, the measured energy difference between the $11/2^-$ and $9/2^-$ states in ^{173}Re [10], ^{171}Re [8, 9], ^{169}Re [6, 7] and ^{167}Re [40] are 160 keV, 157 keV, 136 keV and 92 keV, respectively. Assuming this trend extrapolates to ^{163}Re, the excitation energies of the $11/2^-$ state and the $9/2^-$ bandhead are inverted, and the resulting low-energy M1 transition ($\sim$50 keV) would be detected with low efficiency by the JUROGAM spectrometer.

Figure 5.2.4 shows γ rays in coincidence with the 733 keV, 792 keV and 156 keV transitions. The 192 keV, 384 keV and 431 keV γ-ray transitions are common to these spectra and form the basis of an excited band structure (labelled Band 2 in Fig. 5.2.2). Furthermore, these spectra indicate that the 733 keV and 156 keV transitions form a parallel decay path to the 97 keV and 792 keV γ rays from a common state at $E_x = 2154$ keV relative to the $11/2^-$ state.

The 577 keV transition is observed to be a doublet. The first and most strongly populated component depopulates the 577 keV (15/2$-$2) state, whilst there are two

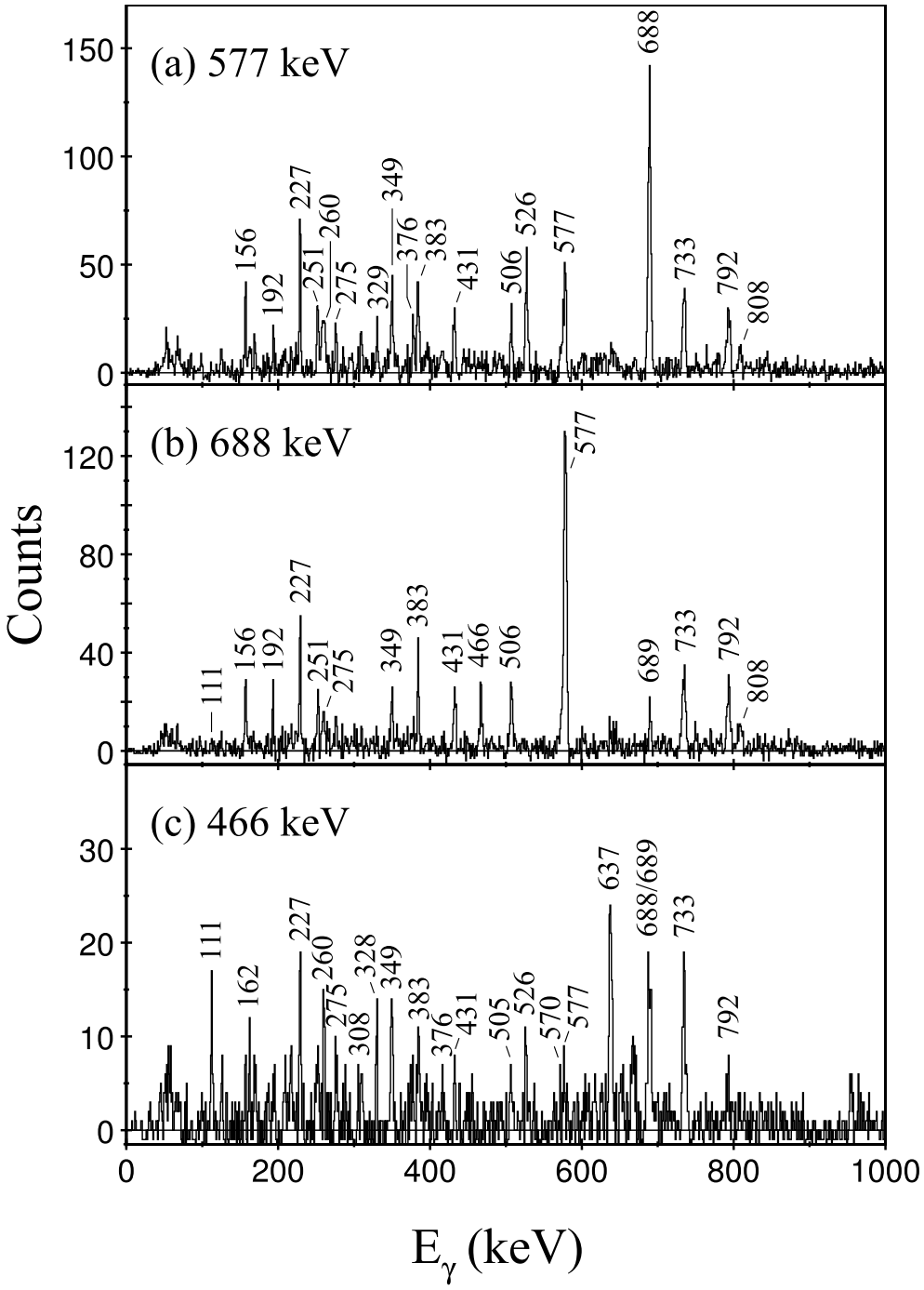

FIGURE 5.2.3: Spectra of prompt γ rays detected in the JUROGAM spectrometer, extracted from an $E_{\gamma 1} - E_{\gamma 2}$ coincidence matrix correlated with recoil implantations followed by the α decay from the $11/2^-$ isomer in ^{163}Re detected within the same DSSD pixel of the GREAT spectrometer. The time for recoil-decay correlations was limited to 214 ms. The spectra show coincidences with (a) the 577 keV transition, (b) the 688 keV transition, and (c) the 466 keV transition.

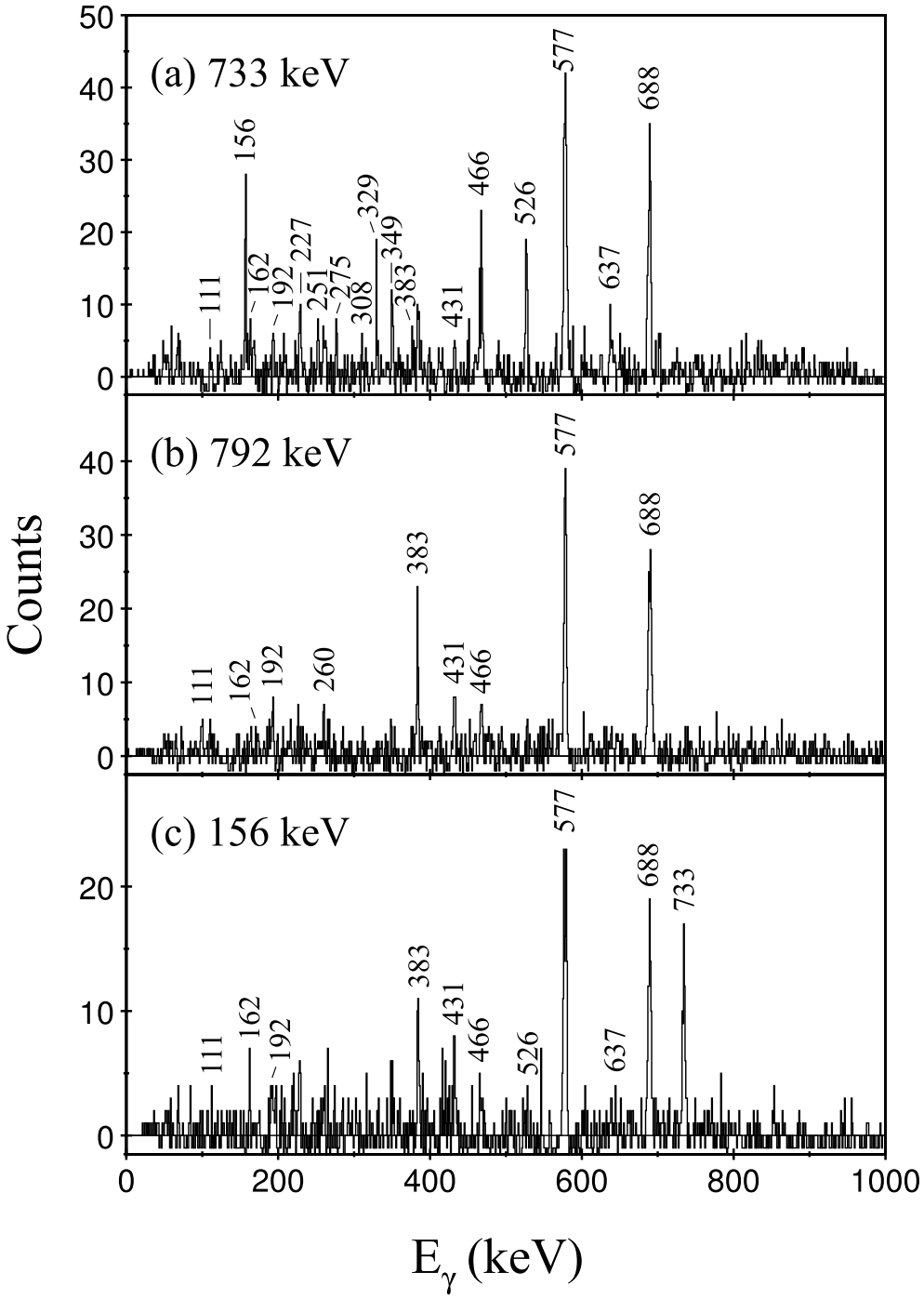

FIGURE 5.2.4: Spectra of prompt γ rays detected in the JUROGAM spectrometer, extracted from an $E_{\gamma 1} - E_{\gamma 2}$ coincidence matrix correlated with recoil implantations followed by the α decay from the $11/2^-$ isomer in ^{163}Re detected within the same DSSD pixel of the GREAT spectrometer. The time for recoil-decay correlations was limited to 214 ms. The spectra show coincidences with (a) the 733 keV transition, (b) the 792 keV transition and (c) the 156 keV transition.

possible locations for the second component of the doublet in the level scheme. The energy difference suggests that the 576 keV transition could be an in-band transition depopulating, the 2729 keV state. However, an alternative placement from the 2346 keV state to the 1771 keV $(21/2^-)$ state is also possible within experimental uncertainties, and cannot be ruled out with these data.

Figure 5.2.5 shows γ-ray coincidences with the 349 keV, 251 keV and 377 keV transitions. A series of γ-ray transitions at 228 keV, 251 keV, 259 keV, 275 keV, 309 keV, 349 keV and 377 keV are observed to be in coincidence with each other, yet it has not been possible to place these transitions in the level scheme unambiguously. These γ rays are not in coincidence with the transitions assigned to Band 2, and are therefore likely to form another band (Band 3) and its decay path. The 228 keV γ ray is prominent in the spectra in Fig. 5.2.3, Fig. 5.2.4(a) and Fig. 5.2.5, which suggests that this transition is placed at the bottom of Band 3. The 228 keV transition feeds the excited states at 1998 keV, 2072 keV and 2286 keV, which are depopulated by the 733 keV, 807 keV and 1022 keV γ-ray transitions, respectively; however, discrete decay paths from Band 3 to these states could not be confirmed with the present data.

The development of the excited states level scheme and its subsequent analysis is complicated by a significant number of doublet and triplet transitions. As a result, $B(M1 : I \rightarrow I-1)/B(E2 : I \rightarrow I-2)$ ratios of reduced transition probabilities could not be measured. Furthermore, poor statistics have made reliable angular intensity correlations impossible and, for this reason, R_{DCO} ratios have not been used in this analysis.

5.2.2 Excited states in ^{165}Re

Previous decay spectroscopy experiments have identified α-decay branches from both the $1/2^+$ ground state and a low-lying $11/2^-$ isomer in ^{165}Re [51, 12, 54]. These

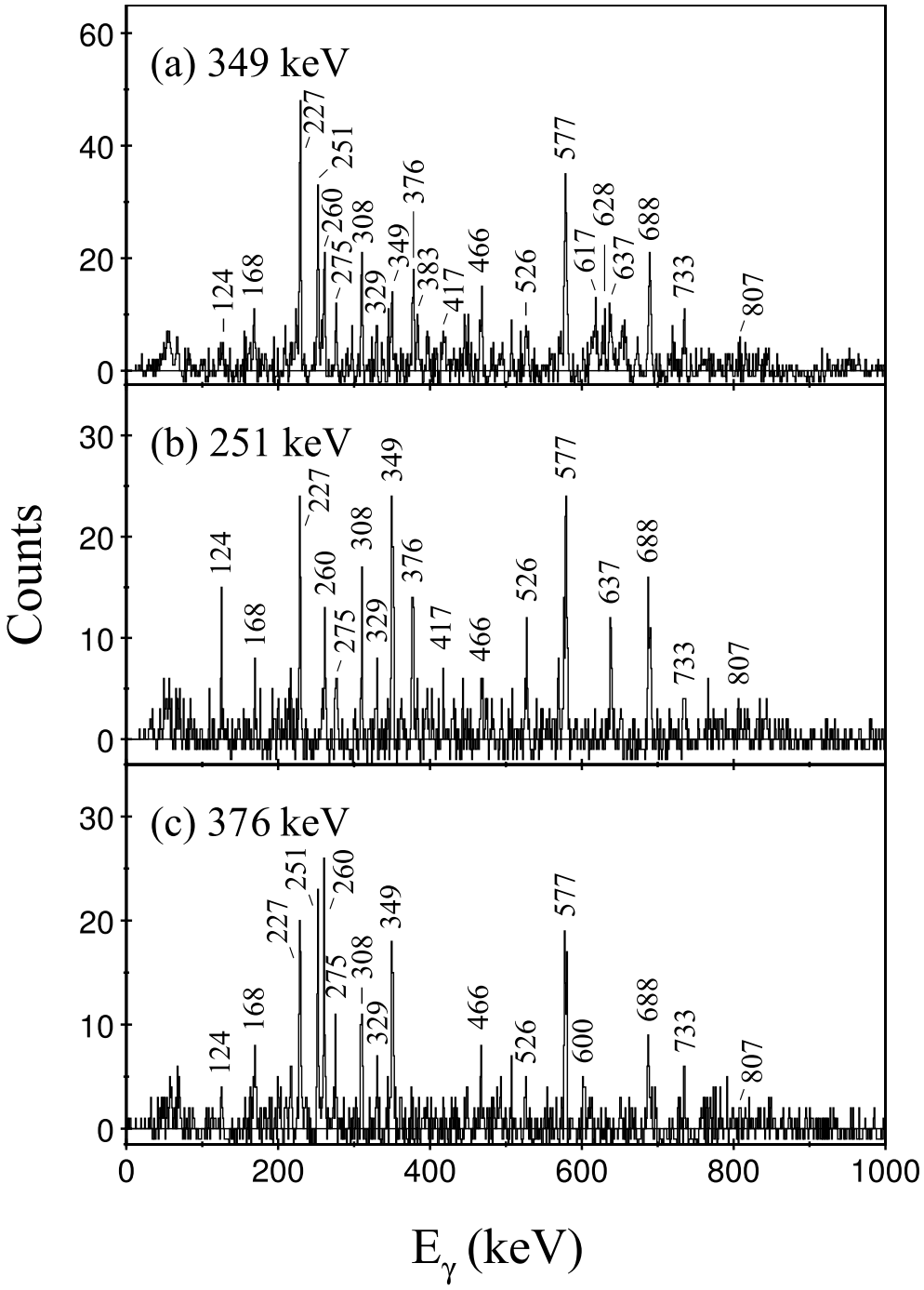

FIGURE 5.2.5: Spectra of prompt γ rays detected in the JUROGAM spectrometer, extracted from an $E_{\gamma 1} - E_{\gamma 2}$ coincidence matrix correlated with recoil implantations followed by the α decay from the $11/2^-$ isomer in ^{163}Re detected within the same DSSD pixel of the GREAT spectrometer. The time for recoil-decay correlations was limited to 214 ms. The spectra show coincidences with (a) the 349 keV transition, (b) the 251 keV transition, and (c) the 376 keV transition.

TABLE 5.4: α-decay properties for the $1/2^+$ ground state and $11/2^-$ isomer of ^{165}Re. The level energies are quoted relative to the ground state. Values taken from Ref. [51, 12, 54].

J^π	Level energy (keV)	Decay Energy (keV)	Half-life (ms)	Branching ratio (%)
$1/2^+$	0.0	5556(6)	1600(600)	14(8)
$11/2^-$	115(4)	5520(6)	1740(60)	13(1)

decay properties, given in Table 5.4, are not ideal for tagging experiments due to their relatively long half-lives and low branching ratios. Furthermore, the $\alpha(^{165m}$Re) decay overlaps the characteristic α-decay peaks from ^{166}Re [E_α = 5533(10) keV, $t_{1/2}$ = 2120(380) ms [51, 55, 56] and ^{162}W [E_α = 5541(5) keV, $t_{1/2}$ = 1200(100) ms, b_α=44(2)%] [51], which are produced in the fusion-evaporation reaction via the $3pn$ and $\alpha 2p2n$ exit channels, respectively. Uniquely assigning γ rays to ^{165}Re using the recoil-decay tagging technique is thus problematic due to the similar properties of these unresolved α decays.

Figure 5.2.6 shows γ-ray coincidence spectra generated from an α(5520 keV)-correlated $\gamma\gamma$ matrix. The recoil-decay correlation time was limited to 5 s. The coincidences demanded with the 337 keV, 202 keV and 672 keV γ rays provide evidence for a new strongly coupled band. A strongly coupled band must be based on a configuration with at least one odd nucleon in a deformation-aligned (high-Ω) orbital, which in this region of the nuclear chart is likely to be the odd proton in the $h_{11/2}$ orbital. This would limit the assignment of the new band to either ^{165}Re or ^{166}Re, rather than the even-even nucleus ^{162}W.

The technique of inverse tagging has been used to aid the unambiguous assignment of γ-ray transitions in this new band to a specific nuclide [57]. Inverse tagging uses γ rays measured at the target position as an additional criterion for the selection of α-decay chains. Figure 5.2.7(a) shows all α decays detected between 500 ms and 5 s after a recoil implantation within the same DSSD pixel. Figure 5.2.7(b) shows

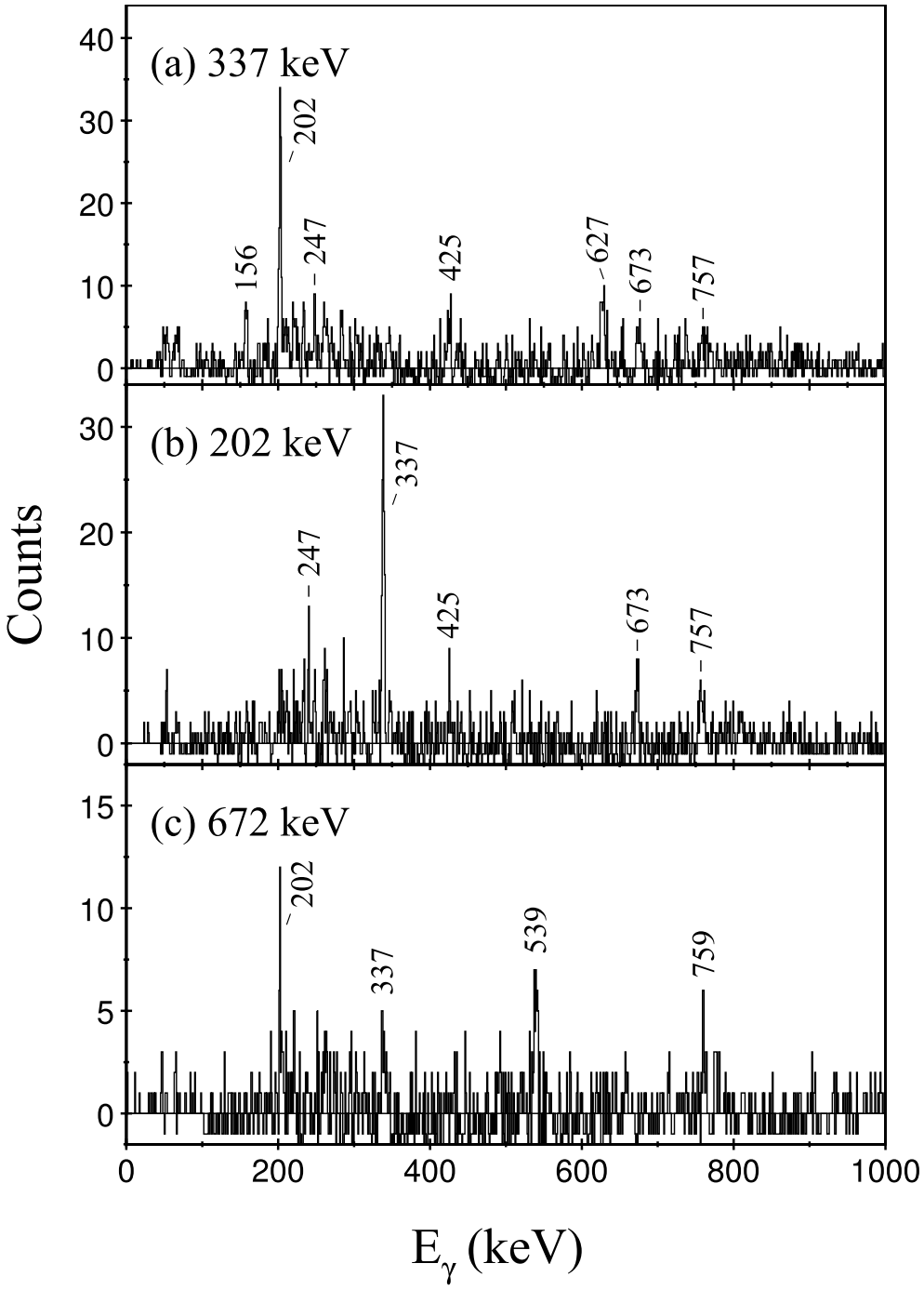

FIGURE 5.2.6: Spectra of prompt γ rays detected in the JUROGAM spectrometer, extracted from an $E_{\gamma 1} - E_{\gamma 2}$ coincidence matrix correlated with recoil implantations followed by the 5520 keV unresolved α decays from ^{162}W, ^{165m}Re and ^{166}Re detected within the same DSSD pixel of the GREAT spectrometer. The time for recoil-decay correlations was limited to 5 s. The spectra show coincidences with (a) the 337 keV transition, (b) the 202 keV transition, and (c) the 672 keV transition.

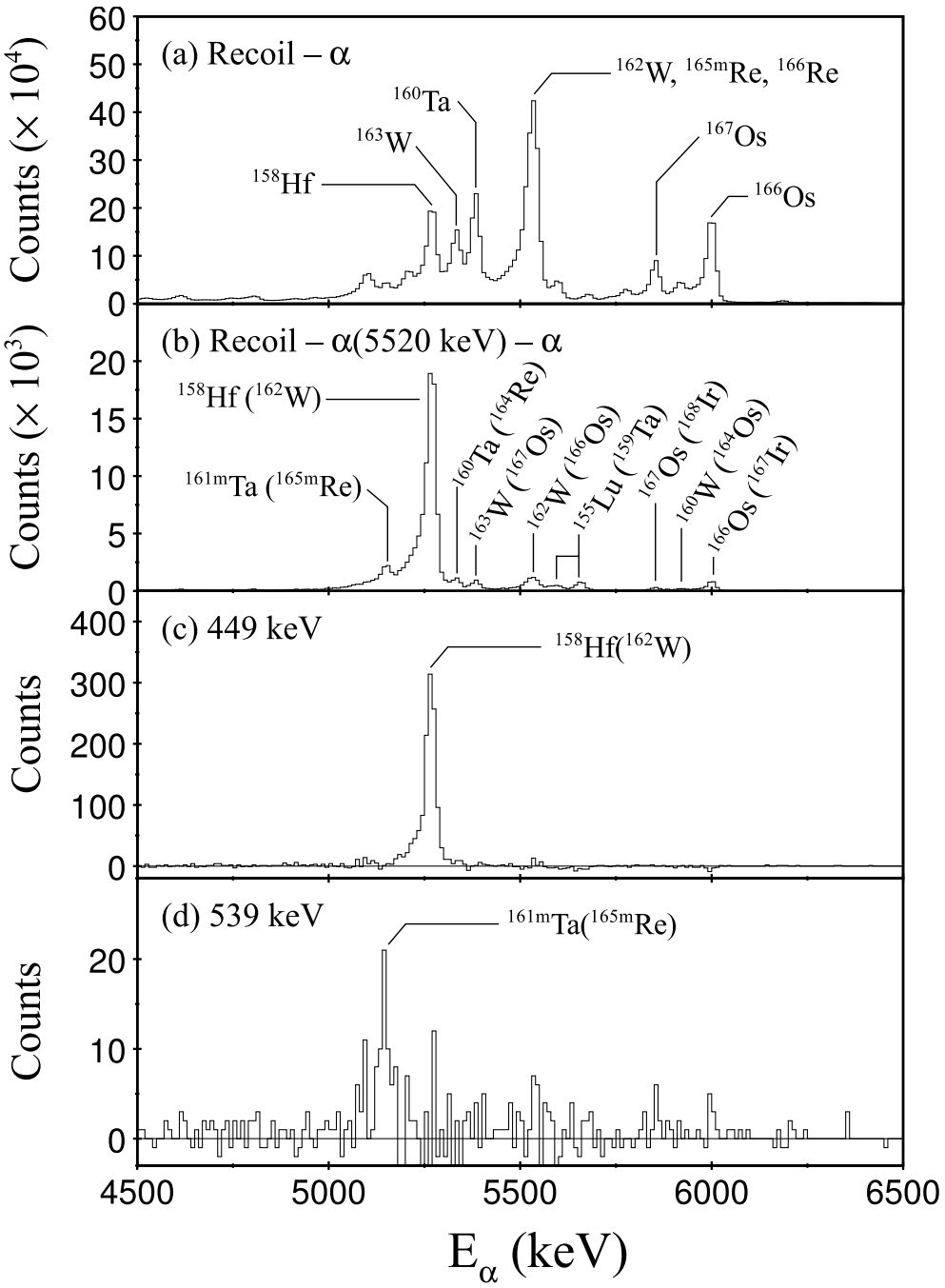

FIGURE 5.2.7: (a) Alpha particles detected between 500 ms and 5000 ms after a recoil implantation in the same pixel of the GREAT DSSD. (b) Second generation α-decays following a recoil implantation and the subsequent decay with energy within the 5520 keV unresolved α-decay peaks. (c) The same conditions as for panel (b), with the additional constraint that the decay chain is in delayed coincidence with the 449 keV transition in ^{162}W, detected at the target position. (d) The same conditions for panel (b), with the additional constraint that the decay chain is in delayed coincidence with the 539 keV transition detected at the target position. The second generation α-decay of ^{161m}Ta indicates that the 539 keV γ ray is emitted by ^{165}Re.

all second-generation α decays preceded by the detection of a recoil implantation and the 5520 keV unresolved α-decay peaks. The correlation time between α decays was limited to 10 s. The ^{158}Hf and ^{161m}Ta α-decay peaks, which originate from the ^{162}W and ^{165m}Re precursors, respectively, are prominent in the spectrum while the ^{162}Ta α-decay arising from the decay of ^{166}Re is not observed. There are several α-decay emissions arising from spurious decay correlations due to the long correlation time between first- and second-generation α decays. Figure 5.2.7(c) shows the second-generation α decays with the additional condition of a delayed coincidence with the 449 keV ($2^+ \rightarrow 0^+$) γ-ray transition in ^{162}W detected at the target position. An α-decay background has been subtracted to mitigate correlations with the γ-ray background arising from Compton scattering. The inverse tagging technique is sufficiently selective to identify the second α decay in the recoil $\rightarrow$ ^{162}W $\rightarrow$ ^{158}Hf decay chain. Similar correlations with the 539 keV γ ray, shown in Fig. 5.2.7(d), select the recoil $\rightarrow$ ^{165m}Re $\rightarrow$ ^{161m}Ta decay chain. The strongly coupled band is assigned to ^{165}Re on the basis of these inverse tagging correlations, and the level scheme deduced from the α(5520 keV)-$\gamma\gamma$ coincidence analysis is shown in Fig. 5.2.8.

5.3 Discussion

The level schemes of ^{163}Re and ^{165}Re have many features in common with other odd-A transitional nuclei above the $N = 82$ shell gap. The strongly coupled bands have a large degree of signature splitting at low spin, which is similar to the heavier known Re isotopes [3, 6, 7, 8, 9] and the analogous structures in the odd-A Ir [58] and Ta [52, 59, 60] isotopes. Figure 5.3.1 shows the evolution of the $9/2^-$, $13/2^-$ ($\alpha = +1/2$) and $15/2^-$ ($\alpha = -1/2$) state excitation energies relative to the $11/2^-$ state as a function of neutron number. The $13/2^-$ states lie near the midpoint between the $15/2^-$ and $11/2^-$ levels in the isotopes approaching the neutron midshell

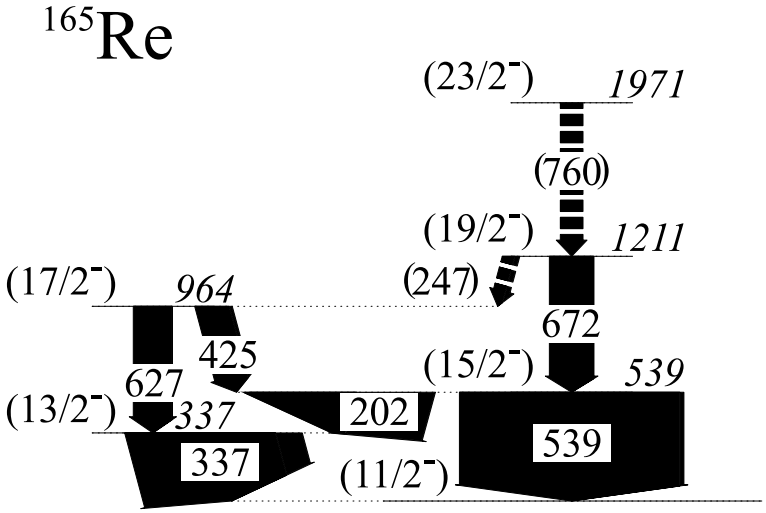

FIGURE 5.2.8: Level scheme deduced for ^{165}Re from an α(5520 keV)-correlated $\gamma\gamma$ matrix. The transition energies are given in keV, and their relative intensities are proportional to the widths of the arrows. Dashed lines and parentheses indicate tentative assignments.

at $N = 104$, which is expected for nuclei exhibiting axial prolate symmetry. The difference in excitation energy between the $15/2^-$ and $13/2^-$ states decreases steadily below $N = 94$, showing a greater degree of signature splitting towards $N = 82$.

The magnitude of the signature splitting can be highlighted by the staggering parameter $S(I)$ [61], which is defined by

$$\begin{aligned} S(I) = E(I) - E(I-1) - 1/2[E(I+1) \\ - E(I) + E(I-1) - E(I-2)]. \end{aligned} \tag{5.3.1}$$

Figure 5.3.2 compares the staggering parameter extracted for the $h_{11/2}$ bands in ^{163}Re and ^{165}Re with those of the heavier Re isotopes, and clearly illustrates the trend of increasing signature splitting towards lower neutron numbers. The splitting is interpreted to arise from the combined core-polarising influences of the high-Ω $h_{11/2}$ proton and the low-Ω neutron orbitals, which result in a soft triaxial shape.

The staggering parameter becomes very small in the heavier Re isotopes, reflect-

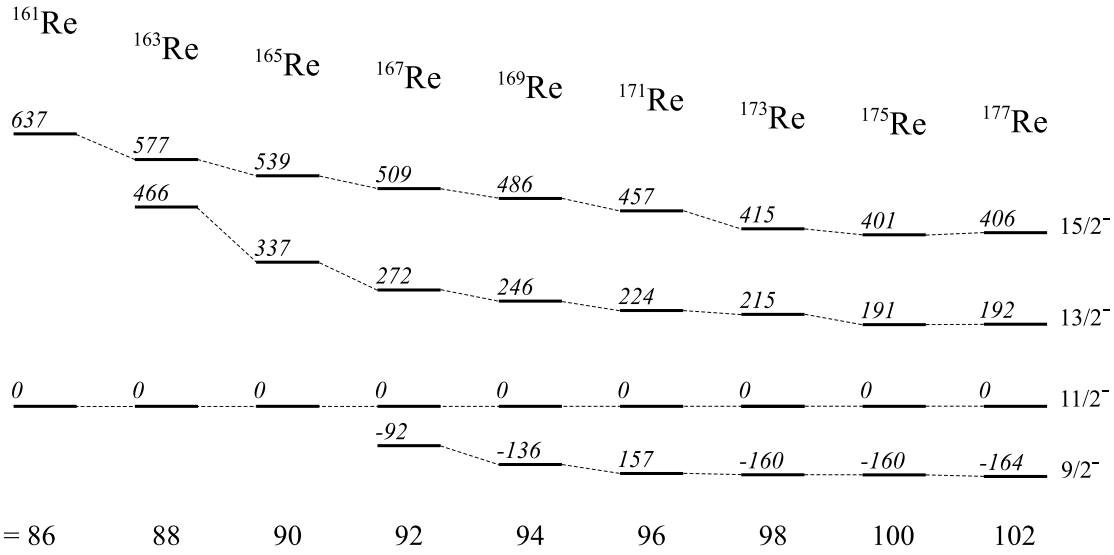

FIGURE 5.3.1: Evolution of low-lying excited states in the neutron-deficient transitional Re isotopes as a function of neutron number. The excitation energies of the $9/2^-$, $13/2^-$ and $15/2^-$ levels are given in keV and stated relative to the $11/2^-$ state.

ing the dramatic reduction in signature splitting. The disappearance of signature splitting is related to the crossing of the single quasiproton configuration by the three quasiparticle $\pi h_{11/2} \otimes (\nu i_{13/2})^2$ configuration [3, 6, 7, 8, 9]. The rotational alignment of an $i_{13/2}$ neutron pair at this crossing brings about a change from γ-soft triaxial shapes to axially symmetric prolate deformations.

The likely configurations for the lowest-lying three-quasiparticle bands in ^{163}Re and ^{165}Re can be predicted by considering the total energy of the nucleus in the rotating frame (or total Routhian E'). Total Routhians have been calculated for multi-quasiparticle configurations by summing single-particle Routhians extracted from cranked-shell model calculations incorporating a Nilsson potential and adding a γ-deformation-dependent reference, as proposed by Frauendorf and May [62, 63], such that

$$E'(\omega,\gamma) = \sum_{\mu} e'_{\mu}(\omega,\gamma) + E'_{Ref}(\omega,\gamma), \tag{5.3.2}$$

where e'_{μ} are the single quasiparticle Routhians and $E'_{Ref}(\omega,\gamma)$ is a γ-dependent

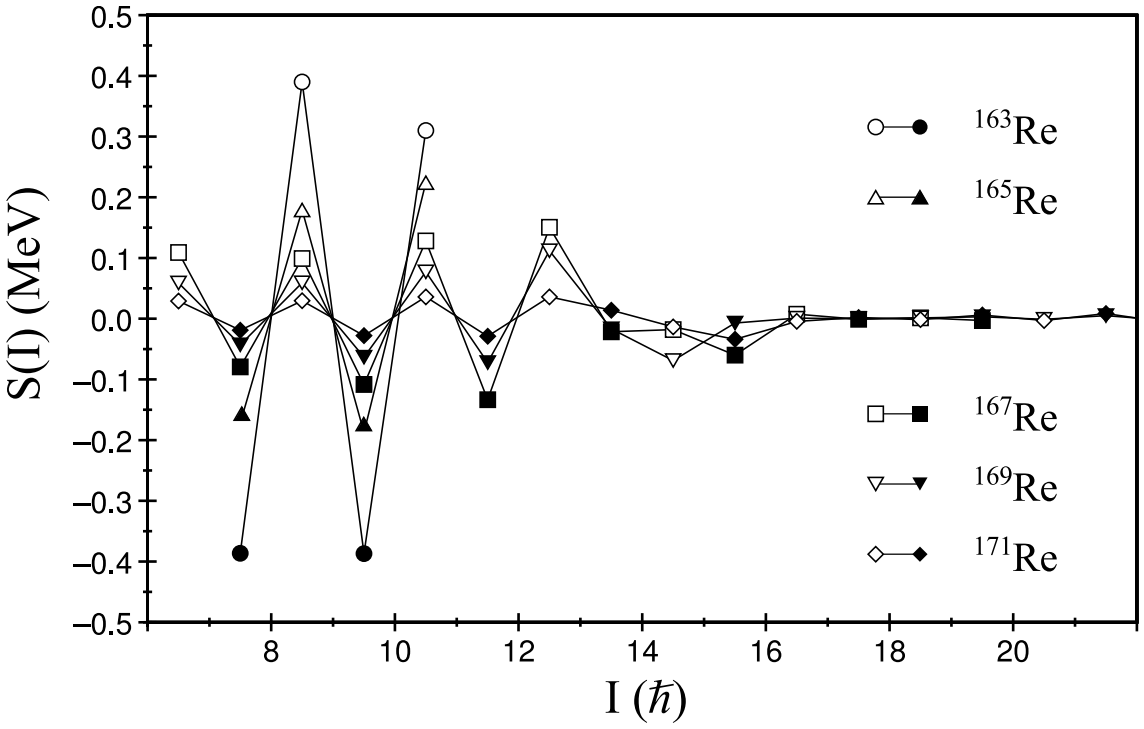

FIGURE 5.3.2: Staggering parameter $S(I)$ as a function of spin I for the $[514]9/2^-$ bands in the neutron-deficient odd-A rhenium isotopes ^{163}Re, ^{165}Re, ^{167}Re [3], ^{169}Re [6, 7] and ^{171}Re [8, 9]. The solid (open) symbols represent the $\alpha = -1/2$ $(+1/2)$ signatures.

reference defined as

$$E'_{ref}(\omega,\gamma) = \frac{1}{2}V_{po}\cos(3\gamma) - \frac{3}{2}\omega^2\left(\mathcal{J}_0 + \frac{1}{2}\omega^2\mathcal{J}_1\right)\cos^2(\gamma + 30^\circ) \tag{5.3.3}$$

The parameter V_{po} is a prolate-oblate energy difference and $\mathcal{J}_0$ and $\mathcal{J}_1$ are the Harris parameters. The total Routhians for ^{163}Re are shown in Fig. 5.3.3. The labelling convention for the constituent quasiparticles is adopted from Ref. [64], and the resulting configurations are listed in Table 5.5.

Figure 5.3.3 gives an insight into the microscopic basis for the observed features of the low-spin $h_{11/2}$ bands in ^{163}Re and ^{165}Re. The single-quasiproton configurations,

TABLE 5.5: Labelling convention for single- and three-quasiparticle configurations in ^{163}Re. The convention adopted is taken from Ref. [64].

Label	Signature & Parity (α, π)	Configuration
e	(−,−1/2)	$\pi h_{11/2}$
f	(−,+1/2)	$\pi h_{11/2}$
eEF	(−,−1/2)	$\pi h_{11/2} \otimes \nu(f_{7/2}, h_{9/2})^2$
fEF	(−,+1/2)	$\pi h_{11/2} \otimes \nu(f_{7/2}, h_{9/2})^2$
eAE	(+,−1/2)	$\pi h_{11/2} \otimes \nu[i_{13/2} \otimes (f_{7/2}, h_{9/2})]$
fAE	(−,+1/2)	$\pi h_{11/2} \otimes \nu[i_{13/2} \otimes (f_{7/2}, h_{9/2})]$
eAF	(−,+1/2)	$\pi h_{11/2} \otimes \nu[i_{13/2} \otimes (f_{7/2}, h_{9/2})]$
fAF	(−,+3/2)	$\pi h_{11/2} \otimes \nu[i_{13/2} \otimes (f_{7/2}, h_{9/2})]$
eAB	(−,−1/2)	$\pi h_{11/2} \otimes \nu(i_{13/2})^2$
fAB	(−,+1/2)	$\pi h_{11/2} \otimes \nu(i_{13/2})^2$

labelled e and f, represent the negative-parity $\alpha = -1/2$ and $\alpha = +/2$ signatures of the $h_{11/2}$ orbital, respectively. These configurations exhibit large signature splitting between the e and f Routhians in the range $-80° \leq \gamma \leq -10°$, which is consistent with the experimental staggering parameter obtained at low spins, as shown in Fig. 5.3.2. The e Routhian has a shallow minimum total energy at $\gamma \sim -30°$ corresponding to a triaxially deformed rotor.

The calculations predict that the lowest energy three-quasiparticle structures in ^{163}Re should be negative-parity bands based on the eEF and fEF configurations. These structures are formed by coupling the odd proton to the mixed rotationally aligned $\nu(f_{7/2}, h_{9/2})^2$ neutron configuration. The first rotational alignment in the lighter $N = 88$ isotones ^{161}Ta [59] and ^{162}W [66, 67] is interpreted as arising from the same EF quasineutron alignment, which is favoured over the $i_{13/2}$ (AB) rotational

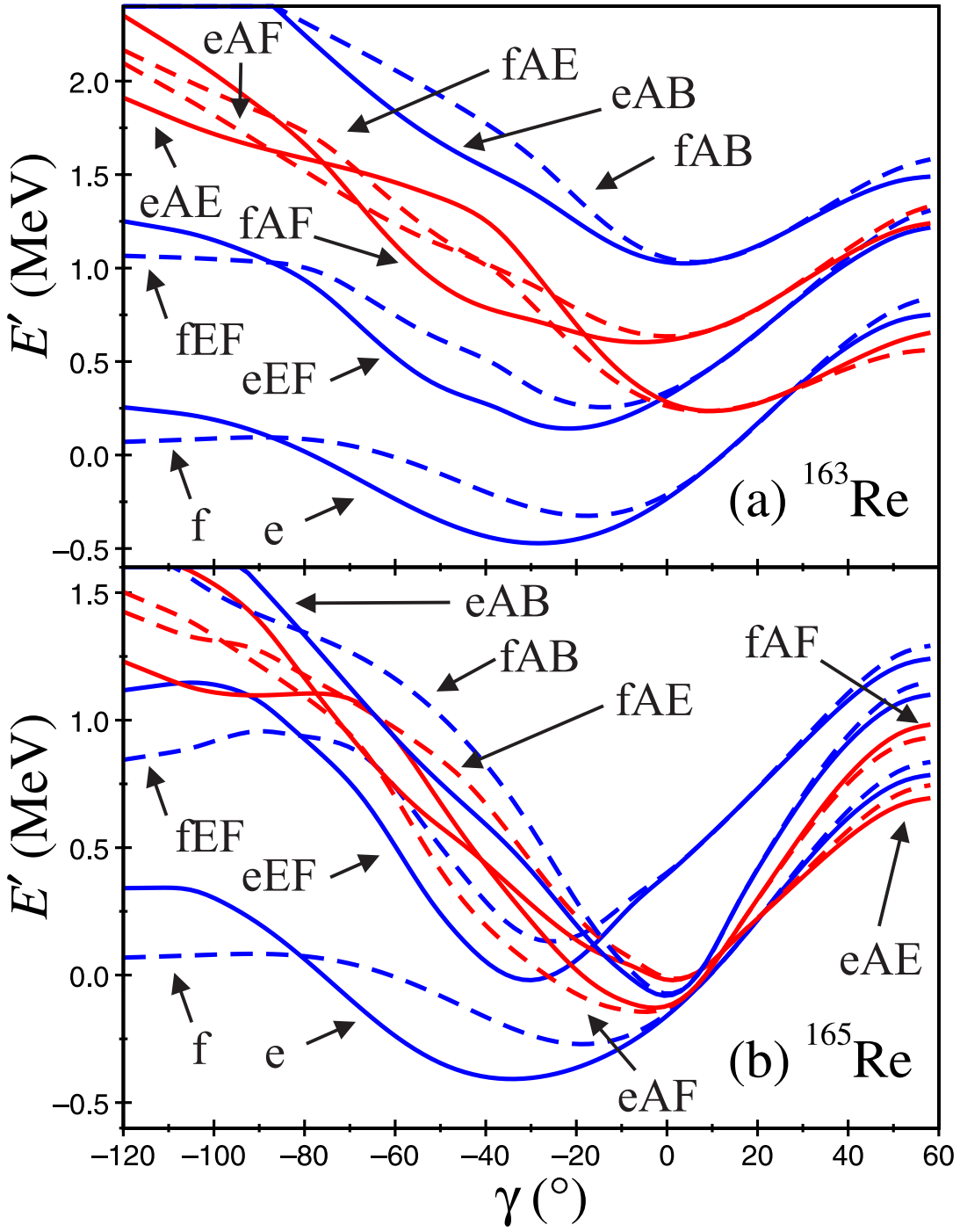

FIGURE 5.3.3: Calculated total Routhians as a function of γ deformation for single and three-quasiparticle configurations in (a) ^{163}Re and (b) ^{165}Re. The Routhians are calculated at a rotational frequency of 0.2 MeV and assume a prolate-oblate energy difference $V_{po} = -0.4$ and quadrupole deformation parameters of $\epsilon_2 = 0.117$ and $\epsilon_2 = 0.117$ for ^{163}Re and ^{165}Re, respectively. The deformation parameters are taken from Ref. [65]. The Harris parameters are fixed at $\mathcal{J}_0$= 26 $\hbar^2$MeV^{-1} and $\mathcal{J}_1$= 32 $\hbar^4$MeV^{-3} and are taken from Ref. [59]. The e, f, eEF, fEF, eAB and fAB, configurations have negative parity (blue lines) while the eAE, fAE, eAF and fAF configurations have positive parity (red lines). The solid (dashed) lines represent the $\alpha = -1/2$ $(+1/2)$ signature.

alignment observed in the heavier isotopes. This is a consequence of the higher excitation energy of the $\nu i_{13/2}$ orbitals relative to the $\nu(f_{7/2}, h_{9/2})$ negative-parity states, which is attributed to the lower average deformation of the isotopes closer to the $N = 82$ shell gap. Thus, the eAB/fAB configurations are non-yrast at low spin in ^{163}Re, see Fig. 5.3.3(a).

The eEF and fEF configurations have their minimum total energy at triaxial deformation ($\gamma \sim -15°$) and exhibit a significant degree of signature splitting. These configurations are observed to high spin in the lighter odd-Z $N = 88$ isotone, ^{161}Ta [59], and show a persistence of signature splitting beyond the alignment. Band 2 in ^{163}Re would be a good candidate for the eEF and fEF configurations if the 192 keV and 384 keV transitions are the interleaving $\Delta I = 1$ transitions of a strongly coupled band.

The total Routhians for ^{165}Re suggest that the lowest-energy three-quasiparticle excitations should be based on configurations involving at least one $i_{13/2}$ quasineutron orbital, as observed in the other $N = 90$ isotones ^{163}Ta [52] and ^{164}W [68]. The lower excitation energy of the $i_{13/2}$ quasineutron orbital reflects the larger average deformation of ^{165}Re, when compared with ^{163}Re (*c.f.* $\epsilon_2(^{165}\text{Re}) = 0.142$, $\epsilon_2(^{163}\text{Re}) = 0.117$) [65].

The coincidence analysis indicates that the γ rays assigned to Band 3 in ^{163}Re feed the states depopulated by 733 keV, 807 keV and 1022 keV transitions, although it has not been possible to elucidate these discrete decay paths in this work. Figure 5.3.3 predicts that the eEF and fEF configurations are only marginally favoured over the prolate eAE and fAE positive-parity configurations formed by coupling the $h_{11/2}$ proton to the $i_{13/2}\otimes(f_{7/2}, h_{9/2})$ neutron orbitals. Further work is needed to determine if the transitions belonging to Band 3 are based on this configuration. The total Routhians for the eAE/fAE configurations in ^{163}Re are significantly higher than the analogous structures in the lighter odd-Z isotone ^{161}Ta [59], which are yrast

at high spin ($29/2 \leq I \leq 43/2\hbar$). Indeed, the relative positions of the eEF/fEF and eAE/fAE are inverted in ^{163}Re. This is a consequence of the lower deformation in ^{163}Re due to the smaller proton valence space (*c.f.* $\epsilon_2(^{163}\text{Re}) = 0.133$, $\epsilon_2(^{161}\text{Ta}) = 0.117$) [65].

Chapter 6

Summary

In this work, excited states in two Re isotopes in the neutron-deficient region close to the proton drip line and the $N = 82$ shell closure have been studied. In two separate experiments, excited states in ^{163}Re and ^{165}Re have been populated using heavy-ion fusion evaporation reactions, performed at the University of Jyväskylä Accelerator Laboratory, Finland. Evaporation residues recoiling from the targets were separated in-flight from the beam species and fission products by the RITU gas-filled separator and transported to the focal plane, where they were implanted into the DSSDs of the GREAT spectrometer. Prompt γ rays emitted at the target position were detected by the JUROGAM spectrometer array. Recoil-decay correlations have been used to unambiguously assign γ-ray transitions to ^{163}Re and ^{165}Re.

This work has allowed for the scheme of excited states in ^{163}Re to be significantly revised and extended. For the first time, two further band structures, which strongly feed the low-spin states of the yrast configuration, have been identified. This work also presents the first observation of γ-ray transitions assigned to ^{165}Re, which have been placed in a strongly coupled band structure.

Signature splitting considerations and total Routhian calculations within the framework of the cranked shell model have been used to propose configuration as-

signments for the observed structures in both nuclei. At low spin, the yrast structure in ^{163}Re is a strongly coupled band assigned to a deformation-aligned odd proton in the high-Ω $h_{11/2}$ orbital. This structure exhibits large signature splitting consistent with a γ-soft triaxial rotor and no high-spin rotational alignment is observed. This is consistent the Nilsson model, where there are fewer valence neutrons to drive deformation and the prolate-driving low-Ω $i_{13/2}$ orbital lies at high excitation energy. The strongly coupled band observed in ^{165}Re is assigned to the single-quasiproton $\pi h_{11/2}$ configuration. This structure exhibits a degree of signature splitting which is approximately midway between that of ^{163}Re and the heavier isotopes. This is in agreement with the trend of increasing signature splitting with neutron deficiency.

On the basis of the total Routhian calculations, candidates for the $\pi h_{11/2}\otimes \nu(f_{7/2}, h_{9/2})^2$ (eEF/fEF) and the $\pi h_{11/2}\otimes \nu[i_{13/2}\otimes(f_{7/2}, h_{9/2})]$ (eAE/fAE) three-quasiparticle configurations in ^{163}Re have been suggested. In addition, these predictions suggest that, due to its lower average deformation, the relative positions of the eEF/fEF and and eAE/fAE configurations are inverted in ^{163}Re, relative to the heavier isotope ^{165}Re and the lighter $N = 88$ isotones.

References

[1] E. Rutherford, Philosophical Magazine **21**, 669 (1911).

[2] E. S. Paul *et al.*, Phys. Rev. C **51**, 78 (1995).

[3] D. T. Joss *et al.*, Phys. Rev. C **68**, 014303 (2003).

[4] E. S. Paul *et al.*, Phys. Rev. Lett. **98**, 012501 (2007).

[5] K. Lagergren *et al.*, Phys. Rev. C **74**, 024316 (2004).

[6] X. H. Zhou *et al.*, Eur. Phys. J. **A19**, 11 (2004).

[7] D. J. Hartley *et al.*, Phys. Rev. C **87**, 024315 (2004).

[8] R. A. Bark, G. D. Dracoulis, A. E. Stuchbery, A. P. Byrne, A. M. Baxter, F. Riess, and P. K. Wang, Nucl. Phys. **A501**, 157 (1989).

[9] H. Carlsson, Nucl. Phys. **A551**, 295 (1993).

[10] L. Hildingsson, Nucl. Phys. **A513**, 394 (1990).

[11] D. T. Joss *et al.*, Spectroscopy of the neutron-deficient isobars (163)re and (163)w using tagging techniques, in *Conference on Nuclear Physic and Astrophysics - From Stable Beams to Exotic Nucle* Vol. 1072, pp. 154–159, 2008.

[12] C. W. Reich and R. G. Helmer, Nucl. Data Sheets **90**, 645 (2000).

[13] R. D. Woods and D. S. Saxon, Phys. Rev. **95**, 577 (1954).

[14] R. Casten, *Nuclear Structure from a Simple Perspective*, 2nd ed. (Oxford Science Publications, 2005).

[15] W. Greiner and J. A. Maruhn, *Nuclear Models* (Springer-Verlag Berlin Heidelberg New York, 1996).

[16] A. Klein, Physical Review C **63** (2001).

[17] S. Kumar, International Journal of Computer Science and Communication Engineering **Emerging Trends in Engineering ICETIE** (2012).

[18] S. Frauendorf and F. R. May, Physics Letters **125B**, 245 (1983).

[19] F. S. Stephens, Rev. Mod. Phys. **47**, 43 (1975).

[20] D. R. Inglis, Phys. Rev. **96**, 1059 (1954).

[21] D. R. Inglis, Phys. Rev. **103**, 1786 (1956).

[22] D. Thouless and J. Valatin, Nuclear Physics **31**, 211 (1962).

[23] R. Bengtsson and S. Frauendorf, Nuclear Physcis **A327**, 139 (1979).

[24] Y. Sun, D. H. Feng, and S. X. Wen, Physical Review C **50**, 2351 (1994), Sun, y feng, dh wen, sx.

[25] A. Bohr *et al.*, Rev. Mod. Phys. **48**, 365 (1976).

[26] M. M. Sirag, Turk. J. Phys. **33**, 333 (2009).

[27] R. D. Page *et al.*, Nucl. Instrum. Methods Phys. Res. B **204**, 634 (2003).

[28] I. H. Lazarus *et al.*, IEEE Trans. Nucl. Sci. **48**, 567 (2001).

[29] J. Uusitalo *et al.*, Nucl. Instrum. Methods Phys. Res. B **204**, 638 (2003).

[30] J. Sarén, J. Uusitalo, M. Leino and J. Sorri, Nucl. Instrum. Methods Phys. Res. A **654**, 508 (2011).

[31] P. Rahkila, Nucl. Instrum. Methods Phys. Res. A **595**, 637 (2008).

[32] D. C. Radford., Nucl. Instrum. Methods Phys. Res. A **361**, 297 (1995).

[33] P. Regan, Postgraduate nuclear experimental techniques (4net) course notes, `http://personal.ph.surrey.ac.uk/~phs1pr/lecture_notes/nuc_expt_phr03.pdf` (Accessed: 27th November 2013), 2003.

[34] Z. Szymański, *Fast Nuclear Rotation* (Clarendon Press, Oxford, UK, 1983).

[35] C. W. Beausang *et al.*, Nucl. Instrum. Methods Phys. Res. A **313**, 37 (1992).

[36] M. Leino *et al.*, Acta Physica Polonica. **B 26**, 309 (1995).

[37] E. Liukkonen, New K130 cyclotron at Jyväskylä, in *Proceedings of the 13th International Conference on Cyclotrons and their Applications, Vancouver, BC, Canada*, 1993.

[38] A. Bohr and and B. R. Mottelson, *Nuclear Structure Volume 1: Single-Particle Motion* (W. A. Benjamin Inc, New York, USA, 1969).

[39] A. Bohr and B. R. Mottelson, *Nuclear Structure Volume 2: Nuclear Deformation* (W. A. Benjamin Inc, New York, USA, 1975).

[40] D. T. Joss *et al.*, Phys. Lett. **B641**, 34 (2006).

[41] S. J. Steer *et al.*, Phys. Rev. C **84**, 044313 (2011).

[42] R. D. Page *et al.*, Phys. Rev. Lett **68**, 1287 (1992).

[43] I. G. Darby *et al.*, Phys. Rev. C **83**, 064320 (2011).

[44] R. J. Irvine *et al.*, Phys. Rev. C **55**, R1621 (1997).

[45] I. G. Darby *et al.*, Phys. Lett. **B695**, 78 (2011).

[46] P. J. Sapple *et al.*, Phys. Rev. C **84**, 054303 (2011).

[47] Y. S. Chen, S. Frauendorf and G. A. Leander, Phys. Rev. C **28**, 2437 (1983).

[48] C. W. Beausang and J. Simpson., J. Phys. G **22**, 527 (1996).

[49] C. N. Davids *et al.*, Phys. Rev. C **55**, 2255 (1997).

[50] C. N. Davids *et al.*, Hyperfine Interactions **132**, 133 (2001).

[51] R. D. Page, P. J. Woods, R. A. Cunningham, T. Davinson, N. J. Davis, A. N. James, K. Livingston, P. J. Sellin, and A. C. Shotter, Phys. Rev. C **53**, 660 (1996).

[52] M. Sandzelius *et al.*, Phys. Rev. C **80**, 054316 (2009).

[53] J. Thomson *et al.*, Phys. Rev. C **81**, 014307 (2010).

[54] A. Thornthwaite *et al*, Phys. Rev. C **86**, 064315 (2012).

[55] U. J. Schrewe, W. D. Schmidt-Ott, R. D. v. Dincklage, E. Georg, P. Lemmertz, H. Jungclas, and D. Hirdes, Z. Phys. A **288**, 189 (1978).

[56] F. Meissner, H. Salewski, W. D. Schmidt-Ott, U. Bosche-Wicke and R. Michaelsen, Z. Phys. A **343**, 283 (1992).

[57] L. Bianco *et al.*, Nucl. Instrum. Methods Phys. Res. A **597**, 189 (2008).

[58] M. Sandzelius *et al.*, Phys. Rev. C **75**, 054321 (2007).

[59] K. Lagergren *et al.*, Phys. Rev. C **83**, 014313 (2011).

[60] D. G. Roux *et al.*, Phys. Rev. C **63**, 024303 (2001).

[61] A. J. Kreiner, M. A. J. Mariscotti, C. Baktash and E. der Mateosian, Phys. Rev. C **23**, 748 (1981).

[62] S. Frauendorf and F. R. May, Phys. Lett **B125**, 245 (1983).

[63] E. S. Paul, C. W. Beausang, D. B. Fossan, R. Ma, W. F. Piel Jr., P. K. Weng, and N. Xu, Phys. Rev. C **36**, 153 (1987).

[64] R. Wyss, J. Nyberg, A. Johnson, R. Bengtsson, and W. Nazarewicz, Phys. Lett. **B215**, 211 (1988).

[65] P. Möller, J. R. Nix, W. D. Myers, and W. J. Swiatecki, At. Data Nucl. Data Tables **59**, 185 (1995).

[66] G. D. Dracoulis *et al.*, Proceedings of the International Conference on Nuclear Structure at High Angular Momentum, Ottawa, AECL Report No. 10613 (unpublished) **2**, p94 (1992).

[67] G. D. Dracoulis, *Private communication.*

[68] J. Simpson, M. A. Riley, A. Alderson, M. A. Bentley, A. M. Bruce, D. M. Cullen, P. Fallon, F. Hanna, and L. Walker, J. Phys. **G17**, 511 (1991).